UNIVERSIDADE ESTADUAL PAULISTA
“JÚLIO DE MESQUITA FILHO”
School of Engineering
Campus São João da Boa Vista

Helton Silva Bernardo

Gain Enhancement and Sidelobe Level Reduction of Rectangular Microstrip Patch Antenna Under Operation of High-Order Modes

São João da Boa Vista

2024

Helton Silva Bernardo

Gain Enhancement and Sidelobe Level Reduction of Rectangular Microstrip Patch Antenna Under Operation of High-Order Modes

Dissertation presented to the School of Engineering of São Paulo State University, São João da Boa Vista Campus, as a partial requirement for the Master's degree in Electrical Engineering within the Graduate Program in Electrical Engineering.

Concentration Area: Electronic Systems

Advisor: Prof. Dr. Rafael Abrantes Penchel
Co-advisor: Prof. Dr. Guilherme Simon da Rosa

São João da Boa Vista
2024

B523g

Bernardo, Helton Silva
Gain enhancement and sidelobe level reduction of rectangular microstrip patch antenna under operation of high-order modes / Helton Silva Bernardo. -- São João da Boa Vista, 2024
95 p. : il., tabs.

Dissertação (mestrado) - Universidade Estadual Paulista (UNESP), Faculdade de Engenharia, São João da Boa Vista
Orientador: Rafael Abrantes Penchel
Coorientador: Guilherme Simon da Rosa

1. Antenas de microondas. 2. Ondas eletromagnéticas. 3. Sistemas de comunicação sem fio. I. Título.

Sistema de geração automática de fichas catalográficas da Unesp. Biblioteca da Universidade Estadual Paulista (UNESP), Faculdade de Engenharia, São João da Boa Vista. Dados fornecidos pelo autor(a).

Essa ficha não pode ser modificada.

Potential Impact of This Research

This research promotes technological advancements that transform wireless connectivity by integrating innovation and sustainable development. Focused on microstrip antennas, it offers solutions that enhance performance, essential for internationalization and technological integration. It increases efficiency in smart city and industrial infrastructures, aligning with SDGs 9 and 11.

Impacto potencial desta pesquisa

Esta pesquisa promove avanços tecnológicos que transformam a conectividade sem fio, integrando inovação e desenvolvimento sustentável. Focada em antenas de microfita, oferece soluções que melhoram o desempenho, essenciais para a internacionalização e inserção tecnológica. Aumenta a eficiência em infraestruturas de cidades inteligentes e indústrias, alinhando-se aos ODS 9 e 11.

Impacto Potencial de Esta Investigación

Esta investigación fomenta avances tecnológicos que transforman la conectividad inalámbrica al integrar la innovación y el desarrollo sostenible. Centrada en las antenas microstrip, ofrece soluciones que mejoran el rendimiento, esenciales para la internacionalización y la integración tecnológica. Aumenta la eficiencia de las infraestructuras de ciudades inteligentes e industriales, alineándose con los ODS 9 y 11.

Impact Potentiel de Cette Recherche

Cette recherche favorise des avancées technologiques qui transforment la connectivité sans fil en intégrant innovation et développement durable. Axée sur les antennes à microfentes, elle propose des solutions améliorant les performances, essentielles pour l'internationalisation et l'intégration technologique. Elle accroît l'efficacité des infrastructures des villes intelligentes et industrielles, en accord avec les ODD 9 et 11.

This "impact reflection page" is required by ordinance UNESP N. 117/2022 and AT/PROPG N. 02/2022.

UNIVERSIDADE ESTADUAL PAULISTA

Câmpus de São João da Boa Vista

CERTIFICADO DE APROVAÇÃO

TÍTULO DA DISSERTAÇÃO: Gain Enhancement and Sidelobe Level Reduction of Rectangular Microstrip Patch Antenna Under Operation of High-Order Modes

AUTOR: HELTON SILVA BERNARDO
ORIENTADOR: RAFAEL ABRANTES PENCHEL
COORIENTADOR: GUILHERME SIMON DA ROSA

Aprovado como parte das exigências para obtenção do Título de Mestre em Engenharia Elétrica, área: Sistemas Eletrônicos pela Comissão Examinadora:

Prof. Dr. RAFAEL ABRANTES PENCHEL (Participaçao Virtual)
Departamento de Engenharia Eletronica e de Telecomunicacoes / Faculdade de Engenharia de Sao Joao da Boa Vista UNESP

Prof. Dr. IVAN ARITZ ALDAYA GARDE (Participaçao Virtual)
Departamento de Engenharia Eletronica e de Telecomunicacoes / Faculdade de Engenharia de Sao Joao da Boa Vista UNESP

Prof. Dr. RENAN ALVES DOS SANTOS (Participaçao Virtual)
Faculdade de Engenharia Elétrica / Universidade Federal de Uberlândia

Profª. Drª. ARIANA MARIA DA CONCEIÇÃO LACORTE CANIATO SERRANO (Participaçao Virtual)
Escola Politécnica (EP) / Universidade de São Paulo (USP)

São João da Boa Vista, 06 de agosto de 2024

Faculdade de Engenharia - Câmpus de São João da Boa Vista -
Profª Isette Corrêa Fontão, 505, 13876750, São João da Boa Vista - São Paulo
http://www.sorocaba.unesp.br/#!/pos-graduacao/--engenharia-eletrica-local/CNPJ: 48031918004111.

CC BY-NC 4.0 LEGAL CODE

Attribution 4.0 International

Sincere thankfulness to...

In brief words, I thank my family for their support.

I would like to express my gratitude for the recommendation letters from Professors Elias Oliveira, Serginei Liberato, and Fernando Neto from the Federal Rural University of Pernambuco (UFRPE). I sincerely appreciate their belief in my academic potential and am deeply thankful to them.

I also wish to thank Luís Alexandre S. Tapia for his support during my incoming and my stay corner in São João and my classmate in Machine Learning. Your integration efforts were invaluable. I must also mention the CAST team: Elígia Simionato, Marcela, and Ana Júlia, for their warmth and support during my integration at Unesp.

Special thanks to Prof. Guilherme S. da Rosa for accepting the academic mission as my co-advisor. It has been a great pleasure to learn from you and receive your guidance and knowledge.

I would like to extend my gratitude, especially to Prof. Renan A. dos Santos, a prominent researcher in higher-order modes, whom both my advisor and I have had the privilege to acknowledge. As I have said before and will repeat: "*We drink from this source*".

Finally, I am thankful to Prof. Rafael A. Penchel for believing in my work and potential. Thank you for your advice, teachings, and technical guidance. Your patience and ability to explain complex concepts have been invaluable to my learning journey, as I understand things from various perspectives.

Acknowledgements

This study was financed in part by the Coordenação de Aperfeiçoamento de Pessoal de Nível Superior – Brasil (CAPES) – Finance Code 001.
This research is supported by grant numbers 88887.885627/2023-00 and 88887.953339/2024-00.

Abstract

Emerging technologies are revolutionizing the market with advanced devices and increased data transmission power, thereby enhancing wireless connectivity performance. Furthermore, microstrip patch antennas (MPAs) are lightweight, compact, and can be easily integrated into flat surfaces, making them ideal for mobile devices and embedded communication systems, providing higher gain and directivities on higher-order modes. But, this operation involving higher sidelobe levels that it is problematic issue. In order to mitigate these problem, we propose two easy and simplest techniques: using slots and stubs method and permittivity analysis. Moreover, our study proposes an MPA operating in the TM_{50}-like mode to achieve higher gain and lower sidelobe levels. Our methodology involves altering the surface current distribution of the resonator by introducing three sets of transverse slots at points of null electric field. We fabricated and characterized an antenna prototype resonating at 7.6 GHz in the C-band. The results demonstrate an increased realized gain of 15.0 dBi and reduced sidelobe levels to approximately 15 dB. Additionally, we present another technique focusing on permittivity analysis aimed at reducing sidelobe levels by adjusting the permittivity for a microstrip patch antenna operating in the TM_{30}-mode. The findings reveal a significant reduction in sidelobe levels to -33 dB, while maintaining a constant directivity of 10 dBi—a standard value. Minor decreases were noted in both the effective area and aperture efficiency. Furthermore, we reduce the physical and effective size of the antenna in a conventional MPA project operating at 7.3 GHz. This is done to compare the performance of two evaluation methods: slots and stubs versus permittivity analysis. The gain-over-area metrics have demonstrated that the permittivity analysis yields significantly better results, showing a difference of $\frac{7}{\lambda_0^2}$ units compared to the slots and stubs method (reduced $SLL \sim 13.3$dB) method and permittivity analysis (reduced $SLL \sim 12.7$dB) both equivalently efficient.

Keywords: microstrip antennas; reduction of sidelobe levels; slots and stubs technique; permittivity analysis.

Resumo

As tecnologias emergentes estão revolucionando o mercado com dispositivos avançados e aumento da potência de transmissão de dados, melhorando assim o desempenho da conectividade sem fio. Além disso, as antenas de microfita (MPAs) são leves, compactas e podem ser facilmente integradas em superfícies planas, tornando-as ideais para dispositivos móveis e sistemas de comunicação embutidos, proporcionando maior ganho e diretividade em modos de ordem superior. No entanto, essa operação envolve níveis mais altos de lóbulos laterais, o que é um problema. Para mitigar esse problema, propomos duas técnicas fáceis e simples: o método de uso de fendas e stubs e a análise de permissividade. Além disso, nosso estudo propõe uma MPA operando no modo semelhante ao TM_{50} para alcançar maior ganho e níveis mais baixos de lóbulos laterais. Nossa metodologia envolve alterar a distribuição de corrente de superfície do ressonador, introduzindo três conjuntos de fendas transversais em pontos de campo elétrico nulo. Fabricamos e caracterizamos um protótipo de antena ressonando a 7,6 GHz na banda C. Os resultados demonstram um ganho realizado aumentado de 15,0 dBi e redução dos níveis de lóbulos laterais para aproximadamente 15 dB. Além disso, apresentamos outra técnica focada na análise de permissividade destinada a reduzir os níveis de lóbulos laterais, ajustando a permissividade para uma antena de microfita operando no modo TM_{30}. Os resultados revelam uma redução significativa nos níveis de lóbulos laterais para -33 dB, mantendo uma diretividade constante de 10 dBi—um valor padrão. Foram observadas pequenas reduções tanto na área efetiva quanto na eficiência de abertura. Além disso, reduzimos o tamanho físico e efetivo da antena em um projeto convencional de MPA operando a 7,3 GHz. Isso foi feito para comparar o desempenho de dois métodos de avaliação: fendas e stubs versus análise de permissividade. As métricas de ganho por área demonstraram que a análise de permissividade apresenta resultados significativamente melhores, mostrando uma diferença de 7 $1/\lambda_0^2$ unidades (inverso do comprimento de onda ao quadrado no espaço livre) em comparação com o método de fendas e stubs (SLL reduzido $\sim 13,3$ dB) e a análise de permissividade (SLL reduzido $\sim 12,7$ dB) ambos igualmente eficientes.

Palavras-chave: antenas de microfita; redução de níveis de lóbulos laterais; técnica de fendas e tocos; análise de permissividade.

Resumen

Las tecnologías emergentes están revolucionando el mercado con dispositivos avanzados y un aumento de la potencia de transmisión de datos, mejorando así el rendimiento de la conectividad inalámbrica. Además, las antenas de parche de microcinta (MPAs) son ligeras, compactas y pueden integrarse fácilmente en superficies planas, lo que las hace ideales para dispositivos móviles y sistemas de comunicación integrados, proporcionando mayor ganancia y directividad en modos de orden superior. Sin embargo, esta operación implica niveles más altos de lóbulos laterales, lo que es un problema. Para mitigar este problema, proponemos dos técnicas fáciles y simples: el método de uso de ranuras y stubs y el análisis de permitividad. Además, nuestro estudio propone una MPA operando en el modo similar a TM_{50} para lograr mayor ganancia y niveles más bajos de lóbulos laterales. Nuestra metodología implica alterar la distribución de corriente superficial del resonador, introduciendo tres conjuntos de ranuras transversales en puntos de campo eléctrico nulo. Fabricamos y caracterizamos un prototipo de antena que resuena a 7.6 GHz en la banda C. Los resultados demuestran un aumento de la ganancia realizada de 15.0 dBi y una reducción de los niveles de lóbulos laterales a aproximadamente 15 dB. Además, presentamos otra técnica centrada en el análisis de permitividad destinada a reducir los niveles de lóbulos laterales ajustando la permitividad para una antena de parche de microcinta que opera en el modo TM_{30}. Los resultados revelan una reducción significativa en los niveles de lóbulos laterales a -33 dB, manteniendo una directividad constante de 10 dBi, un valor estándar. Se observaron disminuciones menores tanto en el área efectiva como en la eficiencia de apertura. Además, reducimos el tamaño físico y efectivo de la antena en un diseño convencional de MPA operando a 7.3 GHz. Esto se hizo para comparar el rendimiento de dos métodos de evaluación: ranuras y stubs frente al análisis de permitividad. Las métricas de ganancia por área demostraron que el análisis de permitividad arroja resultados significativamente mejores, mostrando una diferencia de 7 $1/\lambda_0^2$ unidades (inverso de la longitud de onda en el espacio libre al cuadrado) en comparación con el método de ranuras y stubs (SLL reducido $\sim$ 13.3 dB) y el análisis de permitividad (SLL reducido $\sim$ 12.7 dB), ambos igualmente eficientes.

Palabras-clave: antenas de microtarja; reducción de niveles de lóbulos laterales; técnica de ranuras y stubs; análisis de permitividad.

Résumé

Les technologies émergentes révolutionnent le marché avec des dispositifs avancés et une puissance de transmission de données accrue, améliorant ainsi les performances de la connectivité sans fil. De plus, les antennes patch microstrip (MPAs) sont légères, compactes et peuvent être facilement intégrées sur des surfaces planes, ce qui les rend idéales pour les appareils mobiles et les systèmes de communication intégrés, offrant un gain et des directivités plus élevés sur les modes d'ordre supérieur. Cependant, cette opération implique des niveaux de lobes latéraux plus élevés, ce qui pose un problème. Pour atténuer ce problème, nous proposons deux techniques simples et faciles : l'utilisation de la méthode des fentes et stubs et l'analyse de la permittivité. De plus, notre étude propose une MPA fonctionnant dans un mode similaire au TM_{50} pour obtenir un gain plus élevé et des niveaux de lobes latéraux plus faibles. Notre méthodologie consiste à modifier la distribution du courant de surface du résonateur en introduisant trois ensembles de fentes transversales aux points de champ électrique nul. Nous avons fabriqué et caractérisé un prototype d'antenne résonnant à 7,6 GHz dans la bande C. Les résultats montrent une augmentation du gain réalisé de 15,0 dBi et une réduction des niveaux de lobes latéraux à environ 15 dB. De plus, nous présentons une autre technique centrée sur l'analyse de la permittivité visant à réduire les niveaux de lobes latéraux en ajustant la permittivité pour une antenne patch microstrip fonctionnant en mode TM_{30}. Les résultats révèlent une réduction significative des niveaux de lobes latéraux à -33 dB, tout en maintenant une directivité constante de 10 dBi, une valeur standard. Des diminutions mineures ont été notées à la fois dans la surface efficace et l'efficacité d'ouverture. En outre, nous réduisons la taille physique et effective de l'antenne dans un projet conventionnel de MPA fonctionnant à 7,3 GHz. Cela est fait pour comparer les performances de deux méthodes d'évaluation: les fentes et stubs versus l'analyse de la permittivité. Les métriques de gain par surface ont démontré que l'analyse de la permittivité donne des résultats nettement meilleurs, montrant une différence de 7 $1/\lambda_0^2$ unités (longueur d'onde inverse au carré dans l'espace libre) par rapport à la méthode des fentes et stubs (réduction du $SLL \sim 13,3$ dB) et l'analyse de la permittivité (réduction du $SLL \sim 12,7$ dB), toutes deux équivalentes en efficacité.

Mots-clés: antennes à microfente; réduction des niveaux de lobe latéral; technique des fentes et des stubs; analyse de la permittivité.

List of Figures

Contents

1 Introduction

New technologies are emerging in the marketplace with innovative devices and higher data transmission power, enhancing wireless connectivity performance. In this brief introductory chapter, we explore the increasing demand from major companies around the world and how they are investing in these technologies. Additionally, we explain the transmission limitations of certain operational bands and alternatively solutions like higher performance microstrip patch antennas (MPAs), as we can see in Fig. 1.

Figure 1. Relationship in the cycle of connectivity demand, transmission limitations, and the role of MPAs in providing high-performance solutions.

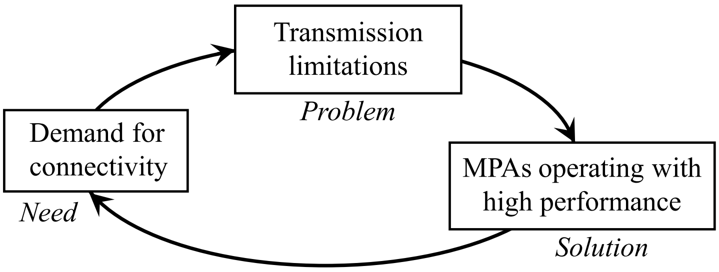

Source: author's own work (2024).

1.1 Global Demand for Wireless Device Connectivity and Next Generation

The escalating proliferation of data traffic devices linked to cellular technologies is rapidly approaching the capacity limits in modern mobile communication networks. This growth is not solely attributed to the data traffic generated by a large number of connected devices and mobiles. Rather, it marks the advent of a new era of connectivity, characterized by escalating demands placed on established networks by major corporations and expanding consumer needs [1].

This connectivity is poised for further expansion with the globalization of current network implementations, particularly through the creation of new protocol standards for Communication Service Providers (CSPs). These standards involve the utilization of various parts of the spectrum bands, facilitating enhanced communication capabilities [2]. In recent decades, the proliferation of wireless communication devices has progressed through successive generations of technology, starting from 1G (First Generation Cellular System, 1980s), advancing to 2G (Second Generation, 1990s), 3G (Third Generation, 2000s), 4G (Fourth Generation, 2010s), and now encompassing 5G (Fifth Generation, 2020s) [3], with expectation for the advent and launch commercially of 6G (Sixth Generation, 2030s) [4] and beyond.

By 2022, 515 major telecommunications operators worldwide had made substantial investments in 5G technologies across low-, mid-, and high-band frequencies. Among these operators, 243 had successfully launched commercial 5G services globally. According to the Global System for Mobile Communications Association (GSMA), Indian telecommunication operators secured portions of frequency spectrum through auctions. In 2023, a staggering $19 billion was bid in spectrum auctions, with Reliance Jio alone acquiring $11 billion worth of spectrum in the 700-800 MHz for low-band frequencies, as well as the 1800 and 3300 MHz bands to be implemented across the entire Indian territory. In parallel, Bharti Airtel secured spectrum in the auction, investing $5.4 billion in low-band frequencies such as 900 MHz, and mid-band frequencies including 1800, 2100, and 3300 MHz for 5G technologies. Another significant player in the Indian communication sector, Vodafone Idea, invested $2.4 billion in 4G LTE (Long-Term Evolution) broadband technologies [2], as seen Fig. 2.

Figure 2. The global landscape surrounding the demand and implementation of next-generation of the wireless connectivity devices in 2022.

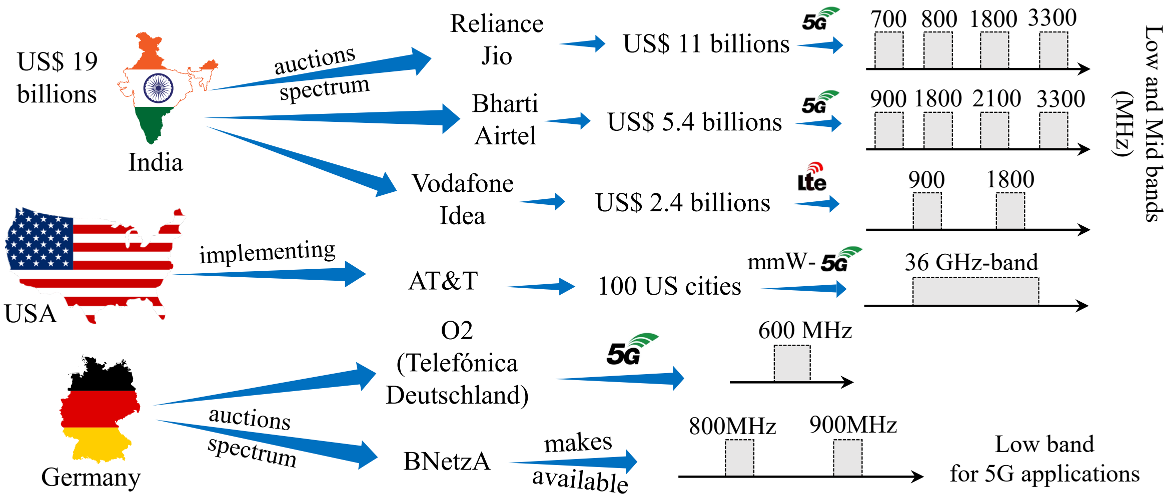

Source: author's own work (2024).

In the global landscape, the North American company AT&T (American Telephone and Telegraph) has embarked on the implementation of 5G technology services, launching in 100 cities across the United States. Leveraging millimeter wave spectrum in the 36GHz bands, AT&T is providing communication devices with high-traffic data capabilities and facilitating simultaneous connections at base station sources. Meanwhile, in Germany, O2 (Telefónica Deutschland Holding AG) has acquired low-band spectrum in the 600 MHz range to support its 5G technologies. Additionally, the German national regulator, BNetzA, has made available portions of spectrum in the 800 and 900 MHz bands for bidding in upcoming auctions [5]. These initiatives highlight the global momentum towards the deployment and optimization of 5G networks.

This flurry of investments underscores the aggressive pursuit of next-generation connectivity solutions and the strategic positioning of key players in the telecommunications landscape and globalization demands with largest network computers (Internet). The Figure 2 summaries the main idea with some operators from different countries around to world reaches and looking for allocations bands for current generation.

1.2 Transmission Problems and Limitations

With the growth and exploration of new technologies, new radio frequency bands like 4G LTE and sub-6GHz have been licensed and auctioned, resulting in a scarcity of radio spectrum [6], in particular of *L-, S-, C-* and *X*-bands, which is a significant challenge for wireless communications. This overcrowded of spectrum is given by due to service ranges and the highest demand for such growth are increasingly coming from new channels allocated in new unlicensed spectral portions. Another problem is the low homogeneity in coverage density across different regions.

In urban areas, there is a large number of connected devices and new antenna receivers and transceivers deployed through Multi-User Multi-Input-Multi-Output (MU-MIMO) systems, which are installed at a massive density to support a large number of connected users [6]. Meanwhile, in rural regions, basic transmission and reception systems are scarce, highlighting the difficulty in achieving connectivity homogenization due to the high costs involved for larger cellular telephony operators. Both in big urban centers and in far regions (rural and distant cities), there is an increasing expansion of these generations which demands overcoming barriers related to *transmission problems such as:*

- attenuation from signal transmitted;
- interference between another signals sources;
- nonlinear distortions from another undesired signals;
- multipath losses;
- and other issues [7, Ch. 2].

Alternatively, many solutions have been proposed and are changing the evolution. The physical implementation of 5G brings a diverse series of devices with enhanced electromagnetic characteristics. This is particularly important because MU-MIMO systems require multiple array antennas for transmitting multiple orthogonal signals independently to many users and in various locations.

1.3 MPAs Operating in Higher-Order Modes Like Solutions

The use of microstrip antennas in high-order modes has gained prominence due to specific requirements for gain and directivity in various modern applications [8]. When microstrip antennas operate in their fundamental mode, they offer conventional gains (in order 8dBi–9dBi) [8] and directivities that, while adequate for many situations, may fall short for more demanding requirements. To overcome this limitation, employing high-order modes allows for achieving high values of gain and directivity, similar to those obtained by *parallel arrays antennas* (which it doesn't has a equality distribution of input power along of geometry patches and these arrays need more area physical on system-on-chip) [9], *serie arrays antennas* (bigger structures of arrangement of patches and they require larger physical area of chip) [9] and *complex antenna structures* (like horn antennas that require large difficulty on construction and yours high manufacturing cost) [10]. While maintaining the inherent advantages of microstrip antennas, such as ease of manufacturing, low cost, and low profile [8].

The advantages of microstrip antennas are numerous: they are lightweight, compact, and can be easily integrated into flat surfaces, making them ideal for mobile devices and embedded communication systems. Beyond it, advantages are associated with MPAs: their compact size and low profile enable seamless integration into small-scale devices such as mobile phones, RFID tags, GPS systems, and wireless communication setups [11]. Their cost-effectiveness stems from a relatively simple manufacturing process involving printed circuit board technology. Additionally, their lightweight nature makes them particularly suitable for weight-sensitive applications in aerospace and satellite communications. The broad frequency range over which MPAs can operate underscores their versatility in various wireless communication applications, including Wi-Fi [12], Bluetooth [12], and satellite communication [13, Ch. 6, p. 392]. Furthermore, their directional radiation patterns, when paired with MPAs, offer customized patterns that promote point-to-point communication [11], thus enhancing signal transmission and reception efficiency.

Additionally, they allow for integration with printed circuits and are highly versatile in design, capable of being adjusted to operate at various frequencies. However, by operating in high-order modes, these antennas achieve higher values of gain and directivity, meeting specific demands without losing these advantageous characteristics.

Nevertheless, operating microstrip antennas in high-order modes presents challenges due to the involved electromagnetic physics. In such modes, side lobes emerge that can cause signal redundancy, signal loss due to energy being radiated in unwanted directions, and multipath problems. These side lobes not only compromise the antenna's efficiency but can also interfere with other communications, generating noise and interference.

1.4 Contributions of This Work

To address these issues and improve the performance of microstrip antennas in high-order modes, various strategies can be employed. The insertion of slots in the antenna structure can help reduce the levels of side lobes. Introducing short circuits through pins can favorably alter the radiation pattern, it involves higher complexity in construction and fabrication processes need many steps on development. The implementation of dielectric multilayer techniques can also be effective, providing more precise control over the electromagnetic field distribution, but it is require complexity understanding of phenomenon, require higher-cost and low practicality in fabrication and construction steps. Often these strategies should be combined enable microstrip antennas to retain their traditional advantages while offering high gains and directivities, essential for high-performance applications. To address these problematic issues, we have developed two techniques aimed at reducing the sidelobe level (SLL) and increasing the gain/directivity:

- **Implementation of Three Slot Sets and Stubs Insertion in a Square MPA Operating in the TM_{50}-like Mode**: This technique aims to reorganize the electric field nulls on the resonator patch. By canceling the out-of-phase components of the surface current distribution and combining all in-phase components, the method maximizes the contributions of the field in the far-field, thereby enhancing the radiation pattern.

- **Permittivity Analysis Technique in the TM_{30}-Mode Using the Conventional MPA Model**: This method involves reducing the distance between radiating slots from $3\lambda/2$ to $\lambda/2$ by increasing the permittivity. This reduction in distance helps to lower the SLL by reorganizing the electric field distribution on the patch, leading to a more efficient radiation pattern.

1.5 Organization of the Research

Ch. 1 In introduction, we brought the justification of the global demand and exploration of how larger companies are seeking new solutions through new technologies for 5G networks.

Ch. 2 A theoretical approach is proposed in the second chapter to introduce fundamental concepts such as boundary conditions, fringing effects, resonant cavity theory, far-field patterns, and the principles supported by high-order modes.

Ch. 3 In the third chapter, we designed an antenna with slots and inserted stubs to reduce sidelobe levels and achieve high gain for maximum radiation pattern enhancement in TM_{50} mode. This chapter explains the working principle and demonstrates how it enhances and improves positions nulls in the field through slot sets for maximum contribution in the far-field.

Ch. 4 In the fourth chapter, we presented the simplest analysis of changing relative permittivity for a conventional microstrip antenna while keeping the resonance frequency fixed, and demonstrated how this reduces SLL in TM_{30} mode.

Ch. 5 In this chapter, we provide the numerical comparison between two techniques, bring the radiation pattern, the metric gain over effective area and little studies between theoretical and computational performance evaluation for behavior cavity model, corrected cavity model and FEM tool.

Ch. 6 In conclusion, we have outlined the advantages and disadvantages between two techniques in terms of effectiveness and figure merit parameters shown of the methods used in this work.

2 Microstrip Patch Antenna Operating Under TM$_{m0}$-Mode

In this brief introduction, we delve into an overview of Microstrip Patch Antennas, showcasing their basic structure, key physical attributes, principal feeding methods, primary analysis techniques for determining both physical and electrical parameters for project design, and the principal kinds and types of resonator patch geometries. This theoretical chapter elucidates the fundamentals of cavity resonance, grounded in core concepts such as effective dimensions, resonance frequency, boundary conditions, and mathematical modeling of input impedance. Additionally, it explores how cavity resonance supports multiple orthogonal modes for MPA and examines the impact of these modes' order on gain, sidelobe levels, and bandwidth.

2.1 An Overview of Microstrip Patch Antennas

Microstrip Patch Antennas embody a pivotal advancement in contemporary communication systems by seamlessly integrating into printed circuits on chips, notably Systems-on-Chip (SoC) or Integrated Circuits (IC) [13, Ch. 6, p. 392]. Their planar configuration facilitates integration on flat surfaces [14], streamlining the design process for devices requiring wireless connectivity, such as aircraft or structure missiles [14], automotive systems, smartphones, smart TVs, among others [15]. MPAs inherently operate as resonant antennas, employing methods like cavity, transmission line, and coupling for their design. Their designs and performance can be characterized by factors like bandwidth and frequency, as well as radiation pattern modeling [16].

The conventional structure of a MPA comprises a substrate, typically a dielectric material characterized by its relative permittivity ϵ_r and loss tangent $\tan\delta$, in conjunction with conductor components distinguished by their conductivity, σ. The structure of the MPA features a grounded configuration, distinguished by a lower metallic conductor segment with a specified thickness t. In contrast, other planar antenna structures, such as monopoles, dipoles, and various types of antenna designed for ultra-wideband (UWB) operation [17], lack a grounded reference [18]. In the illustration in Figure 3, a conventional model for a rectangular MPA is depicted, showcasing two distinct feeding methods: the coaxial probe as depicted as in Figures 3(a) and 3(b) and transmission line as depicted as in Figure 3(c).

Fig. 3(a) depicts a dielectric structure characterized by its width W_d in the x-direction, length L_d in the y-direction, and height h in the z-direction. The region from

Figure 3. Conventional rectangular MPA on isometric view with different feeding methods at (a) coaxial probe with view of top (b) coaxial probe with view of bottom and (c) recessed inset feed by transmission line with view of top.

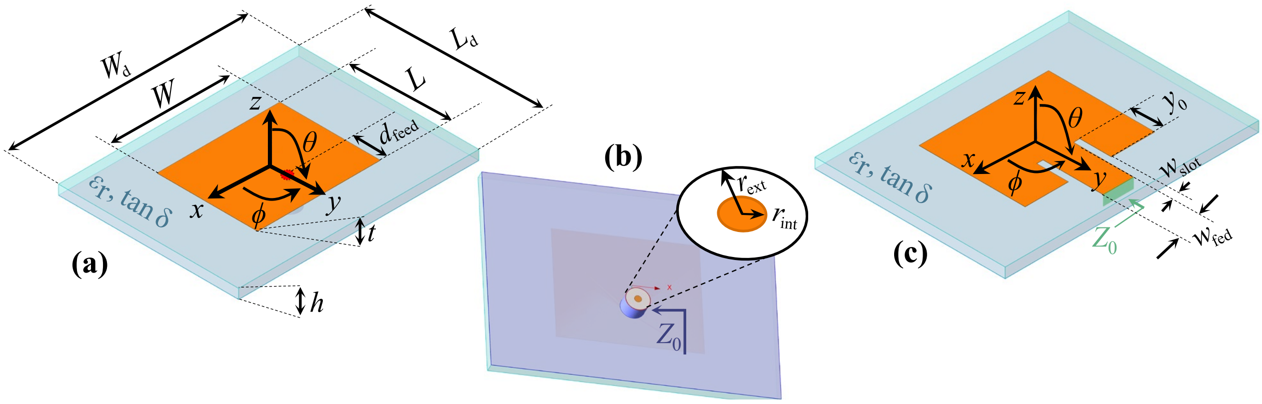

Source: author's own work (2024).

$z = 0$ to $z = t$ represents the grounded structure due to its metallic composition. From $z = t$ to $z = h + t$, the structure is characterized by a dielectric material with electrical properties represented by ϵ_r and $\tan\delta$ along the z-direction. Atop the MPA, a resonator patch is situated, comprised of metallic material with width W in the x-direction and length L in the y-direction, positioned at $z = h + t$ in the z-direction. In Figure 3(a), both Cartesian coordinates (x, y, z)-axis and spherical coordinates (θ, ϕ, r)-axis systems are illustrated, providing a comprehensive depiction of the antenna's spatial orientation.

The feeding point specified by a RF coaxial probe – commonly responsible by SMA connector (*SubMiniature version A*). Thereby, it is centered at $(0, d_{\text{feed}}, h + h_{\text{Teflon}} + 2t)$ coordinates, where a cylindrical layer of Teflon insulator surrounds the inner copper conductor and out grounded structure conductor. The height Teflon is $h_{\text{Teflon}} = 5\text{mm}$ (but it maybe varies with commercial model of SMA connector). For example, if we get a ratio of the outer ($r_{\text{ext}} = 1.675$ mm within partial Teflon isolation material) and inner ($r_{\text{int}} = 0.500$ mm for copper conductor) radii was previously calculated to provide an input impedance of $Z_0 = 50\,\Omega$:

$$\frac{r_{\text{ext}}}{r_{\text{int}}} = 3.35 \rightarrow Z_0 \approx 50\,\Omega, \tag{2.1}$$

By the use of the Equation (2.2):

$$Z_0[\Omega] = \frac{138 \log\left(\frac{r_{\text{ext}}}{r_{\text{int}}}\right)}{\sqrt{\varepsilon_{\text{insulator}}}}, \tag{2.2}$$

The matching impedance of connector antenna is proportional to ratio logarithmic of radii and inversely proportional dielectric constant of insulator $\varepsilon_{\text{insulator}}$ (in this case adopted it was Teflon). The cutoff frequency given by the relationship between external and internal radial distance of the conductor and insulator is (2.3):

$$f_{\text{cutoff}}[\text{GHz}] = \frac{11.8}{\sqrt{\varepsilon_{\text{insulator}}}\pi(r_{\text{ext}} + r_{\text{int}})}. \tag{2.3}$$

Fig. 3(c) the same MPA is presented with a different feeding mechanism using a matched microstrip transmission line for 50 Ω.

The transmission line model can be represented by MPA using two slots separated by a low-impedance transmission line of characteristic impedance Z_0 and length L [19]. The feeding method depicted in Figures 3(a) and 3(b) utilizes a coaxial probe, denoted by a red point, which traverses along the y-direction at a feed distance d_{feed}. In Figure 3(b), presented from the bottom view, the coaxial probe aligns with the characteristic impedance Z_0, as indicated by the violet arrow. Here, the white material signifies the dielectric properties, typically Teflon, characterized by the radial distance $r_{\text{ext}} - r_{\text{int}}$, representing the difference between the external and internal radial distances.

Figure 3(c) illustrates the feeding of the resonator patch via a transmission line along the y-direction at a distance y_0. This transmission line, with a width w_{fed}, incorporates slots that separate the metallic components of the resonator patch and the feeding line.

Notably, the port responsible for delivering electromagnetic energy to the system is matched with the characteristic impedance Z_0, as denoted by the green arrow. This method offers ease in fabrication and represents a straightforward approach to manufacturing processes. Moreover, MPAs boast straightforward manufacturing processes and cost-effectiveness, facilitating mass production of commercial devices. They come in various shapes including rectangular (the most prevalent), circular, triangular, square, elliptical, trapezoidal, and others, each altering radiation characteristics and influencing operational performance as per specific project requirements and analysis criteria [20]. There are several methods associated with the feeding process – coaxial probe, transmission line (microstrip), aperture coupling, proximity coupling [8, Ch. 14] as demonstrated in Table 1.

Our dissertation does not delve into methods that are not commonly utilized. However, it is noteworthy to highlight the methods that were employed, such as the coaxial probe for feeding technique, and computational tools like the Finite Element Method [21] for analysis. Additionally, only rectangular patches were considered as a type of structure in our study. The Table 1 provides a summary of various feeding techniques, analysis methods, and the main types of MPA commonly used in lectures and research to improve performance.

Important note: In this dissertation thesis, we adhere to the following convention for principal planes: the *E-plane*, which contains the maximum component of the electric field in the direction of maximum power density of the radiation vector, lies in the *yz-plane* parallel to the *radiating slots* and includes the feed source position of the antenna. Conversely, the H-plane, which contains the maximum component of the magnetic field in the direction of maximum power density of the radiation vector, lies in the *xz-plane* parallel to the *non-radiating slots* and perpendicular to the plane of the feed source position of the antenna.

Table 1. Summary of different feeding methods, analysis methods, and types/kinds of microstrip patch antenna structures.

Feeding Method	**Analysis Method**	**Comput. Analysis**	**Type/Kind of Structure**
Coaxial Probe	Cavity Resonator Model	Method of Moments (MoM)	Rectangular Patch
Microstrip Line	Circuit Model	Finite Element Method (FEM)	Rectangular Array
Aperture Coupling	Transmission Line Model	Finite Difference Time Domain (FDTD)	Circular Patch
Proximity Coupling	*Full-Wave*	Integral Equation (IE) [22]	Circular Array

Source: [8, 23, 24, 25].

2.2 Boundary Conditions on MPA Operation

To analyze the fields inside a rectangular MPA, we need to establish boundary conditions for the radiating field outlined on the dielectric box. This involves solving Maxwell's Equations within the regions where the fields exist within the box cavity. These solutions must satisfy the imposed electromagnetic field conditions. Another aspect to consider is the infinite number of discrete solutions or eigenfunctions that support various field distributions, described by integers m, n, and p, representing unique pattern configurations (or *modes*) [27, Ch. 3, p. 41]. We can understand that an infinite series of weighted modes (or eigenfunctions) satisfies these conditions through the feed of the MPA.

In any antenna operation, regardless of the mode, the objective is to receive or transmit electromagnetic signals, converting them into electrical energy and inducing current flow in the metallic conductor. In the patch configuration, the presence of a grounded surface between parallel plates allows for the propagation of waves inside the dielectric material when fed with an incident wave [26, p. 2].

The MPA is characterized using the resonance cavity method, wherein: Fig. 4(a) electromagnetic effects are extended due to effective length and increase of electrical dimensions in operation. Already on Fig. 4 (b) we can see tangential electric field lines distribution is confined by the PEC walls outlined by vector $\boldsymbol{E}$-field. We observe that as waves transition from the dielectric material to air, the tangential components $E^{\text{tang}} \approx 0$ of the field tend towards null values due to thickness of the substrate material in relation of faction of the wavelength (they're negligible), remaining components like $E_z(x, y)$, $H_x(x, y)$ and $H_y(x, y)$ only [26, p. 2]. This phenomenon results in the fringing effect on the total field [8, Ch. 14, p. 800], influenced by the boundary conditions imposed by Perfect Electric Conductor (PEC) surfaces [28][29].

Figure 4. MPA is depicted: (a) illustrating the extended length in a top view. In (b) and (c) represent the electric and magnetic field distributions, respectively. (d) The change in electrical charges. (e) The equivalent distribution of fields around boundary conditions. (f) Provides an ideal representation of the cavity model on effective permittivity bounded by E-walls. (g) 3D MPA operating.

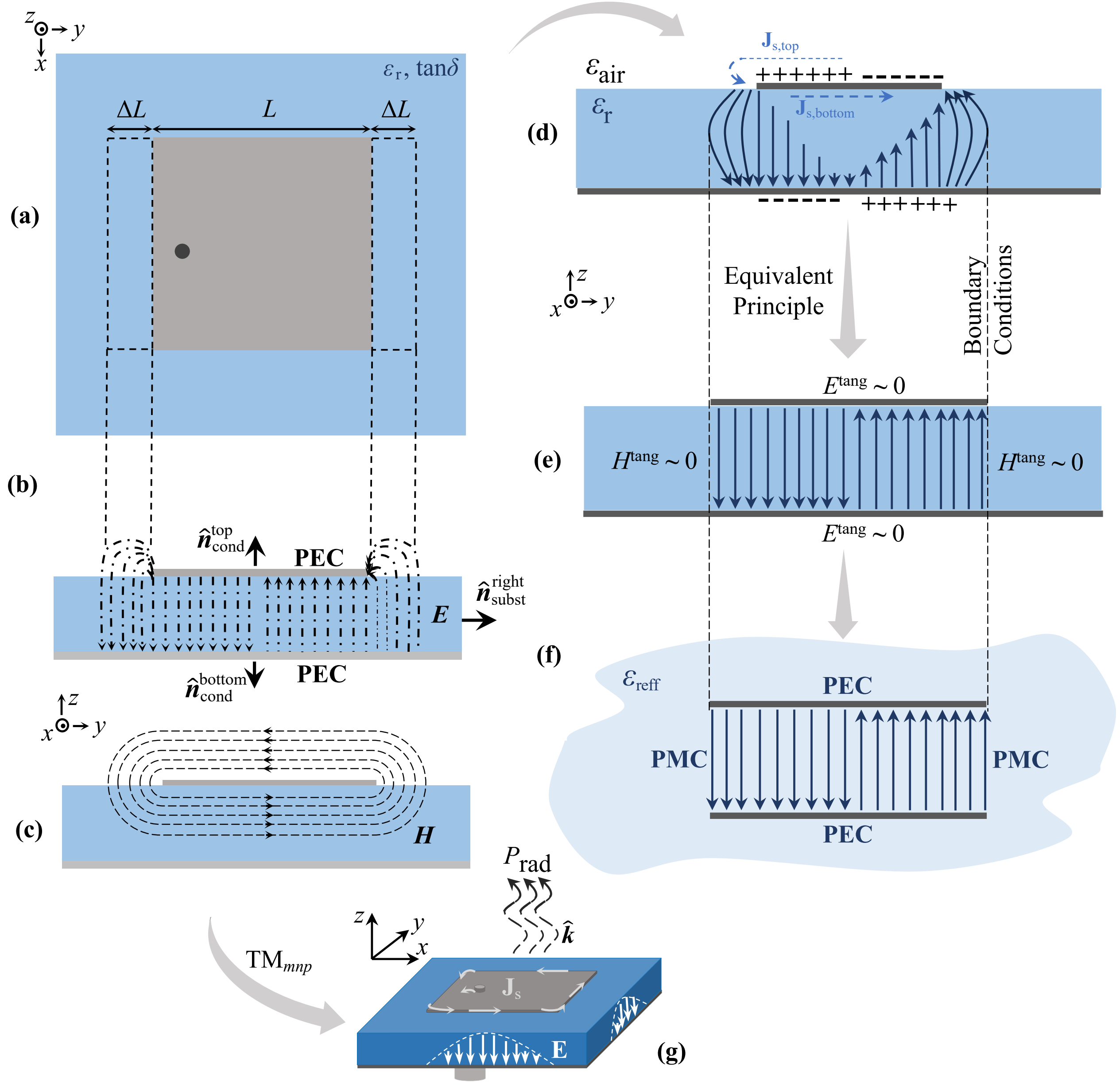

Source: author's own work with adaptations from [26, 8] (2024).

Fig. 4 (c) magnetic field distribution adheres to boundaries conditions set by H-walls. In this context, the magnetic field presents the propagation of the $\boldsymbol{H}$-field within the microstrip (resonator patch) occurs perpendicular to both the direction of maximum radiation and the $\boldsymbol{E}$-field. This is represented by a line distribution, with vectors rotationally aligned by a closed loop outlined by Perfect Magnetic Conductor (PMC). It's important to note that the $\boldsymbol{H}$-field is not parallel to the $\boldsymbol{E}$-field or the direction of maximum radiation; rather, it transversely propagates to both the $\boldsymbol{E}$-field and the direction of maximum radiation denoted by $\boldsymbol{k}$. These conditions of operation lead to the establishment of TM_{mn} modes [23, 30].

Fig. 4 (d) surface current densities $\boldsymbol{J}_{\mathrm{s}}$ result from changes in motion at the combination between top and bottom portions $\boldsymbol{J}_{\mathrm{s}} = \boldsymbol{J}_{\mathrm{s,top}} + \boldsymbol{J}_{\mathrm{s,bottom}}$, of the patch structure, expressed by Eq. (2.4):

$$\boldsymbol{J}_{\mathrm{s}} = \hat{\boldsymbol{n}}_{\mathrm{cond}}^{\mathrm{top}} \times \boldsymbol{H}, \tag{2.4}$$

the mutual exchange of charges signifies resonance through the flow of surface density from top to bottom on the resonator patch. This effect generates an electric field due to the accumulation of charges of opposite signs on the grounded structure, thereby facilitating the operation of the fundamental mode on the substrate [8, Ch. 14, p. 799]. In this moment, the effective length is close to $\lambda/2$, and the patch element starts to resonate, generating large currents associated with a specific field distribution in the structure, resembling a radiation source [26, p. 2].

We can interpret the radiation mechanism from two perspectives using the Equivalent Theorem [26, p. 2][31]:

(i) as the conducting plate (patch) as resonating with current sheet; or

(ii) as an equivalent cavity formed by parallel conducting plates (patch and grounded surface), bounded by slot-type radiators. Within this cavity, confined fields resonate at intervals of $\lambda/2$ (in the fundamental mode).

This approach can be see by Fig. 4(e) at the model that is approximated using Equivalent Principle. The boundary conditions enforce the tangential component of the magnetic field ($\boldsymbol{H}$-field) at the cavity box walls to be zero, while the electric field ($\boldsymbol{E}$-field) is forced to zero by PEC boundaries as well. As electromagnetic energy propagates through the dielectric material, a portion of this energy escapes the cavity and propagates in all directions, creating a 3D radiation pattern in space. The direction of maximum radiation, also known as the broadside direction, is in the z-direction, aligned with the $\boldsymbol{k}$-vector.

In Fig. 4(f) ideal effects are achieved by considering the effective relative permittivity within boundaries defined by PEC and PMC walls [26, p. 2]. Ideally, we can conceptualize the system of permittivities composed of air and substrate as being substituted by an effective permittivity. The cavity model outlined by the metallic walls is bounded by PEC layers on the top, also PEC layers enforce the electromagnetic imposition establishes the boundary conditions for the fields at the interface with a Perfect Conductor (an **electric wall**) resulting from the presence of a conductor atop the substrate material, according to Eq. (2.5), all electric field components must be zero on metallic surface ($\sigma \to \infty$) [32, Ch. 1, p. 14]:

$$\hat{\boldsymbol{n}}^{\text{top}}_{\text{cond}} \times \boldsymbol{E} = \boldsymbol{0}\Big|_{\text{on PEC patch}}, \text{ and} \tag{2.5}$$

$$\hat{\boldsymbol{n}}^{\text{bottom}}_{\text{cond}} \times \boldsymbol{E} = \boldsymbol{0}\Big|_{\text{on PEC ground}}, \tag{2.6}$$

where $\hat{\boldsymbol{n}}^{\text{top}}_{\text{cond}}$ and $\hat{\boldsymbol{n}}^{\text{bottom}}_{\text{cond}}$ are normal unit vectors orthogonal to metallic conductor (resonator patch) and on bottom (grounded surface), respectively. On interface between borders substrate-air, seeing thin substrate assumption (it's thickness $t \ll \lambda$), variations of fields along z are nonexistent and $\hat{\boldsymbol{n}}^{\text{top}}_{\text{cond}} \cdot \boldsymbol{J}_{\text{s}} = 0$, we got it [27, Ch. 3, p. 42]:

$$\boldsymbol{H} = -\hat{\boldsymbol{n}}^{\text{perimeter}}_{\text{cond}} J_{\text{s}}\Big|_{\text{on edge patch}}, \tag{2.7}$$

obviously J_{s} is magnitude scalar of the surface current density, and $\hat{\boldsymbol{n}}^{\text{perimeter}}_{\text{patch}}$ is unit vector orthonormal to the perimeter of the patch (on ribbon-like surface, terminology used by [31]). Alike to behavior same of PEC walls, we got alongside the PMC layers force the boundaries condition on the right and left sides (taken by **magnetic wall**), imposed by the magnetic contour must be zero on tangential $H^{\text{tang}} \approx 0$ to substrate surface [26, p. 2][27, Ch. 3, p. 42], as we can impose it [32, Ch. 1, p. 15]:

$$\hat{\boldsymbol{n}}^{\text{right}}_{\text{subst}} \times \boldsymbol{H} = \boldsymbol{0}\Big|_{\text{on PMC right-interface}}, \text{ and} \tag{2.8}$$

$$\hat{\boldsymbol{n}}^{\text{left}}_{\text{subst}} \times \boldsymbol{H} = \boldsymbol{0}\Big|_{\text{on PMC left-interface}}, \tag{2.9}$$

where $\hat{\boldsymbol{n}}^{\text{left}}_{\text{subst}}$ and $\hat{\boldsymbol{n}}^{\text{right}}_{\text{subst}}$ are normal unit vectors orthonormal to dielectric material left and right interfaces, respectively. It's important to note the alternation of fields within the enclosed cavity. Naturally, all electromagnetic energy that escapes by slot-type radiators (it's *radiating slots*) of the cavity is converted into radiated waves, constituting the electromagnetic signal.

Finally, Fig. 4(g) represents the 3D structure of the MPA, depicting the electric field distribution (tangential components) within the substrate and the surface current density on the patch resonator with circularly motion on edge of surface conductor patch. The radiation power P_{rad} computed by surface integral is given by [8]:

$$P_{\text{rad}} = \frac{1}{2} \oint_S \Re\{\boldsymbol{E} \times \boldsymbol{H}^*\} \cdot d\boldsymbol{s}. \tag{2.10}$$

Here, $\frac{1}{2}\Re\{\boldsymbol{E} \times \boldsymbol{H}^*\}$ [in W/m^2] represents the average real part of the radiation *density* of electromagnetic energy emitted by the source (antenna). This term signifies the portion of electromagnetic energy radiated away from the source. The total radiation power is composed of contributions from all infinitesimal surface elements $d\boldsymbol{s} = \hat{\boldsymbol{n}}\, da$ taken by inner product of $\frac{1}{2}\Re\{\boldsymbol{E} \times \boldsymbol{H}^*\}$. In this aspect, da represents an infinitesimal portion of the surface area and $\hat{\boldsymbol{n}}$ is the outward unit normal vector to the surface S. This radiation power is obtained by integrating over the entire surface to sum up the radiation density contributions. This electromagnetic energy radiation density propagates on TM$_{mn}$ wavesfront at $\boldsymbol{k}$-direction for configuration mode (in this case, TM$_{11}$-mode was represented and arbitrarily illustrated).

2.3 Fringing Fields and Its Contribution for Extension Effective Length

On the resonator patch, an effective radiative aperture is created by slots (both radiating and non-radiating) and extends towards the edge areas. In Fig. 5(a), the metallic conductor surface, shown in orange-white, is labeled with "slot 1," "slot 2," "slot 3," and "slot 4." Slots 1 and 3 are radiating slots, which they are separated by the length of the patch [8, Ch. 14, p. 833], while slots 2 and 4 are non-radiating. It's important to note a small extension length ΔL beyond the length L (a physical parameter). This extension is associated with the *fringing field* phenomenon observed in the operation of microstrip antennas. This effective extension length, also referred to as leakage energy radiating, allows for the escape of electromagnetic fields $\boldsymbol{E}_a$ radiated between dielectric material (blue-white) onto space [33, Ch. 21, p. 1061],[8, Ch. 14, p. 790, p. 800]. Considering a closed path labeled ABCD (as indicated in Fig. 5(b)), we can calculate the total contribution of voltage by evaluating the line integral of the $\boldsymbol{E}$-field around the loop ABCD. It's worth noting that the electric components on radiating slots "1" and "3" are $E_z = \pm E_0$, oriented along the z-axis at $y = \pm\frac{L}{2}$ (constant) [33, Ch. 21, p. 1061]:

Figure 5. Formation of the fringing fields on aperture slots radiating.

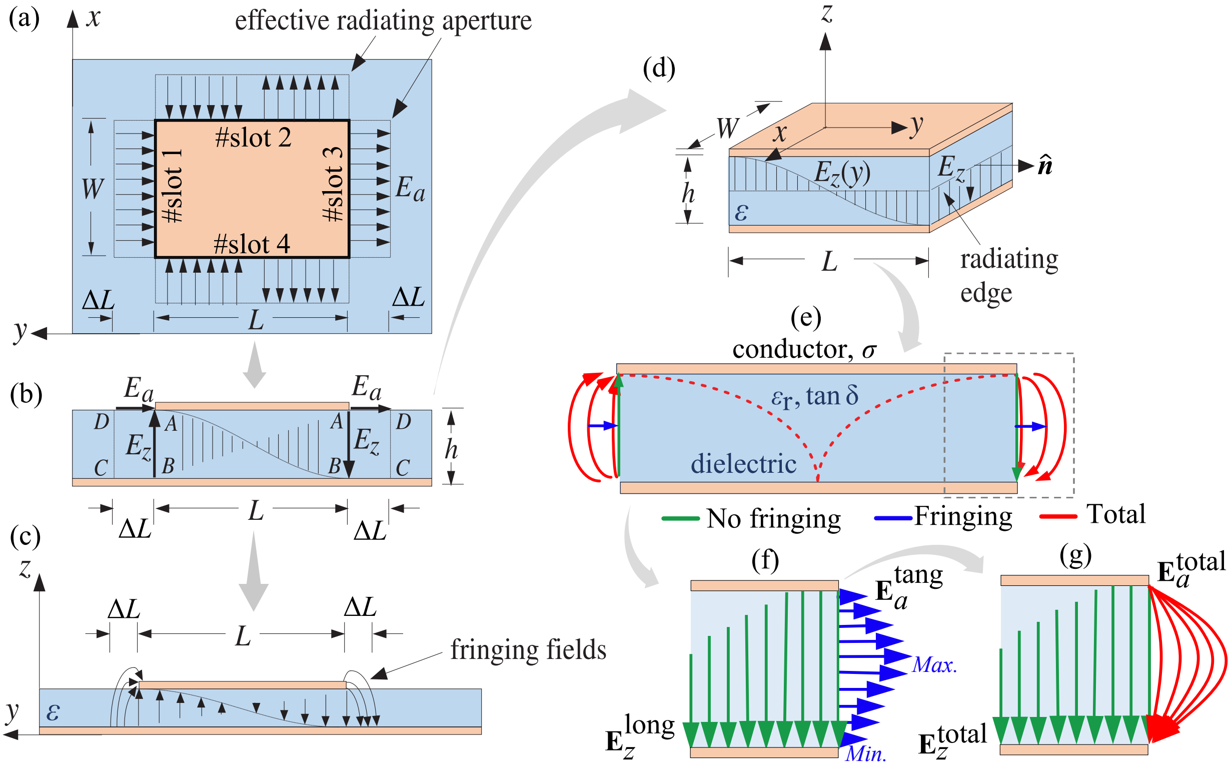

Source: author's own work with adaptations from [33, 8] (2024).

$$\oint_{\text{ABCD}} \boldsymbol{E}\cdot d\boldsymbol{l} = -E_0 h + E_a \Delta L = 0 \Rightarrow E_a = \frac{h}{\Delta L}E_0, \tag{2.11}$$

on the other hand, for the non-radiating slots “2” and “4”, the line integral computation is expressed as:

$$\oint_{\text{ABCD}} \boldsymbol{E} \cdot d\boldsymbol{l} = -E_z(y)h + E_a\Delta L = 0 \Rightarrow E_a = \frac{h}{\Delta L}E_z(y) = \frac{h}{\Delta L}E_0 \sin\left(\frac{\pi y}{L}\right). \tag{2.12}$$

Where E_0 represents the initial amplitude of the electric field from the source [in V/m]. Furthermore, the oscillating cycle induced by the non-radiating slots is dependent on the spatial coordinate y, denoted as $E_z(y)$. Another point to highlight is the relationship between the tangential component of the radiating field, E_a, and the initial amplitude E_0. This relationship is expressed as the ratio between the height and the extended length of energy leakage (this relationship is well-known and defined in Eq. (2.23)) and for some approximations $W \gg h$, we got it [34, Ch. 2, p. 58]:

$$\Delta L = \frac{h}{\sqrt{\varepsilon_{\text{reff}}}}, \tag{2.13}$$

where $\varepsilon_{\text{reff}}$ is permittivity of the system substrate-air (defined on section 2.4).

In Fig. 5(c,d), the E-field profile is depicted, reminiscent of the visualization in Fig. 4(b), illustrating the formation of fringing fields on the cut zy-plane due to a radiating edge and a substrate truncated in an isometric view. The oscillatory behavior along the y-direction completes a cycle and a constant field is observed in Fig. 5(d). As shown in Fig. 4(b) and Fig. 4(d), the electric and magnetic fields propagate through all structural materials (both dielectric substrate and air), constrained only by boundary conditions that enforce the tangential components of the electric field $\boldsymbol{E}_a^{\text{tang}}$ (shown by blue arrow at Fig. 5(e)) to zero near metallic conductors. On the other hand, $E_a^{\text{tang}} \to 0$ decreases rapidly [35]. Therefore, almost all electromagnetic radiation emanates from radiating slots at the edge of the patch due to fringing fields [33, Ch. 21, p. 1060]. However, a small amount of energy from these tangential components is emitted due to the absence of PEC at half-substrate height where the amplitude is maximum (see Fig. 5(f)). These contributions are vectorially added to the longitudinal components oscillating in the z-direction represented by $\boldsymbol{E}_z^{\text{long}}$ (green arrows as presented in Fig. 5(f) and (g)) [8, Ch. 14, p. 800]. Formally, we express the total electric field components $\boldsymbol{E}_a^{\text{total}}$ (red arrows indicated) at the edge as follows:

$$\boldsymbol{E}_a^{\text{total}} = \boldsymbol{E}_a^{\text{tang}} + \boldsymbol{E}_z^{\text{long}}. \tag{2.14}$$

It’s important to emphasize that $\boldsymbol{E}_a^{\text{total}}$ acts on radiating slots 1 and 3, between $\pm\frac{L}{2} \leq y \leq \pm\left(\frac{L}{2} + \Delta L\right)$ region, and the remaining of electric field longitudinally orientated in z-direction (under below of the resonator patch) is $\boldsymbol{E}_z^{\text{total}} = \boldsymbol{E}_z^{\text{long}}\Big|_{\text{below patch}}$ inside dielectric material.

2.4 Theory of the Cavity Resonant

A Microstrip Patch Antenna can be conceptualized as a resonant cavity, wherein the interplay of electric and magnetic fields takes place within its confines. The modal solutions, elucidated and familiarized through lectures [8], enable us to describe the electric and magnetic fields as sinusoidal manifestations of resonant factors. Furthermore, the resonant wavenumber ($k_r = \frac{2\pi}{\lambda_r}$), associated with the dispersion effect, can be expressed using the Equation (2.15) [8, Ch. 14]:

$$k_r^2 = \omega_r^2 \mu\epsilon = k_x^2 + k_y^2 + k_z^2, \tag{2.15}$$

where, ω_r is angular frequency, μ is permeability of media, ϵ is permittivity of media, and k_x, k_y, k_z are wavenumbers in (x, y, z)-axis component of dispersion vector $\boldsymbol{k}_r = k_x\boldsymbol{x} + k_y\boldsymbol{y} + k_z\boldsymbol{z}$, at resonance effect. Also, we call to attention for $\boldsymbol{k}$-vector is orthogonal to surface patch resonator (propagation of maximum radiation). Equation (2.15) establishes a relationship between the wavenumber and angular frequency, thereby determining the resonance frequency, $(f_r)_{mnp}$. Alternatively, the resonance frequency can be calculated using Equation (2.16) [8, Ch. 14, p. 802]:

$$(f_r)_{mnp} = \frac{1}{2\pi\sqrt{\mu\epsilon}} k_{mnp} = \frac{1}{2\pi\sqrt{\mu\epsilon}} \sqrt{\left(\frac{m\pi}{L}\right)^2 + \left(\frac{n\pi}{W}\right)^2 + \left(\frac{p\pi}{h}\right)^2}. \tag{2.16}$$

Where m and n are the index numbers representing multiple order modes (Transverse Magnetic TM_{mn}) supported by the cavity resonant box. Note that m and n are positive integers, and theoretically, as m and n tend towards infinity, the cavity model allows for the propagation of an infinite number of modes [30].

The propagation of electromagnetic fields influences the concentration of electric and magnetic fields confined within the cavity, resulting in an effective permittivity arising from the interaction between the mediums: air ($\epsilon_{air} = 1$) and the relative dielectric properties ϵ_r of the material. This effective permittivity is dependent on the physical geometries of the antenna and significantly affects the radiation pattern and operation of multiple modes generated by the phenomenon of infinite resonances [8].

The fringing effect in MPA introduces an extended length (electrically) due to the radiating slot predicted by the transmission line model for MPAs. Therefore, we can be calculate the effective permittivities ϵ_{reff} on both x- and y-direction, following the Eq. (2.17) and (2.18) [8, Ch. 14, p. 789]:

$$\epsilon_{\text{reff}}(L) = \frac{\epsilon_r + 1}{2} + \frac{\epsilon_r - 1}{2} \frac{1}{\sqrt{1 + 12(h/L)}}, \tag{2.17}$$

$$\epsilon_{\text{reff}}(W) = \frac{\epsilon_r + 1}{2} + \frac{\epsilon_r - 1}{2} \frac{1}{\sqrt{1 + 12(h/W)}}. \tag{2.18}$$

If $m, n \neq 0, 0$, we calculate the contributions independently [36]:

$$\epsilon_{\text{reff}}(L, W) = \frac{\epsilon_{\text{reff}}(L)\epsilon_{\text{reff}}(W)}{\epsilon_r}. \tag{2.19}$$

The extended length resulting from the effective electrical length:

$$L_{\text{eff}} = L + 2\Delta L, \tag{2.20}$$

and the width are energy leakage of radiating slots can be calculated using Equations (2.21) and (2.22) [8, Ch. 14, p. 790],[36]:

$$\Delta W = 0.412h \frac{(\epsilon_{\text{reff}}(W) + 0.3)\left(\frac{W}{h} + 0.264\right)}{(\epsilon_{\text{reff}}(W) - 0.258)\left(\frac{W}{h} + 0.8\right)}, \tag{2.21}$$

$$\Delta L = 0.412h \frac{(\epsilon_{\text{reff}}(L) + 0.3)\left(\frac{L}{h} + 0.264\right)}{(\epsilon_{\text{reff}}(L) - 0.258)\left(\frac{L}{h} + 0.8\right)}. \tag{2.22}$$

Furthermore, as [36] proposed that the effective length (and width) influence the resonance frequency. Consequently, the physical length is adjusted to account for contributions from both sides of the extended length (width), as described in Eq. (2.23) [36] with $p = 0$:

$$(f_r)_{mn} = \frac{c_0}{2\sqrt{\epsilon_{\text{reff}}(W, L)}} \sqrt{\left(\frac{m}{L + 2\Delta L}\right)^2 + \left(\frac{n}{W + 2\Delta W}\right)^2}. \tag{2.23}$$

Where c_0 is speed of light in free-space and it value $c_0 = 299,792,458$ m/s.

Another parameter that we can measure the fringing effects is fringes factor q. In another words, we consider the resonance frequency in function of length without fringing effects on dominant TM_{m00}-mode, we can rewrite Eq. (2.16) with $n = p = 0$ as [8, Ch. 14, p. 790]:

$$(f_r)_{m00} = \frac{mc_0}{2L\sqrt{\varepsilon_r}}. \tag{2.24}$$

Note that Eq. (2.24) does not take into account the edge effect. On resonance, effective length comes the patch antenna bigger electrically than its physical dimensions. We could rewrite Eq. (2.24) using Eq. (2.20), computing by [8, Ch. 14, p. 790]:

$$(f_{rc})_{m00} = \frac{mc_0}{2L_{\text{eff}}\sqrt{\varepsilon_{\text{reff}}}} = q\frac{mc_0}{2L\sqrt{\varepsilon_r}}. \tag{2.25}$$

Consequently q is outcome of length reduction factor. The fringing effect around an edge that is radiating refers to the distortion or spreading of the electromagnetic field beyond the physical boundary of the radiating element. This phenomenon occurs due to the abrupt change in the electromagnetic field at the edge, causing the field lines to curve and extend into the surrounding space. In other hand, this factor influencing the extent and magnitude of fringing include the geometry of shape patch of the radiating structure, the resonance frequency of the electromagnetic wave and the properties of the surrounding dielectric medium. Then fringing factor given by [8, Ch. 14, p. 791],

$$q = \frac{(f_{cr})_{m00}}{(f_r)_{m00}}. \tag{2.26}$$

Manipulating the Eq. (2.26) with auxiliary expressions of eqs. (2.24) and (2.25) and simplifying:

$$q = \frac{\frac{mc_0}{2L_{\text{eff}}\sqrt{\varepsilon_{\text{reff}}}}}{\frac{mc_0}{2L\sqrt{\varepsilon_r}}} \times \frac{\frac{2L\sqrt{\varepsilon_r}}{mc_0}}{\frac{2L\sqrt{\varepsilon_r}}{mc_0}} = \frac{L\sqrt{\varepsilon_r}}{L_{\text{eff}}\sqrt{\varepsilon_{\text{reff}}}} = \frac{L}{L_{\text{eff}}}\sqrt{\frac{\varepsilon_r}{\varepsilon_{\text{reff}}}}. \tag{2.27}$$

Fringing factor is inversely proportional to the effective length, and consequently to $2\Delta L$ (the extension of electric length), as observed in Equation (2.27). It is worth noting that the fringing factor is directly proportional to the square root relative permittivity and inversely proportional to the square root effective permittivity. It's noteworthy to observe the independence of the order mode on the effect of the fringing fields or a little predominantly affected on another $\text{TM}_{\text{odd-0}}$ modes, as we have analyzed the odd mode here and Eq. (2.27) translates on a outcome like it.

2.5 Electromagnetic Fields in Far-Field Region

In the *(ii)* interpretation presented in section 2.2, the equivalent cavity can be approximated by a cavity model through analytical solutions for designing the patch antenna. To find all fields, we need to solve the scalar wave Equation so that analytical solutions can be enclosed within the cavity. These solutions can be expressed through a superposition of eigenfunctions of all orthonormal-modes A_{mn} as follows:

$$E_z = \sum_{m=0}^{+\infty}\sum_{n=0}^{+\infty} E_{mn}A_{mn}, \tag{2.28}$$

certainly, these solutions are closed-forms like $A_{mn}(x, y) = \cos\left(\frac{m\pi}{W}x\right)\cos\left(\frac{n\pi}{L}y\right)$ in (x, y)-coordinates for rectangular MPA [26, p. 2]. In the far-field region, the electric and magnetic components in spherical coordinates for the θ- and ϕ-directions are well-established, and they are given by representation E_θ, E_ϕ, H_θ and H_ϕ, respectively. The radial component, E_r, tends to approach zero ($E_r \approx 0$) due to the amplitude of the component increasing with factors such as $\frac{1}{r^2}$, $\frac{1}{r^3}$, $\frac{1}{r^5}$, and so on [8]. Eq. (2.29) summarizes all expressions for the complete propagation when the plane wave is sufficiently distant from the electromagnetic source (antenna) [37, Ch. 2, p. 25].

$$\begin{array}{rcc} E_\theta &=& E_0\cos\phi f(\theta,\phi), \\ H_\phi &=& \frac{E_\theta}{\eta}\Big|_{\text{TEM polarization}}, \\ E_\phi &=& -E_0\cos\theta\sin\phi f(\theta,\phi), \\ H_\theta &=& \frac{E_\phi}{\eta}. \end{array} \tag{2.29}$$

Here, η represents the intrinsic impedance of the medium. Note that $f(\theta,\phi)$ defines the dynamic field's shape, with the expression (2.30) being a product of sine and cosine factors dependent on the electric dimensions βW and βL, and therefore, on the physical geometry of the resonator patch [37, Ch. 2, p. 25]:

$$f(\theta,\phi)=\frac{\sin\left(\frac{\beta m W}{2}\sin\theta\sin\phi\right)}{\left(\frac{\beta m W}{2}\sin\theta\sin\phi\right)}\cos\left(\frac{\beta m L}{2}\sin\theta\cos\phi\right), \tag{2.30}$$

where $\beta=\frac{2\pi}{\lambda}$ is propagation constant at far-field region. Focusing solely on define amplitude of electric component for both the E- and H-planes, which encompass the direction of maximum radiation and the electric and magnetic components, respectively, we set up the conditions for $\phi=0°$ (E-plane) and $\phi=90°$ (H-plane), as depicted by Equation (2.31):

$$\begin{aligned} E_\theta &= E_0\cos\left(\tfrac{\beta m L}{2}\sin\theta\right),\ \phi=0°. \\ E_\phi &= -E_0\cos\theta\frac{\sin\left(\frac{\beta m W}{2}\sin\theta\right)}{\left(\frac{\beta m W}{2}\sin\theta\right)},\ \phi=90°. \end{aligned} \tag{2.31}$$

We note that E_ϕ exhibits a sinc($\cdot$) behavior, with the maximum amplitude predominating at broadside propagation ($\theta=0°$), reaching a peak value of approximately $-E_0$. Similarly, when considering E_θ, it approaches E_0 at the broadside direction.

2.6 Input Impedance

In the fundamental mode, the resonance effect can be modeled by an equivalent circuit, which includes the input impedance Z_{in} given by RLC-network also, contributions from various modes can be considered in the patch cavity [38]. When $n,m=0,0$, the MPA exhibits static capacitance C_{00} and shunt resistance R_{00} due to the lossy substrate associated with the loss tangent $\tan\delta$ [39, Ch. 4].

A RLC-network is modeled as the equivalent circuit for the fundamental mode, where R_{10} represents the resistance incorporating radiation, conductor, and dielectric losses. The lumped elements C_{10} and L_{10} correspond to the capacitance and inductance associated with the resonance effect in the TM_{10} mode, as shown in Fig. 6. The high-order modes can be expressed by lumped element inductance assigned to reactance L_{mn} and exhibit high input resistance. Finally, the input impedance can be calculated using (2.32) [23, Ch. 4]:

$$Z_{\text{in}}=-j\omega\mu_0 h\sum_{m}^{\infty}\sum_{n=0}^{\infty}\frac{\epsilon_m\epsilon_n}{LW(k^2-k_{mn}^2)}\cos^2(k_m x_0)\cos^2(k_n y_0)G_{nm}. \tag{2.32}$$

Note that the input impedance Z_{in} assigns contributions from various orthogonal modes of the patch cavity [23, 38]. Where G_{mn} is a factor that results from the product of sinc($\cdot$),

Figure 6. At top view, it's represented model equivalent circuit by parallel RLC-network and bottom view it is shown an ideal behavior for reflection coefficient scattered and impedance together 3D-model for (a) square and (b) rectangular patches.

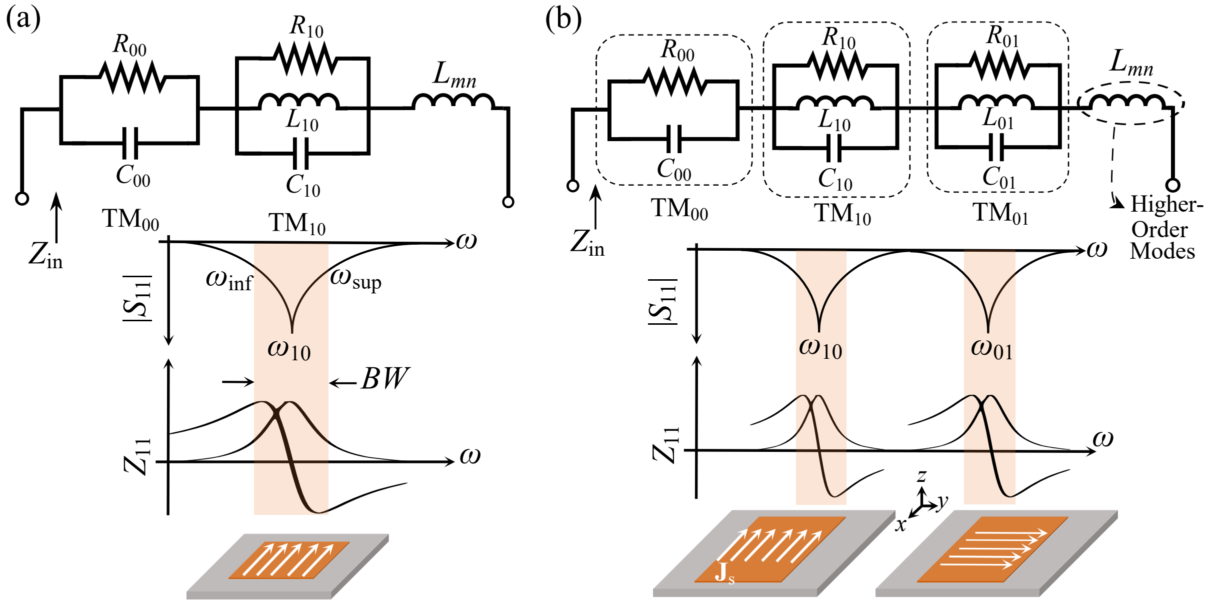

Source: author's own work (2024).

which depends on the physical width and length of the patch resonator, as well as the position of the feeding point with (x', y')-coordinates, given by Eq. (2.33) [39, Ch. 4]:

$$G_{nm} = \text{sinc}\left(\frac{m\pi x'}{2W}\right)\text{sinc}\left(\frac{n\pi y'}{2L}\right), \tag{2.33}$$

In another hand, this factor denoted by $\epsilon_{m,n}$, is defined by (2.34):

$$\epsilon_m = \begin{Bmatrix} 1 & \text{for}\, m = 0 \\ 2 & \text{for}\, m \neq 0 \end{Bmatrix}. \tag{2.34}$$

Therewith, magnitude wavenumber k represents the relationship between the wavenumber in free space k_0, the relative permittivity ϵ_r, and the loss tangent $\tan\delta$ (which accounts for dielectric losses), computed by Equation (2.35):

$$k^2 = k_0^2\epsilon_r(1 - j\tan\delta). \tag{2.35}$$

In Fig. 6, the equivalent circuit model is depicted in a top-view representation, showcasing the input impedance for various resonant modes TM_{mn}, as we show by [40, Ch. 2].

Additionally, the bottom part illustrates the scattering S_{11} and impedance Z_{11} (with input resistance and reactance) matrices for reflection, ideally facilitating transmission within the frequency band and 3D structure with surface density current $\boldsymbol{J}_s$ (in white arrow). The bandwidth BW of this transmission band is calculated using Equation (2.36) [41]:

$$BW = \left.\frac{\omega_{\text{sup}} - \omega_{\text{inf}}}{\omega_{10}}\right|_{-10\text{dB}}. \tag{2.36}$$

Note that in Fig. 6(a), a square patch resonator is depicted, where we emphasize that the TM_{10}-mode is akin to the TM_{01}-mode, as their resonant frequencies coincide. In Fig. 6(b), a rectangular patch is illustrated, showcasing both TM_{10} and TM_{01} modes, highlighting how it provides two distinct resonant frequencies.

2.7 Fundamentals and Basic Principles of Multiple High-Order Modes

2.7.1 Importance of Operation of the Higher-Order Modes for MPAs

Conventional models typically exhibit limitations such as insufficient gain (8–9 dB) and narrow bandwidth (less than 4%) [42, 30] so higher modes offer increased relative gain and directivity, but they also tend to have higher sidelobe levels. Additionally, the combination of mode operations results in a larger bandwidth compared to conventional values. The effective length is illustrated in Fig. 7(a) for the TM_{10} mode (fundamental mode). Here, we observe a minimum of the longitudinal electric field component in the z-direction within the resonator square [37, Ch. 2, pp. 23–28], where the side length approximately approaches $\lambda/2$. Atop this, there is a current flow through the surface current density $\boldsymbol{J}_\mathrm{s}$, sustaining the physical patch length L_p fixed. In Fig. 7(a), the resonator operates akin to a $\lambda/2$-wavelength dipole antenna in full mode with one maximum on center dipole antenna. This is facilitated by a linear current density J along the z-direction, completing a cycle with complementary current flow at 1/2 periodicity. This behavior aligns with the principles outlined in the multi-resonant dipole theory [43].

The increase in effective length becomes more pronounced, when we work in operation of 3th order mode compared to fundamental mode (TM_{10}), as illustrated in Fig. 7(b) for the TM_{30} mode. This behaviour (the increase of electrical dimensions) is inherent to physical nature of higher-order modes. Herein, we see three minima in the longitudinal electric field component within the resonator square [37, Ch. 2, pp. 23–28], indicating two current flows in phase and one out-of-phase current distribution cycle in the resonator center. It causes the emergence sidelobe level at E-plane with two secondary lobes undesired. This highlights a length of approximately $3\lambda/2$ (increasing the electric length), while sustaining the physical patch length L_p fixed. In Fig. 7(b), the resonator behaviour operates “like” to a $3\lambda/2$-wavelength dipole antenna. Where we notice a linear current density completing one and a half cycles with current flow at 3/2 periodicity, consistent with the multi-resonant dipole theory [43].

Thus, we observe that the increase in effective length becomes even more pronounced with larger eigenmode, such as the 3rd and 1st, as illustrated in Fig. 7(c) for the TM_{50} mode. It important to highlight that we don’t need to make any modification in conventional

Figure 7. Effective increasing of electrical dimensions on (a) TM_{10}-, (b) TM_{30}-, and (c) TM_{50}-modes with fixed constant physical length of the resonator patch ($L_p \equiv$ const.).

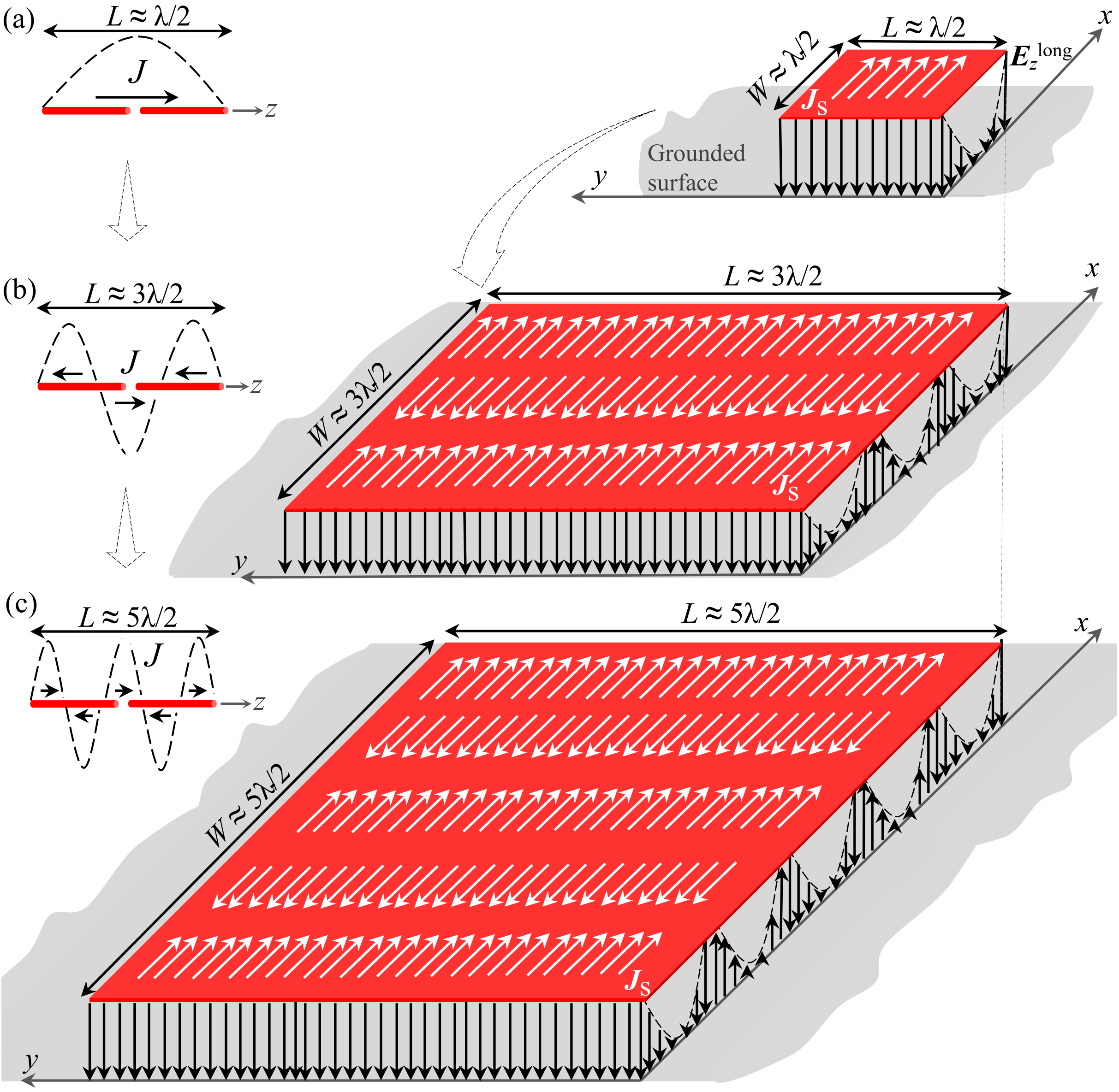

Source: author's own work (2024).

resonator patch, because this increase of electrical dimensions is inherent to operation mode. Then, we notice five minima in the longitudinal electric field component within the resonator square [37, Ch. 2, pp. 23–28], indicating three current flows in phase and two out-of-phase current distributions within the resonator. This effective increment leads to the emergence of sidelobe levels at the E-plane, accompanied by four undesired secondary lobes. Electrically, the length approximates $5\lambda/2$ (it has increased) while sustaining the physical patch length L_p fixed. In Fig. 7(c), the resonator operates similarly to a $5\lambda/2$-wavelength dipole antenna in operation mode. Hence, we observe a linear current density J completing two and a half cycles with current flow at $5/2$ periodicity.

2.7.2 Construction and Design of the MPA in High-Order Mode Operation

In general, the easy construction and fabrication processes of MPAs, combined with their low cost, lightweight, and planar nature, enable versatility and suitability for various applications [44]. While it may seem intuitive to assume that building an MPA in the fundamental mode is simpler, in practice, it can be challenging to achieve desired performance characteristics, such as bandwidth and radiation pattern, solely with the fundamental mode. Higher-order modes offer advantages in terms of bandwidth enhancement [45], pattern shaping, and versatility in antenna design. Therefore, exploring and harnessing higher-order modes can be crucial for optimizing the performance and functionality of MPAs in various applications.

MPAs operating in high-order modes often exhibit high sidelobe levels due to the nature of grid lobes that occur in all directions as we can see at Fig. 8. Consequently, the gain/directivity values increase (compared to fundamental mode) at the broadside direction at $\theta = 0°$, considering the primary lobe in the radiation pattern, but secondary lobes emerge in other non-desired directions (as shown as Fig. 8(b)–(e)). However, numerous techniques and methods exist for mitigating these issues, such as the insertion of slots [46], short pins [47], parasitic elements, modifications to the resonator combined feeding methods [48], and more.

Figure 8. Theoretical propose of conventional model operating for odd high-order (a) TM_{10}-, (b) TM_{30}-, (c) TM_{50}-, (d) TM_{70}- and (e) TM_{90}-mode. At the top, the radiation pattern format is shown, while at the bottom, the field distribution is displayed on substrate.

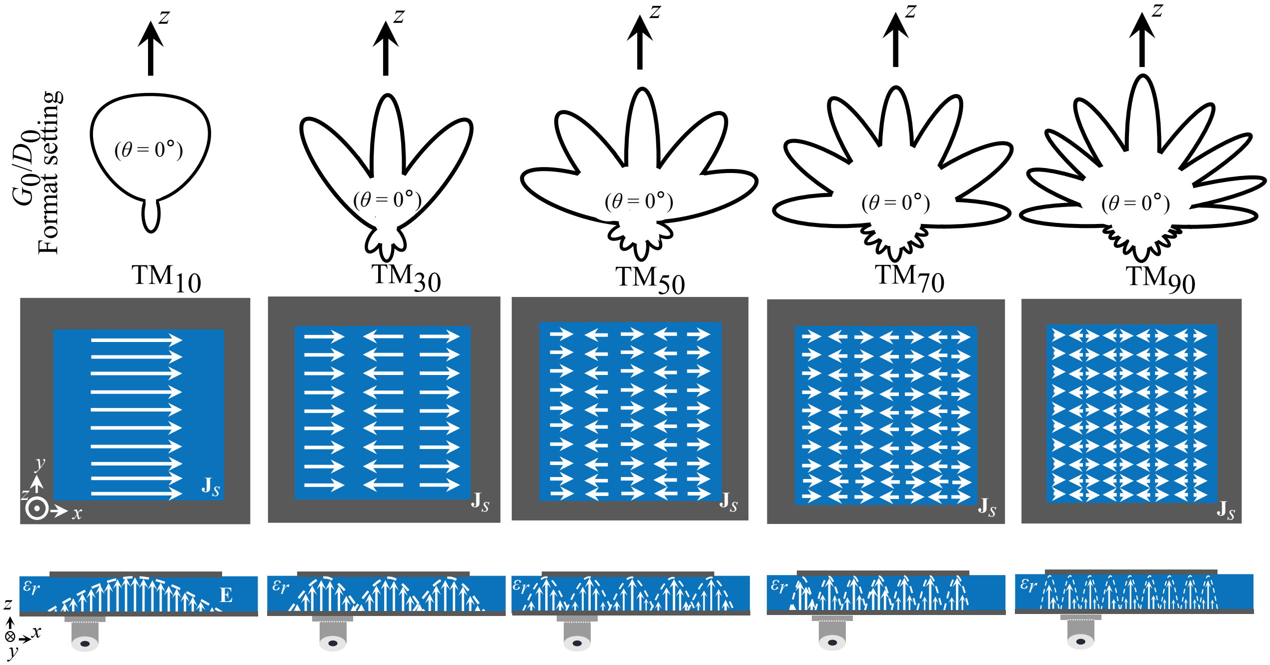

(a) **(b)** **(c)** **(d)** **(e)**

Source: author's own work (2024).

At the top, oriented broadside at $\theta = 0^\circ$ $(+z)$, it provides formatting for gain or directivity concerning the odd higher-order TM_{m0} mode. At the bottom, it illustrates the distribution of surface current $\boldsymbol{J}_s$ on the xy-plane and the electric field distribution $\boldsymbol{E}$ on the xz-plane. In Fig. 8(a) with theoretical description, the fundamental mode is described for TM_{10}, where single lobe (mainlobe) emerges at the broadside of maximum radiation. Additionally, in the same illustration, at the bottom view for the xy-plane, we can observe a distribution of surface current density with only factors in phase contributing to the radiation pattern and the unique oscillation of the electric field within the substrate, as observed in the zx-plane.

Fig. 8(b) introduces the third mode, which produces three significant lobes due to the resonant cavity, with the main lobe at $\theta = 0^\circ$ and secondary lobes in non-desired directions. At the bottom, three factors oscillate, with two counter-phase for the $\boldsymbol{J}_s$-field, similarly for the $\boldsymbol{E}$-field. In Fig. 8(c) to (e), we observe the same logic applied to TM_{m0} modes, where an increasing number of grid lobes result in multiples order modes with higher SLL limitations for MPAs.

With the theoretical Equations proposed in Section (2.5), we can plot them as shown in Fig. 9, with the θ-amplitude electric component normalized on a rectangular plot. Note that in Fig. 9(a), the normalized radiation pattern exhibits the main lobe for the E-plane (in blue color) and H-plane (in orange color), as we expected. Meanwhile, Fig. 9(b) illustrates a sidelobe level at -5dB (observing E-plane) for the second order. In Fig. 9(c), we observe expressive sidelobe levels at 0dB (observing E-plane) for the third order. When comparing the H-plane, we notice that the lobes appear to be narrower. The fifth mode (illustrated in Fig. 9(d)) exhibits more pronounced sidelobe levels compared to lower modes. We emphasize that the number of sidelobes (secondary lobes) increases and reaches higher levels when compared to TM_{30} and TM_{20}. Additionally, the H-plane shows a decrease in sidelobe levels (approaching -20dB).

To confirm our findings, we present the simulation results depicting the field distribution of surface density current $\boldsymbol{J}_s$ (bottom view) in Fig. 10(a), with the oscillation factor aligned with the phase on the xy-plane. Additionally, we verify the radiation pattern (top view) for the normalized electric component on a polar plot for the TM_{10}-mode, spanning from -90° to 90° due to the grounded surface. In this context, the effective length in fundamental mode attributes at radiating waves at patch radiator is [13]:

$$L_{\text{eff}} = \frac{\lambda}{2}\bigg|_{\mathrm{TM}_{10}}, \tag{2.37}$$

where λ is guided wavelength on substrate (dielectric material). In Fig. 10(b), the TM_{30}-mode is depicted, operating as predicted in the theoretical illustration. When the MPA operates in a non-fundamental mode, the electric dimensions typically increase, often by a

Figure 9. Normalized $|E_\theta|$ (E-plane) and $|E_\phi|$ (H-plane) at rectangular plot for radiation pattern in higher-order: (a) TM_{10}-, (b) TM_{20}-, (c) TM_{30}-, (d) TM_{50}-, (e) TM_{70}-, and (f) TM_{90}-mode.

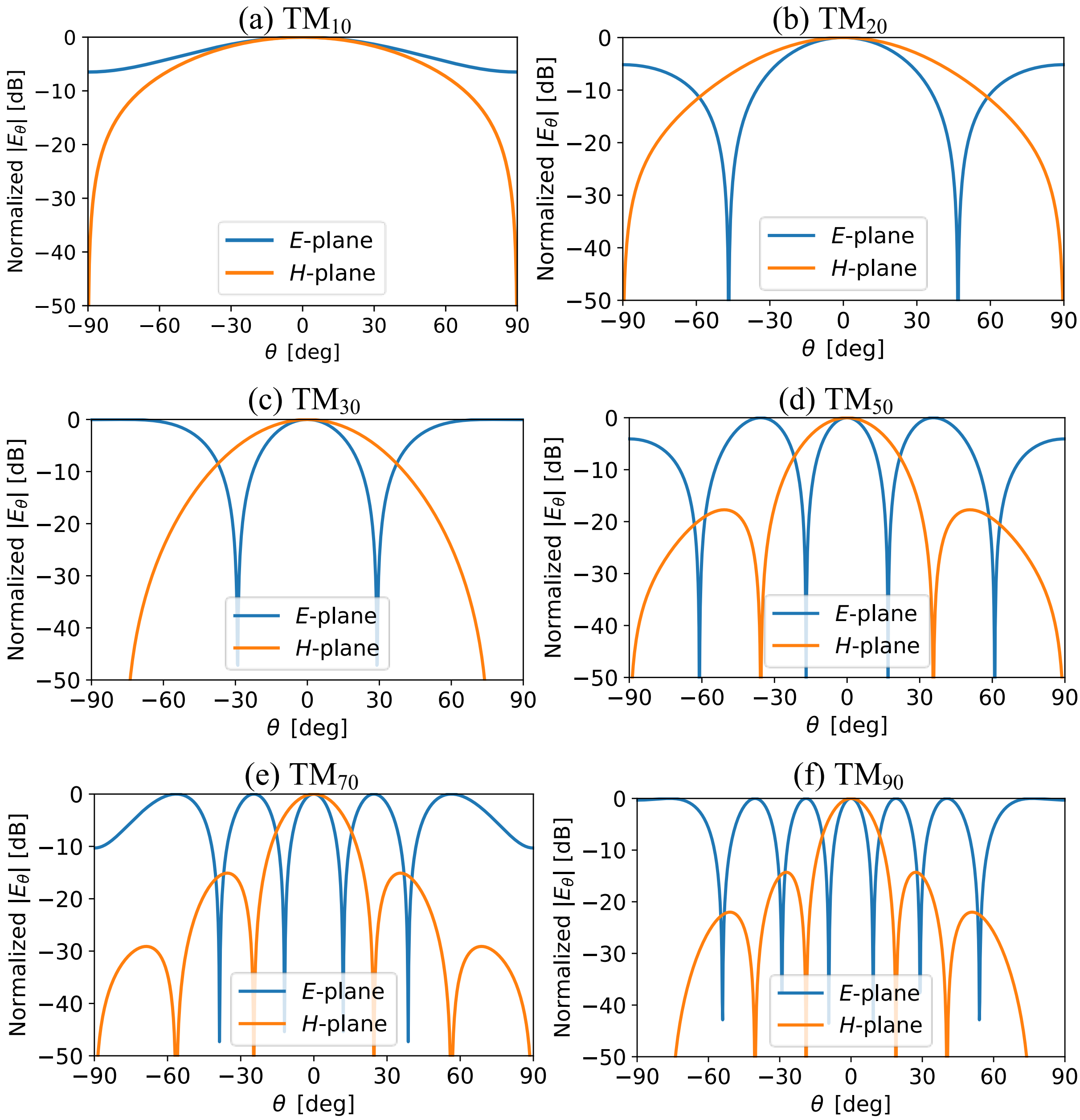

Source: author's own work (2024).

factor of m (in the case of odd modes):

$$L_{\text{eff}} = m\frac{\lambda}{2}\bigg|_{\text{TM}_{m0}}. \tag{2.38}$$

So, following through the effective length in 3rd mode is approximately $3\frac{\lambda}{2}$ [46]. As a result, the effective area, A_{eff}, scales proportionally with L_{eff}^2, approximately $A_{\text{eff}} \sim 3\frac{\lambda}{2} \times 3\frac{\lambda}{2}$, when considering a squared patch with identical width and length dimensions. In this scenario, secondary lobes with significantly high SLL values propagate in all directions according to the normalized radiation pattern. The surface density current, as shown in the bottom

Figure 10. Comparison between theoretical radiation pattern on polar plot of the (a) TM_{10}- (b) TM_{30}- (c) TM_{50}-modes and bottom it represents simulated surface current density field $\boldsymbol{J}_{\mathrm{s}}$ distribution on patch resonator.

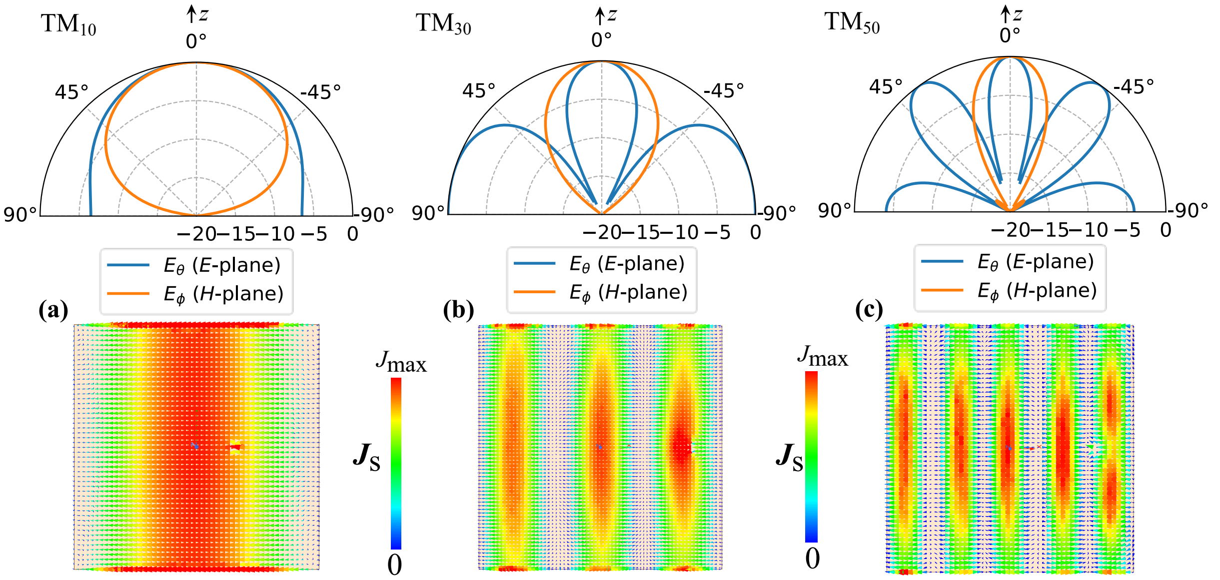

Source: author's own work (2024).

view, exhibits three oscillation factors in counter-phase. It's noteworthy that two of these factors are in phase, giving rise to the grid lobe outer of the broadside direction, which is visualized on both the polar plot and the rectangular plot in Fig. 9(c) and 8(b) under the E-plane configuration. Furthermore, we confirm that the H-plane exhibits a single main lobe at the broadside direction.

In our analysis of the TM_{50}-mode operation (illustrated in Fig. 10(c)), we simultaneously observe that all four oscillation factors are in counter-phase, resulting in a further increase in electric dimensions, proportionally, $L_{\mathrm{eff}} \sim 5\frac{\lambda}{2}$. This counter-phase distribution is evident on the resonator patch when it operates in the fifth order, producing notably four sidelobes with significantly high values in directions away from the propagation of the electromagnetic signal, as predicted in the theoretical illustration for higher modes (as referred to in Figs. 9(d) and 8(c)). In the surface density current simulation (Fig. 10), we confirm the field distribution for the surface density current. It's worth noting that there is a consideration to be made regarding the change of scale between the polar and rectangular plots. This discrepancy becomes apparent in the H-plane, where the sidelobes on the rectangular plot may appear inaccurately presented. However, upon closer inspection, we observe near -20dB on the polar plot, indicating some inner contribution of these sidelobes. It's evident that this inner contribution, although present, is not as pronounced as in the E-plane configuration. Note the pronounced presence of sidelobe levels on the H-plane at TM_{50}, TM_{70}, and TM_{90} modes, approximately at -15 dB (for sidelobes near the mainlobe). Additionally, an increase in the lateral lobes is observed compared to the mainlobe at the 5th, 7th, and 9th orders on E-plane, as depicted in Fig. 9(d), Fig. 9(e), and Fig. 9(f), respectively.

2.7.3 The Emergence of Sidelobe Levels in Each Radiation Plane

According to [37, Ch. 2, p. 26], strong sidelobe levels are observed on the E-plane due to the pattern factor (PF), denoted as $f(\theta)$, extracted by Eq. (2.31) at $\phi = 0°$. This pattern factor is proportional to the cosine function, PF $\sim \cos(\cdot)$, exhibiting numerous null as the phase varies, with m times constant argument ($m = 3, 5, 7, 9, ...$) in the aperture field. The PF introduces significant spacing between radiating edges, resulting in high SLL on the E-plane, as depicted in Fig. 11(a). As shown in Fig. 11(a), variations in phase lead to transitions, and null regions are observed on the irradiation diagram, at each scale. Consequently, maxima and minima of the electric field produce respective lobes, thereby inducing lateral lobes in undesired directions, as verified in the polar diagram in the domain of wavenumbers $k \sin\theta$.

On the H-plane, the pattern factor is proportional to the sinc function, as evident from Eq. (2.31) at $\phi = 90°$. In this context, the number of nulls is smaller compared to the cosine function, resulting in almost negligible variations in phase until TM_{30}. However, these phase variations become notable from TM_{50} onwards, for constant argument $m = 3, 5, 7, 9, ...$ [37, Ch. 2, p. 26]. Another crucial aspect to highlight in this discussion is the relatively smaller magnitude of the lateral lobes (near the mainlobe) compared to the sidelobe levels on the E-plane, derived from the cosine pattern. Consequently, the decibel scale becomes more pronounced, as depicted in Fig. 11(b).

Another explanation, it occurs due to the duality of the Fourier Transform, where the uniform aperture field and far-field patterns exhibit similarities in both cases, forming transform pairs (as observed in the sinc function) [37]. In the far-field, both on the E-plane and the H-plane, the eigenmodes are excited by the feed on the aperture resonator patch, and these weighted modes propagate with different electrical lengths.

As previously discussed, high-order modes tend to offer good gain and directivity for the main lobe, albeit with an accompanying increase in the SLL. In Fig. 12 (at E-plane), the increasing trend is readily apparent in the simulated radiation pattern for a conventional squared MPA with dimensions $W = L = 60$ mm and $W_d = L_d \simeq 1.8333L$, represented by the dashed line with circle marker and red color. Numerically, the gain of the fundamental mode is approximately 8dBi (slightly lower), while the third mode yields around 12dBi. The fifth, seventh, and ninth modes exhibit gains of 12dBi, an impressive 16dBi, and just above 15dBi, respectively. In the same depiction, we can discuss the first sidelobe level ($1^{\text{st}}\,SLL$), defined by the dashed line with square markers and blue color. Obviously, these levels begin to appear from the third mode onwards. Numerically, we observe significant values, reaching nearly 8dB for the fifth order, increasing up to approximately 12dB. There is a slight decrease to 10dB for the seventh order, and it

Figure 11. Representation of the radiation pattern linear, decibel and polar scale for (a) *E*-plane and (b) *H*-plane.

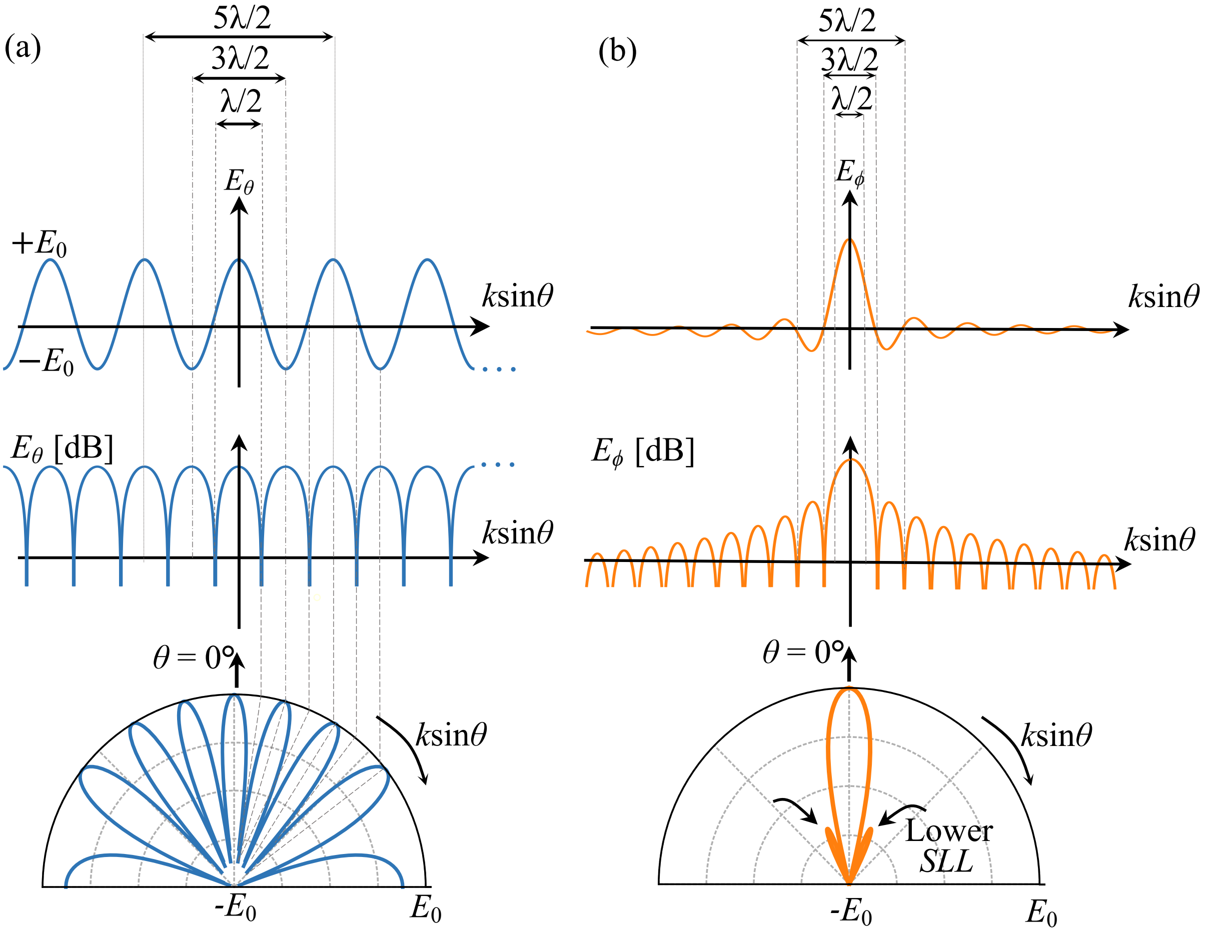

Source: author's own work (2024).

remains at 10dB for the ninth order mode, respectively.

The second sidelobe level (referred to as 2^{nd} *SLL*) is defined by the dashed line with triangular markers and orange color. It exhibits significant values, notably from the fifth order mode onwards. In the fifth order mode, the *SLL* parameters demonstrated in the simulation show lower levels, approximately around 6dB. Progressing to the seventh order, we observed that the *SLL* increases to slightly below 10dB and remains around this value for the ninth order mode.

The third sidelobe level (referred to as 3^{rd} *SLL*) is defined by the dashed line with star markers and depicted in green. In the seventh order, the *SLL* parameters demonstrated in the simulation show slightly lower levels, around $SLL \sim 8$dB. Progressing to the ninth order, we observed that the *SLL* increases to 10dB.

In the spectrum frequency band, numerous applications rely on devices and systems that employ MPA with higher gain and directivity to precisely target electromagnetic signal transmissions. These systems require the reduction of undesired secondary lobes,

Figure 12. Simulated sidelobe level and gain for odd-modes analyzed ($L = W = 60$mm; $h = 1.5$mm; $d_{\text{feed}} = 10$mm; $\epsilon_r = 2.2$ and $\tan\delta = 0.0009$).

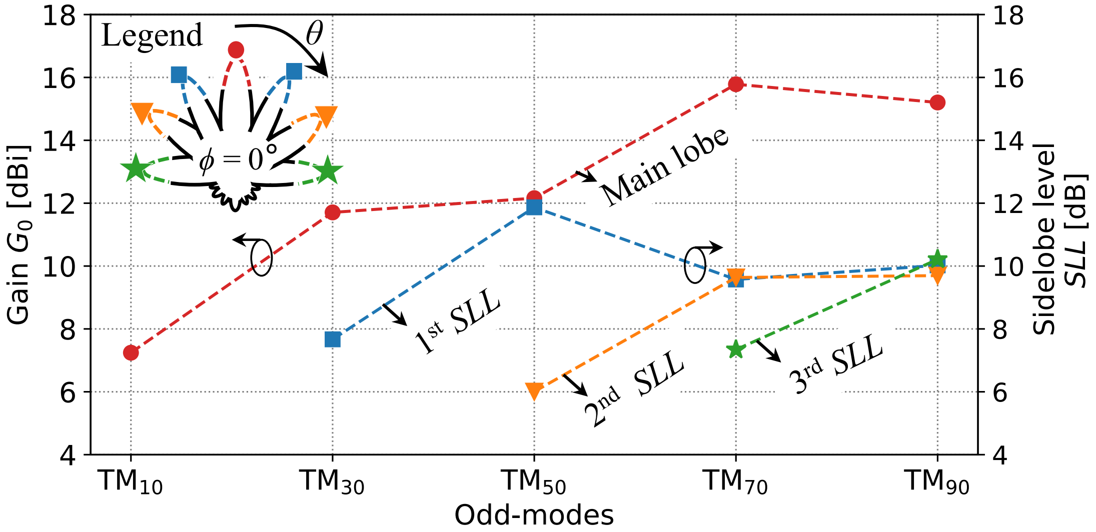

Source: author's own work (2024).

which disperse radiating energy in directions outside of the broadside. The IEEE (Institute of Electrical and Electronics Engineers) standard provides well-defined letter designations for radar bands [49, p. 10]: L-band (Long waves) in the 1 to 2GHz range, S-band (Short waves) in the 2 to 4GHz range, C-band (Compromise between S and X ranges) in the 4 to 8GHz range, X-band (X for cross, used in World War II for fire control) in the 8 to 12GHz range, and K_u-band (*Kurz*-under range, from German "short") in the 12 to 18GHz range and go on [49, p. 10]. These frequency bands play crucial roles in various applications, extending their reach and functionality.

Furthermore, we conducted simulations to analyze the peak gain in band frequency associated with odd modes, as illustrated in Fig. 13. Observing the fundamental mode (TM$_{10}$, depicted by the blue line), it is evident that it exhibits a lower peak gain of approximately 7dBi, centered around 1.6GHz. Moving to the third mode (TM$_{30}$, shown in red), we note that while its maximum gain doesn't quite reach 12dBi, it stabilizes at 11.7dBi, which is considered a satisfactory value for wireless communication and mobile links, network linkages services connected to cloud data transference like HD streaming, 3D TV [50], Bluetooth services, Global Positioning System (GPS) services focused into mobile phone satellite communications [51], it's Mobile Satellite Service (MSS) [52], that provides a wide range of services tailored for individuals, personal users, businesses, organizations in construction and environmental sectors, as well as governmental agencies and NGOs seeking precise and secure localization solutions, and it caters to developers and private sector companies, fostering innovation and partnerships across various industries in L-band frequency most used.

Compared to the fundamental mode, the third mode (indicated by red color curve

Figure 13. Simulated peak gain for odd-modes analyzed and its commercial applications ($L = W = 60$mm; $h = 1.5$mm $d_{\text{feed}} = 10$mm; $\epsilon_r = 2.2$ and $\tan\delta = 0.0009$).

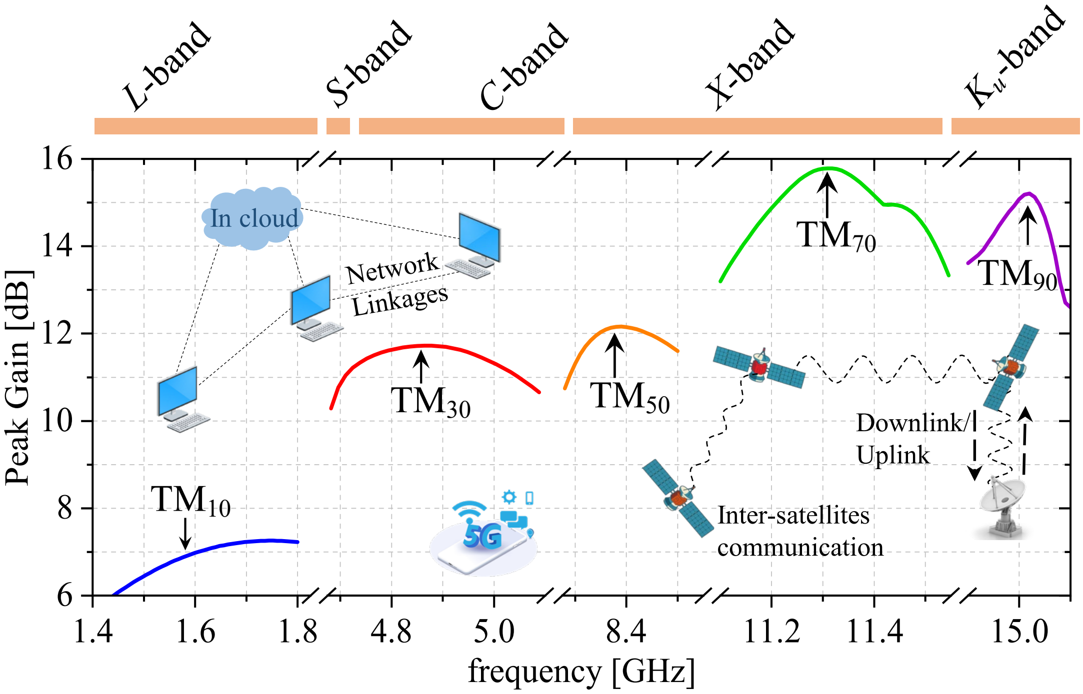

Source: author's own work (2024).

in Fig. 13) offers a wider bandwidth between 4.7–5.1GHz with a center frequency of approximately 4.9GHz, commonly used for Public Safety Communication, including police and emergency medical services, dedicated to emergency and security communication allocation bands; additionally Fixed Satellite Service (FSS), in 1960s TV networks were feeds by these allocations full-time services [51]. Nowadays, with high-connectivity, 4G LTE systems (older generation) have consolidated a wider range application, also 5G (implementing actually since 2020s year) services comes a increasing in theses spectrum bands, specifically on 5.4–5.8GHz ranges (designed C-band) incrementing and exploiting fixed wireless network antenna, mobile base stations as well as increasing monitoring and security of their structures, concomitantly, a increasing of the data traffic of these systems [50].

In the simulation of gain shown in Fig. 12 and Fig. 13, we highlight that the conventional MPA was designed to have matching impedance and a specific feeding point for the fundamental mode. Consequently, the maximum peak gain exhibited by other higher-order modes may vary from these numerical values. It is important to note that these numerical values can change depending on the matching input impedance for each order mode, the substrate material, and other parameters. Our objective was to illustrate how the peak gain behaves when different modes are simultaneously excited.

Analyzing the fifth mode (indicated by the orange color), we observe that its gain remains relatively constant, hovering near 12dBi, with a center frequency of 8.4GHz, ideal for radar systems such as weather, military, air traffic control, and marine applications, such services are widely required on X-bands frequency demands. In this context, military services works on pulsed radar warlike power to get more protection and security, this application can be extended to operative synthetic radars for ongoing weather surveillance, air and maritime traffic monitoring, and defense tracking, operating in a continuous wave mode radars [51, 52].

In the seventh mode (indicated by green color), we encounter a noteworthy peak gain of approximately 16dBi, representing a significant increase. However, the high number of sidelobes that appear poses a potential issue. Regarding the TM_{70}-mode, in this simulation, its center frequency is close to 11.3GHz. Still at X-band frequency allocations, but another services applied as commonly used for microwave links necessitating high-capacity data transmission over long distances, such as Point-to-Point (P2P) communication for device connectivity and Fixed Wireless Access (FWA), enabling broadband connectivity for homes, businesses, and other technologies. When it comes both X- while K_u-ranges provides basics services associated by the communication between satellites is commonly referred to as “inter-satellite communication” or “satellite-to-satellite communication,” it is largely used by communication enables satellites to exchange data, commands, and other information with each other, forming networks or constellations of interconnected satellites, on Broadband Satellite Services (BSS). In these scenarios, inter-satellite linkages allows to various crucial applications, including Earth observation, satellite constellations for internet access, and scientific missions, among others.

Comparing the maximum values with previous modes, we notice that the ninth mode exhibits a slightly lower gain of approximately 15dBi. Another comparison can be drawn between TM_{70} and TM_{90}, where the latter offers a narrower band, while the seventh mode provides an extended band (11.1 to 11.5GHz). Regarding the ninth mode, its center frequency is established at 15.0GHz, with this band allocation commonly used for Wireless Local Loop (WLL), providing fixed wireless access to residential and business customers, already in K_u-band allocation. In Europe, for instead, K_u downlinks is related by direct broadcast satellite services [51].

3 Gain Enhancement and Sidelobe Level Reduction of MPA Under Operation of TM_{50}-like Mode

In this chapter, a MPA operating in the TM_{50}-like mode was propose for higher gain and lower SLL. Our methodology involves modifying the surface current distribution of the resonator by introducing three groups of transverse slots at points of null electric field. We have fabricated and characterized antenna prototype for 7.6 GHz resonance frequency allocated in C-band. The results culminated in higher realized gain of 15.0 dBi and the lower SLL reduced to approximately 15 dB.

3.1 A Brief Review of Slot MPA

With the aim of overcoming the barriers associated with transmission issues mentioned in Section 1.2, we research the enhancement of radiation performance by reducing the sidelobe levels that naturally arise due to the electromagnetic nature of oscillating fields (Sec. 2.7). Then, many researchers have explored the technique of inserting slot sets on microstrip patch antennas to increase gain, directivity, and reduce undesired sidelobe levels.

In [53], a dual-band antenna operating in TM_{10} and TM_{02} mode with multilayer substrate integrated suspended line (SISL) is proposed to achieve high gain for 5G applications. One problematic issue with this strategy is the commercial difficulty of constructing multi-layer structures that combine dielectric substrates, various metallic layers, and air cavities, and still U-slot insertion on several FR4 layers. The complexity of the structure involves multiple slot insertions across different metallic layers on the patch resonators. Another point highlighted by researchers is the use of a low-cost substrate approach (FR4). Despite its non-affordability, FR4 exhibits high tangent loss ($\tan\delta \approx 0.02$), which negatively impacts the antenna gain due to the dielectric material characteristics, resulting in a relatively modest gain of approximately 8–9 dBi (as reported in their work).

In [54], a microstrip patch antenna with a fractal slot operating in TM_{30}-mode shows enhanced SLL, return loss, and improved bandwidth of notch-loaded characteristics. The principle working is based on cancelling out-of-phase currents to ensure all contribution density currents are in phase. This is achieved using a central fractal slit inserted at the center of the resonator patch (similar to the approach in [46] for reducing SLL in TM_{30}). The prototyped antenna achieves a high gain of 13 dBi and a low SLL of -16 dB. However, a problematic issue observed in this work is that a circular slot, rather than a fractal slot, results in better impedance matching (as observed in the S_{11} parameter). While the fractal shape shows better SLL reduction (SLL $\sim$ -16.1 dB), the differences between circular (SLL $\sim$ -14.6 dB) and square (SLL $\sim$ -15.5 dB) shapes are practically insignificant. Moreover, circular and square shapes are easier to fabricate and analyze compared to fractal shapes.

In [55], dual modes near TM_{30} are operated using a MPA. In this strategy, a metallic part of the resonator patch is extracted, reducing the effective length from 1.5λ to 1.25λ, which decreases the effective area (resulting in an overall size of approximately $1.31\lambda_0 \times 1.31\lambda_0 \times 0.03\lambda_0$) and consequently maintains a gain of 10.5 dBi, which is acceptable but compromised. Meanders are inserted between the remaining metallic parts to allow currents to flow from one side to the other. These dual modes combine to provide a higher bandwidth associated with the TM_{30}-like mode.

In [56], a single-layer dual-polarized differentially fed patch antenna is proposed with an insertion short-circuit pin and central slot positioned. The principle working aims to compress the TM_{30} mode in a rectangular patch with a physical length of $3L$ from $3\lambda/2 \approx 3\lambda_0/2$ to $3\lambda/2 < 3\lambda_0/2$ through short-pin and slot modifications. A problematic issue highlighted in this methodology is the difficulty of fabricating and constructing pins on the dielectric layer, involving additional processes after antenna structure fabrication. Another important consideration is the complexity of the feeding method using two coaxial points with a phase difference. The strategy is more interesting as it combines two modes (close to TM_{30}) to achieve a stable bandwidth of 6% and a gain of 9.6 dBi (conventional values).

In [46], a simple and effective method is proposed using a centrally symmetrically positioned slot on a resonator patch to reduce SLL in the TM_{30} mode and increase gain. The study explores three types of slot geometries on a square patch: a central slot, two-sided slots, and a combination of central and two-sided slots, which are implemented and analyzed. The principle approach involves canceling out-of-phase current densities through a combination of in-phase current components. The lengths of these slots have demonstrated effective reduction in SLL and significant increase in Half Power Beam Width (HPBW).

Following on this approach, the present work extends the principles working from [46] to control current distribution of the TM_{50} mode by manipulating of them and cancelling out-of-phase components; repositioning nulls in the field pattern. To achieve this, three symmetrically positioned slot configurations and stubs are proposed to extend the effective length.

3.2 Structure and Antenna Design

Initially, in conventional MPA with typical dimensions $L_d \times W_d$ for the dielectric layer (substrate), $L \times W$ for the resonator patch in the xy-plane with a 50Ω-coaxial probe fed at a distance d from the edge of the resonator patch (as seen in Fig. 14(a)), it is modified by the insertion of two symmetrically placed slots in the yz-plane. This set is composed of two slots each with dimensions $L_{s2}/2 \times W_s$ and a central slot of size $L_{s1} \times W_s$, as depicted in Fig. 14(b). In the evolutionary trend, as shown in Fig. 14(c), an identical set of slots is positioned at the center of the resonator patch, resulting in the third model analyzed. In the last situation, as depicted in Fig. 14(d), pairs of stubs are inserted at the extremities of the resonator patch. Each stub has symmetrical dimensions of $L_{st} \times W_{st}$ in the xy-plane, as illustrated in Fig. 14(d). A parametric design of the final model (designated by slots and stubs) is shown in Fig. 15.

Figure 14. MPA with different models: (a) Conventional (b) With two set of slots (c) With three set of slots and (d) With stubs.

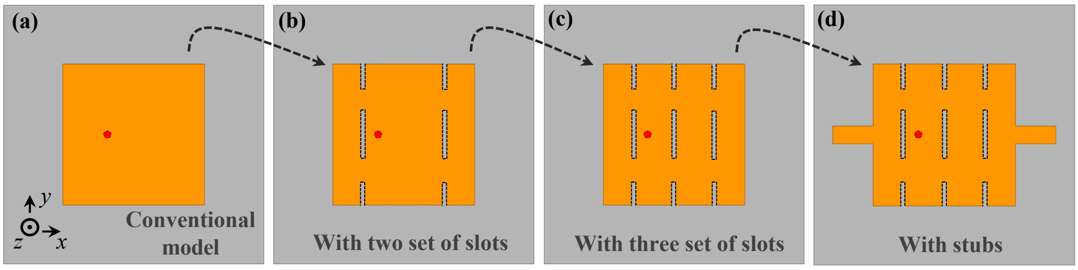

Source: [57].

Figure 15. Parametric and design model of the MPA.

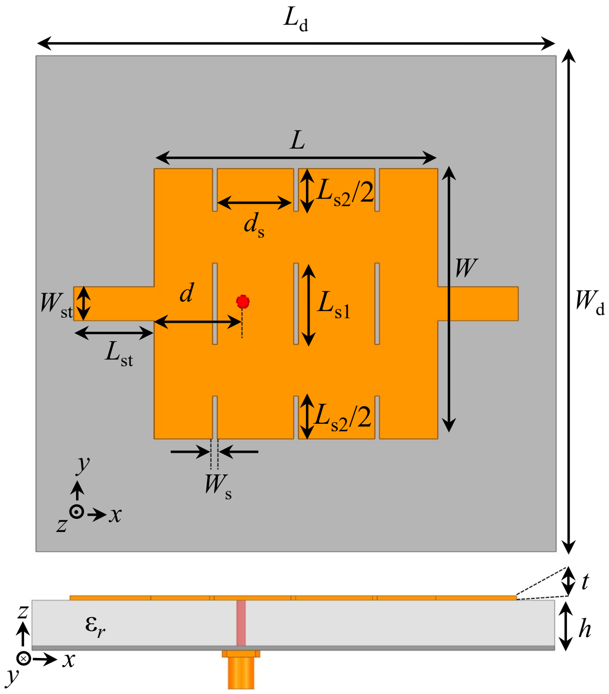

Source: [57].

In the top side of Fig. 15, the cut in the xy-plane is shown, while the bottom side of the same Fig. 15 displays the cut in the xz-plane. The structure has a height $h = 1.575$ mm for the substrate layer with permittivity $\varepsilon_r = 2.2 \pm 0.02$ and a loss tangent of $\tan\delta = 0.0009$. The copper thickness, $t = 18\mu$m, applies to both the resonator patch and the grounded structure. The substrate material used is Rogers RT/duroid 5880 dielectric. All simulations were performed in Ansys Electronics Desktop 2023 using the electromagnetic module HFSS with Finite Element Methods. Therefore, Table 2 shows the numerical values for all dimensional parametric variables of the antenna in millimeters.

Table 2. The dimensions of the proposed antenna

Description	Dimensions [in millimeters]										
Models	L	W	L_d	W_d	d	W_s	L_s1	L_s2	d_s	L_st	W_st
Conventional	60	60	110	110	19	-	-	-	-	-	-
Two set of slots	60	60	110	110	19	1	18	19	17.5	-	-
Three set of slots	60	60	110	110	19	1	18	19	17.5	-	-
Slots and stubs	60	60	110	110	19	1	18	19	17.5	17	7.5

Source: [57].

3.3 Working Principles

As explained in previous sections, the working principle is based on the work of [46], where slots are used to cancel out-phase currents in the TM_{30}-like mode. In other words, [46] transitioned from the TM_{10} mode, which has a single field null (electric field shown in Fig. 16(a)), to the TM_{30} mode, which has three field nulls (Fig. 16(b)), addressing the problematic issue of higher SLL (as highlighted in the previous chapter). The symmetric insertion of slot sets in the transversal central position promotes a reduction in sidelobe levels, and the dimensions of the slots control their magnitude. However, three field nulls are still present, as depicted in Fig. 16(c).

We adopt a similar method: Starting from the TM_{50}-mode (shown in Fig. 16(d)) with five field nulls labeled by numeration, we insert two sets of slots in symmetrical positions as depicted in Fig. 16(e). This modification aims to reduce the mode order towards a TM_{30}-like configuration (although it remains TM_{50}-like after modification) by canceling out-phase currents of the TM_{50}-mode. Subsequently, to cancel the central out-phase current, we insert another set of slots at the transversely central position (as shown in the method evolution), which contributes to the field distribution similar to the TM_{30}-mode. Finally, we introduce a set of stubs resulting in an electrical enhancement of the antenna performance without changing significantly the resonance frequency, increase the effective dimensions, as illustrated in Fig. 16(g).

Figure 16. Electric distribution on cut xz-plane for all configurations analyzed.

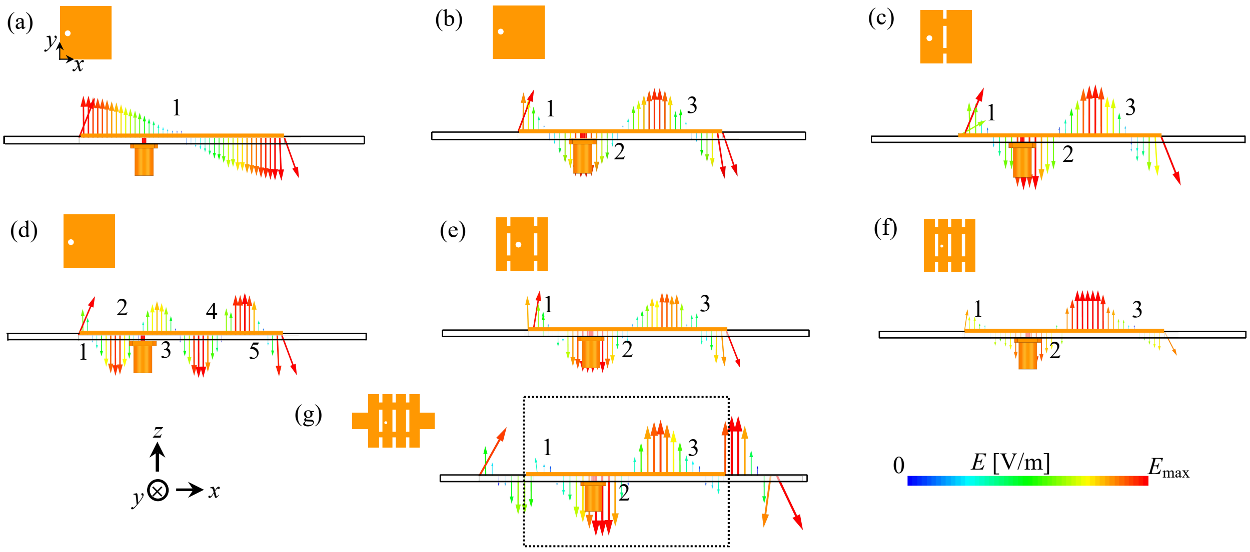

Source: [57].

3.4 Numerical Analysis of Simulation

In a normalized comparison of the directivity parameter, we observe the radiation patterns for all described models in the E-plane (depicted in Fig. 17(a)) and H-plane (seen in Fig. 17(b)). We note that in the conventional model (depicted in red), both in the E-plane and H-plane, there are higher sidelobe levels due to the nature of the TM_{50}-mode. Upon inserting two sets of slots, we achieve a slight reduction of -1.78 dB in SLL (shown in the green curve). In the H-plane, the reduction is more significant, decreasing from -6.26 dB to -14.66 dB in terms of SLL.

Figure 17. Irradiation diagram for all models MPA analyzed (a) E-plane and (b) H-plane.

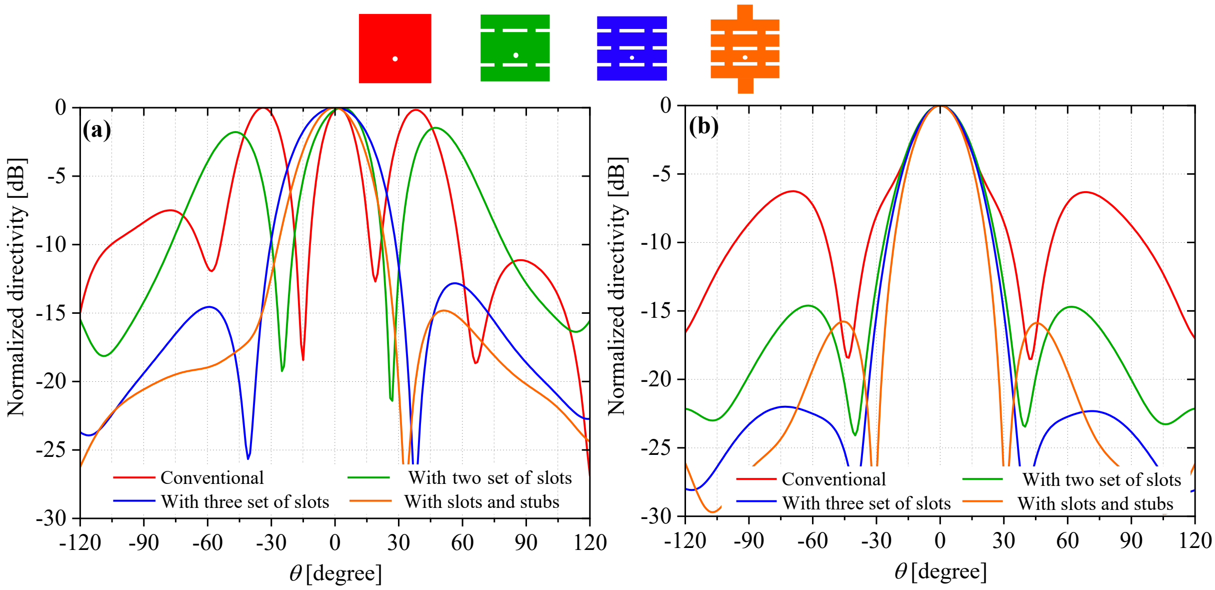

Source: [57].

In the three-slot set model, we observe a significant reduction in SLL from -1.79 dB to -14.55 dB in the E-plane and from -14.5 dB to -22.0 dB in the H-plane configuration. In the slot set and stubs model, our analysis shows a reduction from -14.5 dB to -19.0 dB in terms of SLL in the E-plane, while there is a slight increase from -22.0 dB to -15.8 dB in the H-plane. Overall, our technique demonstrates effective reduction of SLL.

Analyzing the modification involving stubs, in terms of operational bandwidth, we observe a slight improvement from 1.32% to 1.84% with a central frequency of 7.555 GHz at $|S_{11}| \leq -10$ dB. This comparison is shown between the continuous line in blue and orange colors. Regarding the realized gain, we observe that the stubs enhance the maximum peak from 14.22 dBi to 15.09 dBi when comparing both models (represented by the blue and orange dashed lines, respectively), as highlighted in Fig. 18(a).

Figure 18. Comparison between different with (a) three set of slot and stubs models and (b) all models for broadside directivity.

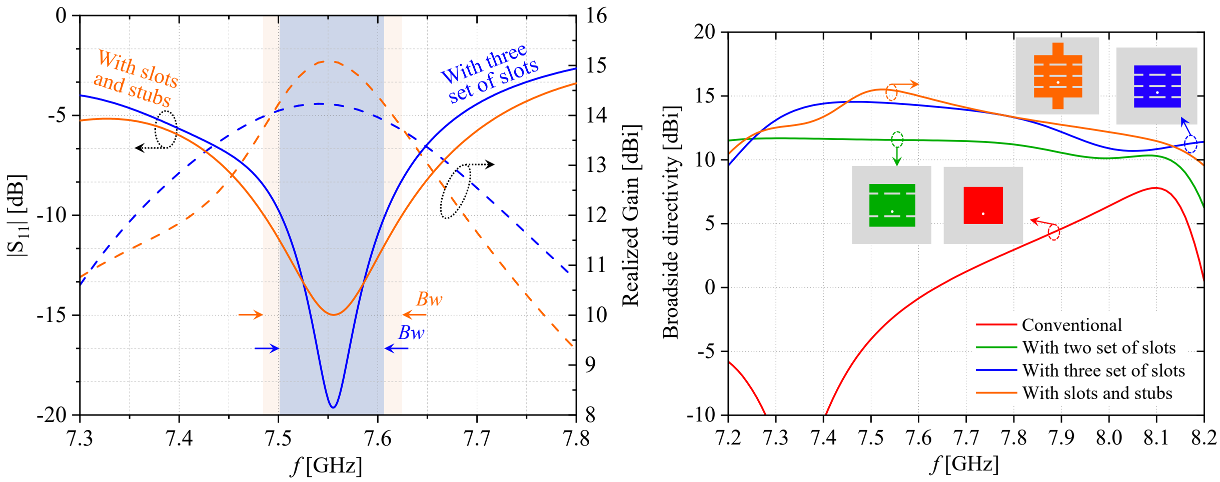

(a) Reflection coefficient and realized gain

(b) Directivity in band frequency

Source: [57].

The broadside directivity (in the maximum direction) shows enhancement when comparing all models, as observed in Fig. 18(b). Initially, the maximum directivity of the conventional model reaches 7.8 dBi at 8.1 GHz (shown in red). Upon inserting two slot sets, we observe improved flatness across all frequencies, maintaining a constant value of 11.5 dBi. Subsequently, implementing the three-slot set significantly increases the bandwidth flatness, achieving a maximum of 14.5 dBi around 7.5 GHz. Finally, inserting stubs increases the maximum peak to approximately 15.5 dBi at 7.55 GHz have a little bit of changing of 500 MHz frequency.

3.5 State-of-the-Art of Slot Microstrip Patches Antennas

Considering the current state-of-the-art, we have reviewed the literature, focusing on recent studies on slot-loaded MPAs with high-gain and reduced SLL operating in higher-order modes. Table 3 presents an overview of the overall size[1] efficiency parameter, where we have increased the effective area to $2.830\lambda_0 \times 2.830\lambda_0$ in TM_{50} while keeping the physical area constant. In comparison with [58], who utilized TM_{09}, we achieved a similar effective area ($\approx 2.920\lambda_0 \times 2.920\lambda_0$) using short-pins technique combined with slots. This observation is reflected in terms of maximum realized gain and directivity, with $G_0 = 15.0$ dBi, differing by 0.5 dBi from [58], in terms of bandwidth and efficiency aperture.

Table 3. Comparison with previous works of sidelobe-reduced and gain-enhanced higher order modes for patch antennas

Ref.	TM_{mn}-like mode	$(f_r)_{mn}$	Overall size*	G_0	D	Bw	ε_{ap}
[59]	$\text{TM}_{03}/\text{TM}_{05}$	2.60	$0.011\lambda_0 \times 1.734\lambda_0 \times 1.734\lambda_0$	-	14.6	15.20	74.13
[46]	TM_{03}	4.20	$0.022\lambda_0 \times 1.541\lambda_0 \times 1.541\lambda_0$	12.8	13.36	1.53	63.97
[60]	TM_{05}	5.96	$0.040\lambda_0 \times 1.650\lambda_0 \times 1.650\lambda_0$	11.5	11.77	3.00	44.52
[61]	$\text{TM}_{03}/\text{TM}_{05}$	5.65	$0.014\lambda_0 \times 1.319\lambda_0 \times 1.319\lambda_0$	10.7	-	6.10	53.82
[58]	TM_{09}	12.52	$0.085\lambda_0 \times 2.920\lambda_0 \times 2.920\lambda_0$	15.5	15.96	2.70	33.10
[56]	TM_{03}	5.00	$0.033\lambda_0 \times 1.334\lambda_0 \times 1.334\lambda_0$	9.6	-	6.00	40.84
[55]	TM_{03}	5.80	$0.031\lambda_0 \times 1.306\lambda_0 \times 1.306\lambda_0$	10.5	10.77	8.50	52.45
[53]	$\text{TM}_{10}/\text{TM}_{02}$	3.30	$0.059\lambda_0 \times 0.924\lambda_0 \times 0.943\lambda_0$	9.1	9.83	12.65	74.64
[54]	TM_{30}	3.09	$0.015\lambda_0 \times 1.546\lambda_0 \times 1.443\lambda_0$	13.3	-	1.94	76.40
[57]	TM_{50}	7.60	$0.040\lambda_0 \times 2.830\lambda_0 \times 2.830\lambda_0$	15.0	15.37	3.28	31.70

*Resonance frequency (f_{mn}) in GHz; Maximum realized gain (G_0) in dBi; Directivity (D) in dBi; Bandwidth (Bw), Radiation aperture (ε_{ap}) efficiency is given in percentage (%); *Overall size ($h \times W \times L$) taken by ground plane physical dimensions in λ_0^3.*

Source: [57].

In comparison to other works, we have achieved enhancements in terms of realized gain and directivity. However, concerning bandwidth and aperture efficiency, other methodologies utilizing combinations of neighboring modes have demonstrated effective operations of 15.2% and 74.13%, respectively, as shown in [59].

3.6 Characterization and Measurement of Prototype MPA

In the anechoic chamber, depicted in Fig. 19(a), the prototype was positioned on a support connected with a 50Ω-cable, with a horn antenna positioned above it (as a reference antenna) to measure the radiation pattern of the MPA in the broadside direction ($\theta = 0°$) on setting measurements. A Cartesian coordinate system x, y, z and spherical coordinates

---

[1] Here, when we call overall size, we are referring to the “effective volumetric space”.

θ, ϕ are shown on the side. The main planes (E-plane and H-plane) are indicated by green balloon, with laser systems marking their locations, as illustrated in Fig. 19(a). These measurements can be observed in Fig. 20(a) and Fig. 20(b), depicting the realized gain. In Fig. 19(b), the bandwidth measurement shows better results than the simulated model. Numerically, we observe $BW_{\text{med}} = 3.36\%$ with a central frequency of 7.63 GHz, whereas the simulated results indicate $BW_{\text{sim}} = 1.77\%$ with a central frequency of 7.58 GHz. These discrepancies may be attributed to inaccuracies in physical dimensions, numerical computation in the simulation tool, precision of measurement targets, which we aimed to resolve with $\Delta|S| = 0.01$, and other factors. Regarding the realized gain, we observed that the maximum peak in the measured model did not exceed 15 dBi, whereas the simulated model achieved peaks above the 15 dBi mark. Finally, we present the radiation patterns for the measured and simulated models of the prototype MPA in Fig. 20. Figures 20(a) and 20(b) depict the E-plane and H-plane normalized realized gain, where the co-polarization (Co-pol.) is represented by the dashed brown curve for measured data and continuous orange curve for simulated data. Cross-polarization (X-pol.) is indicated by the dashed gray line in both plots. The antenna shows a close agreement between measured and simulated prototypes for co-polarization parameters, with cross-polarization below -25 dB in both planes. It is important to highlight that below -20 dB, the measurement system lacks precision, thus unable to accurately measure these parameters.

Figure 19. Comparison between different measured and simulated models for (a) antenna measurement in the aneicoic chamber; (b) three-slot set and stubs model.

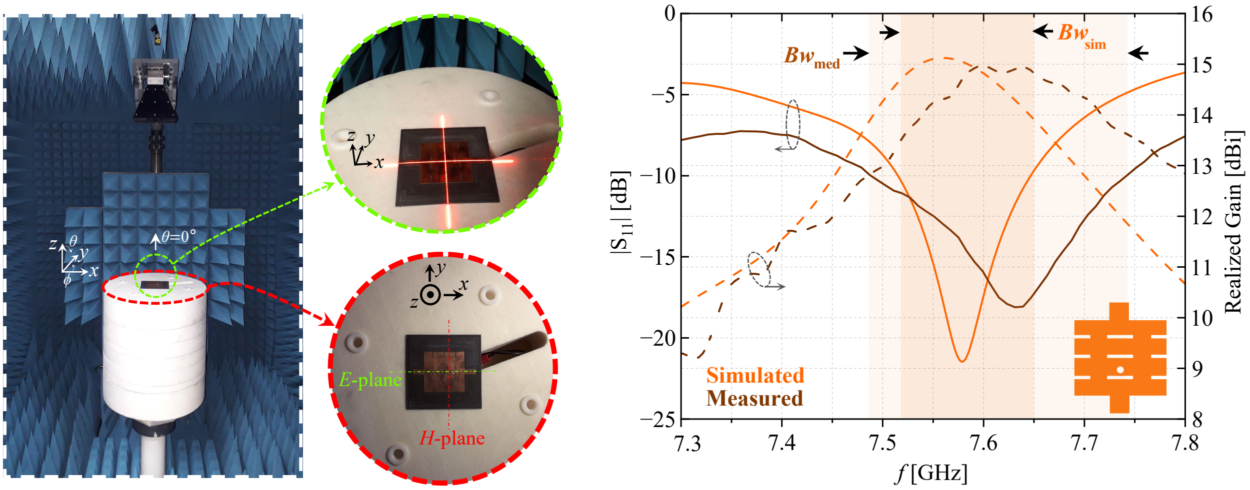

(a) Setting measurements for the antenna [57]

(b) Reflection coefficient and realized gain

Source: [57].

Figure 20. Irradiation diagram for normalized realized gain with co-polarization and cross-polarization (a) E-plane and (b) H-plane of modified model (with stubs and set slots).

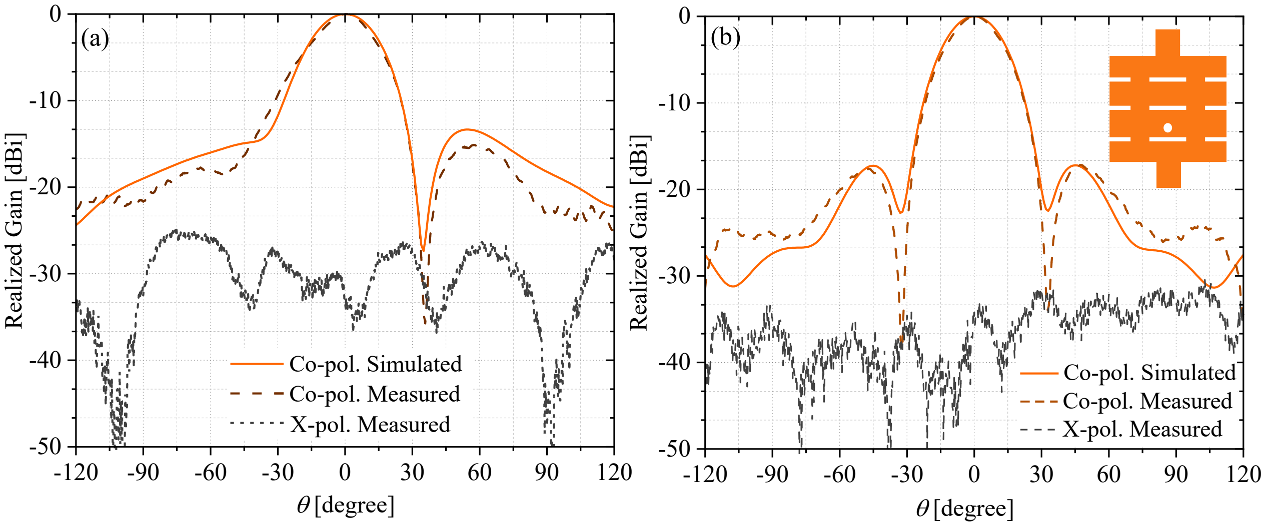

Source: [57].

4 Technique of Reduction of Sidelobe Levels in TM_{30}-Mode for Conventional MPA through Permittivity Analysis

The study of this chapter focuses on reducing sidelobe levels by analyze the variation of permittivity – *i.e.* dielectric constant effective of substrate – for a Microstrip Patch Antenna operating in the TM_{30}-mode at 5.8GHz. The results indicate a substantial reduction in sidelobe levels to -33 dB, while maintaining a constant directivity of 10 dBi—a conventional value. Minor decreases were observed in both the effective area and aperture efficiency. Moreover, a reduction in the antenna's physical area was implemented for a design project to 7.3GHz to propose of to realize comparison between slots and stubs technique.

4.1 Brief Introduction

Microstrip Patches Antennas are resonant cavity structures designed with dielectrically thick material substrates [8]. This characteristic enables the propagation of electromagnetic fields within the cavity and allows a specific quantity of the electric field to penetrate this structure. This characteristic is defined by relative permittivity (it is the selection of substrate utilized).

As a resonant antenna, higher-order modes of propagation such as TM_{mn} operations may emerge. These modes facilitate the achievement of higher gains/directivity compared to the fundamental mode (TM_{10}). The nature of these modes often results in additional grid lobes (or sidelobes) in undesired directions. Reducing these sidelobes poses a significant challenge in structural design. It requires exploring methods and forms to combine field distributions with uniform amplitudes, phases, and polarizations. This search aims to optimize the antenna performance by minimizing radiation in unwanted directions and reducing sidelobe levels SLL.

With this, it managed the higher gains and directivities antennas are essential in wireless communication (such as the Wireless Local Area Network, also called WLAN) [11] between devices due to their ability to amplify electromagnetic fields, thus significantly increasing signal strength. These antennas concentrate the irradiated energy in a specific direction, typically the broadside direction of signal propagation. In this wireless LAN communication: the extend range, improve signal quality, and increase data rates are important for the operation of the local network of devices with bandwidth allocated in

5.725–5.875GHz and central frequency in 5.8GHz [62], in specific standards or protocols within the Wi-Fi framework, such as 802.11a, 802.11ac, or 802.11ax (Wi-Fi 6) to allow communications down/uplinks point-to-point (P2P) between devices [63, 64].

In [65], a study delved into examining the influence of dielectric permittivity in different substrates on a MPA characterized by a circular resonator structure. The investigation also incorporated circular and elliptical slot structures (utilizing air gaps to enhance electric insulation) with the primary objective of broadening the antenna's bandwidth across frequencies. The findings highlighted conventional numerical gains ranging from 6.09 to 8 dB and showcased a notably wide bandwidth spanning between 35 and 38 GHz for permittivity values ranging from 2.1 to 6.1.

In [66], various dielectric materials that serve as substrates were analyzed for their application in Microstrip Patch Antennas operating at 28 GHz with millimeter wave functionalities. This study delved into the analysis of these materials, presenting a relative permittivity range of ε_r = 2.2–4.4. Throughout the investigation, the antenna dimensions remained constant. The findings revealed notable insights: the scattering matrix indicated superior impedance matching with the substrate of relative permittivity 2.2. Furthermore, the study scrutinized the directivity 7dB concerning the fundamental mode, focusing solely on parameters within the radiation pattern.

In [67], an MPA was designed and analyzed for applications operating at 28 and 39 GHz frequencies, catering to millimeter-wave functionalities. The study presented a comparative analysis of a typical MPA model using three distinct dielectric materials with relative permittivities: 2.2 (Rogers RT Duroid substrate), 4.6 (FR4), and 2.0 (Teflon). The results obtained showed gains of 6.7 dBi, 3.08 dBi, and 6.51 dBi, respectively. It's noteworthy that the physical dimensions of the proposed antenna remained constant throughout the study, focusing primarily on the fundamental mode of operation.

In the study by [68], a rectangular MPA is introduced, employing the technique of inserting a U notch into the slot to enhance bandwidth, in conjunction with a matching network. This approach utilizes materials with varying permittivity values to achieve desired performance characteristics. Remarkably, the authors maintain a high-quality factor of the MPA while observing that minimal reflections in the load configuration lead to maximal output power. Consequently, variations in dielectric constants result in distinct bandwidth shifts for the U-notch antenna. It is noteworthy that lower permittivity values of the substrate material are found to positively influence the gain of a broader band. However, it is pertinent to underscore that the investigations cited in this introductory section predominantly focus on bandwidth enhancement and neglect comprehensive analyses of radiation pattern parameters, higher-order mode operation, and the influence of dielectric alterations on radiation pattern performance. Addressing these aspects could provide deeper insight into the overall performance and potential optimizations of MPA systems.

In [69, pp. 52–68, Ch. 6], the analysis examines the influence of substrate material permittivity on the radiation patterns of higher-order TM_{30} at 60GHz and TM_{50} modes at a frequency of 100GHz, respectively. In your study, the analysis involved three different dielectric materials with relative permittivities (loss tangents): $\varepsilon_r = 3$ ($\tan\delta = 0.0011$), $\varepsilon_r = 6.7$ ($\tan\delta = 0.01$), and $\varepsilon_r = 10.2$ ($\tan\delta = 0.0022$), along with a theoretical material with $\varepsilon_r = 15$ ($\tan\delta = 0.002$). In the third mode under study [69, p. 57, Ch. 6], various materials exhibited a resonance frequency shift within the frequency domain, ranging from 60 to 60.5 GHz. Analysis of the radiation pattern revealed a significant reduction in sidelobe levels in the E-plane, particularly noticeable with higher permittivity values.

Additionally [69, p. 54, Ch. 6], in the TM_{30} mode, an increasing trend was observed in the Half-Power Beam-Width (HPBW) on the H-plane with higher permittivities. In the TM_{30} mode, there was an approximate average reduction in sidelobe level from 7.5 dB ($\varepsilon_r = 3$) to -15 dB ($\varepsilon_r = 10.7$) on the E-plane, considering non-normalized directivity [69, p. 56, Ch. 6].

For TM_{50} mode, frequencies ranged from 96 to 102 GHz, often overlapping with neighboring modes (undesired), leading to frequency displacement. In the radiation pattern (directivity), sidelobe levels decreased on the E-plane from 7.5 dB ($\varepsilon_r = 3$) to 5 dB ($\varepsilon_r = 10.7$) and lower than 0 dB ($\varepsilon_r = 15$) [69, p. 63, Ch. 6]. It's important to note that directivity analysis is not normalized, and these values are approximations.

The objective of this chapter is to achieve a reduction in sidelobe levels specifically in the TM_{30}-mode through permittivity analysis. The goal is to maintain a constant directivity that approximates the conventional directivity at the TM_{30}-mode. This reduction in patch length is crucial to maintain a constant wavelength, λ, contributing to the overall desired performance enhancement.

4.2 Interpreting the Resonant Cavity as a Densely Dielectric Box

We can to interpretate an MPA as a densely dielectric box, where it is full fill of permissive material bounded by two conductors plates (resonator patch and grounded surface) on microstrip technology. Thus, the distance between radiating slots (slots #1 and #3) varies with the increase in permittivity according to the relation:

$$d_{\mathrm{slot}} \propto \frac{3}{2\sqrt{\varepsilon_{\mathrm{reff}}}}, \tag{4.1}$$

where d_{slot} is the distance between the slots, and $\varepsilon_{\mathrm{reff}}$ is the effective permittivity. In this context, we highlight that lower permittivity values result in a greater distance between the radiating slots, which effectively increases the length of the antenna. This increase in effective length proportionally enlarges the electrical dimensions of the antenna, leading to the emergence of sidelobe levels. This phenomenon can be viewed as two dipole antennas separated by a distance of d_{slot}. Noticeably, higher permittivity values lead to a shorter distance between the slots, which consequently impacts the suppression of sidelobe levels. However, this maintains the observable mode of operation without modification.

Using Array Theory, we can understand the arrangement and combination of two beams (beam #1 and beam #2) resulting in a single contribution (in broadside), as shown in Fig. 21 (a, b, and c). This top view illustrates a pair of dipoles spaced by a distance d_{slot}, which is the same distance that the radiating slots are spaced in a dielectric box with effective permittivity $\varepsilon_{\mathrm{reff}}$. It's important to highlight that $d_{\mathrm{slot}} \approx L_{\mathrm{eff}}$ approximately. However, the distance d_{slot} is expressed in terms of the free-space wavelength (which does not change), while the effective length L_{eff} is expressed in terms of the guided wavelength (which may change because it depends on the effective permittivity, which varies in our analyzed concept).

In this sense, we can see that the distance d_{slot} between two dipole antennas decreases from $1.5\lambda_0$ to $0.5\lambda_0$. Using phasor representation, we observe that the intensity of the beam (as shown in Fig. 21(a)) at $0.75\lambda_0$ has diminished in intensity on the radiation pattern. Consequently, the SLL become less pronounced, as shown in Fig. 21(b). In the last case, we denote that the distance between dipoles is approximately $0.5\lambda_0$ (as shown in Fig. 21(c)). Note that the effective length remains the same for the third mode of operation, but the distance between the slots does not. This discussion is analyzed by effective dimensions; in other words, this analysis keeps the TM_{30} mode fixed at the same frequency of operation (proposed at 6 GHz). However, it diminishes the electrical dimensions by effective permittivity, reducing the sidelobe level as we will demonstrate. A disadvantage observed in this study is a slight drop in directivity from 12 dB to 9 dB. All these considerations are discussed throughout this chapter.

The behavior of the MPA front with respect to the increase in permittivity is depicted in Fig. 21. Initially, Fig. 21(a) illustrates the electrical field exhibiting three sinusoidal factors oscillating (as provided by the Resonance Cavity Analysis) in TM_{30} and appear three surface density current $\boldsymbol{J}_s$ at counter-phase setting. In this operating state (Fig. 21(a)), the sidelobe levels are higher in comparison to the main lobe (at the broadside direction, $\theta = 0^\circ$), and the effective dimensions is:

$$A_{\mathrm{eff}} = (L_{p1} + 2\Delta L) \times (W_{p1} + 2\Delta W), \tag{4.2}$$

they are also significantly high with low relative permittivity ε_{r1}; where leakage energy of radiating slot is calculated by (2.21)–(2.22) for spacial case of squared patch, this convenience is required $\Delta W = \Delta L$. And it is notable that effective $\varepsilon_{\mathrm{reff}}$ depends on relative permittivity, because the effective effect is the relationship of substrate (used dielectric material) and air, discussed and given by (2.16) and (2.17) already shown in Chapter 2.

Figure 21. At the top, the patch antenna in the xy-plane is shown with the respective $\boldsymbol{J}_\mathrm{s}$ current distributions associated with the TM_{03} operating mode. As the relative and effective permittivities increase the guided wavelengths are reduced as can be seen for a rectangular patch antenna. At the bottom of the illustration, the maximums and minimums in the zx-plane are shown, and grid lobes in the broadside direction ($\theta = 0°$), as well as the behavior against the increase in relative permittivity. (a) It is shown relative permittivity $\varepsilon_{r1} < \varepsilon_{r2} < \varepsilon_{r3}$, we can observe that there are higher levels sidelobes with directivity D_0 and tree factors in the density distribution of the current $\boldsymbol{J}_\mathrm{s}$ in the patch. (b) Main lobe with D_0 directivity is more predominant than the side lobes, theoretically the density distribution current in the center is more predominant for ($\varepsilon_{r2} > \varepsilon_{r1}$). (c) Side lobes are reduced by increase in relative permittivity and there is a density distribution factor current in the center ($\varepsilon_{r3} > \varepsilon_{r2} > \varepsilon_{r1}$).

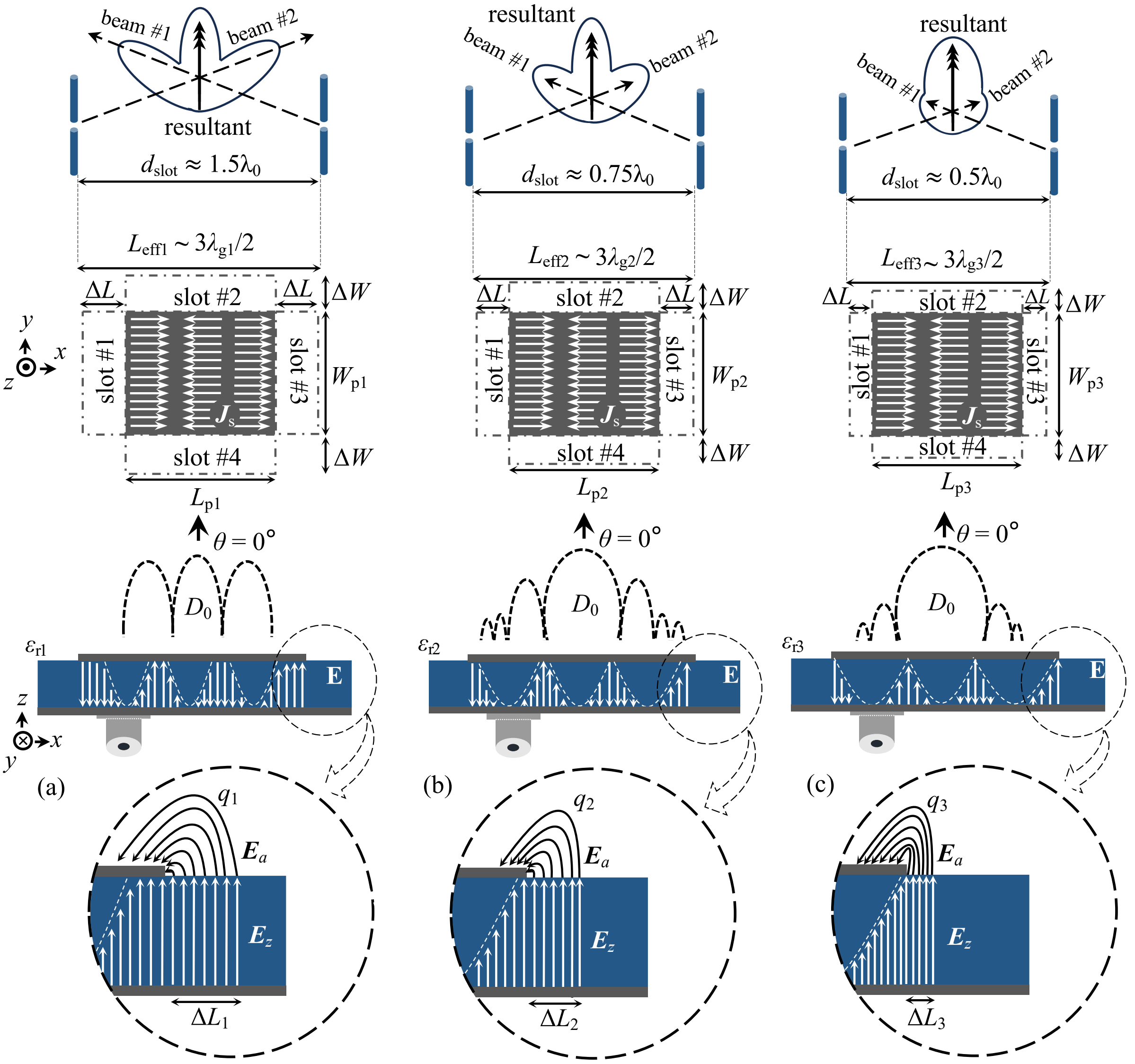

Source: author's own work (2024).

Moving to Fig. 21(b), where the permittivity is higher than in the first case ($\varepsilon_{r2} > \varepsilon_{r1}$), it is observed that the sidelobes are reduced and the main lobe expands. Noticeably, the effective area is reduced ($A_\mathrm{eff2} < A_\mathrm{eff1}$) due to the tendency of the directivity to decrease concurrently. Finally, in Fig. 21(c), the permittivity is significantly higher, leading to a reduction in Sidelobe Level to an insignificant value. This results in a more uniform electric field distribution in terms of the electric surface current density $\boldsymbol{J}_s$ in the operating mode. Consequently, the effective area is reduced and the directivity approaches a conventional value obtained previously, where $A_{\text{eff3}} < A_{\text{eff2}} < A_{\text{eff1}}$, when $\varepsilon_{r1} > \varepsilon_{r2} > \varepsilon_{r3}$. This outcome was anticipated and achieved through another modification in the patch antenna.

4.3 Interpreting the Effect Permittivity through Array Elements

In this chapter, we provide a comprehensive explanation of the effect of permittivity in our analysis. Indeed, in brief, we can interpret the proceeding analogical principle taken by an array grounded with two element patches (labeled as #1 and #2), in air with a constant dielectric of 1, separating the slots labeled as slot #1 and #2, as shown in Fig. 22(b). Following Fig. 22(a), the distance between radiating slots produces a higher sidelobe level for longer distances, as illustrated. We note that for $d_{\text{slot}} = 1.5\lambda_0$ (with larger distance), the sidelobe level becomes more pronounced with two significant sidelobes. This observation is supported by the theory of arrays [8]. Generally, in designs with large spacing between elements, there is a threshold allowed due to broadside radiation. With a decrease in d_{slot}, we note that the radiation pattern approximates a fundamental mode-like radiation pattern, without significant sidelobes.

Figure 22. Analysis for an array antenna with two elements (a) radiation pattern, (b) array structure with two patches spaced by distance between radiating slots, and (c) schematic equivalent MPA using our technique.

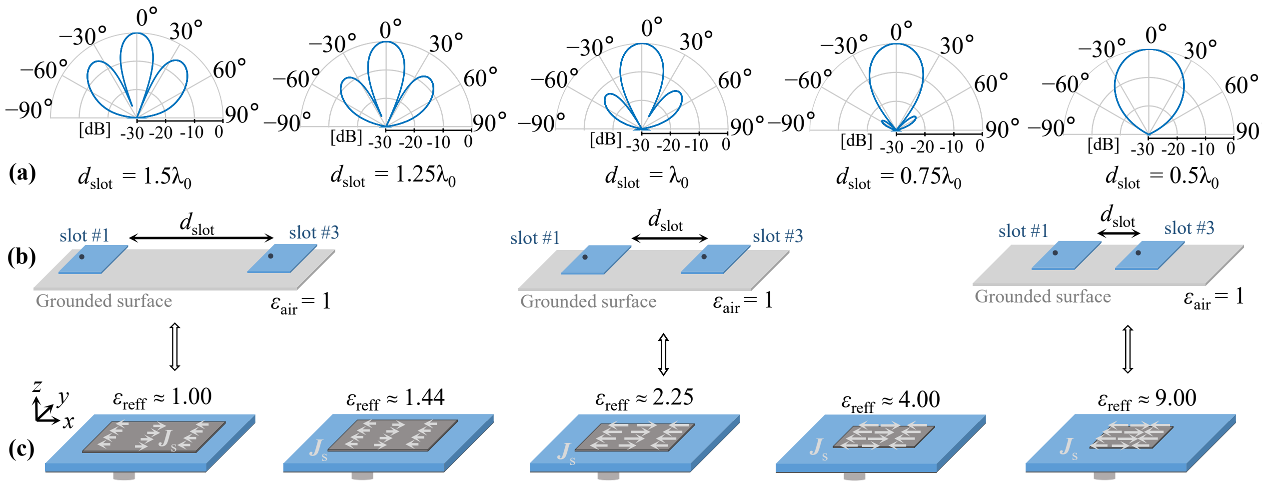

Source: author's own work (2024).

Through Eq. (4.1), we can see the relationship between the distance between radiating slots and the effective permittivity, which falls with the inverse of the square root. In the case of a dielectric constant of 1, it appears that at $1.5\lambda_0$, the spacing between array elements is considerable. With an approximate dielectric constant of 2.5, we can achieve $1.00\lambda_0$ spaced element slots, and consequently, the sidelobe level remains high (compare Fig. 22(a) with Fig. 23). When the permittivity increases to 4, the distance falls from 1.0 to $0.75\lambda_0$, and at this point, the sidelobes are lower but still present. With a higher permittivity of 9, we see a significant reduction in the sidelobe level, with a small distance between radiating slots (half-wavelength), demonstrating a good application for design decisions that involve compromises in radiation pattern performance.

Figure 23. Relationship of distance between radiating slots and effective permittivity on TM_{30}-mode configuration.

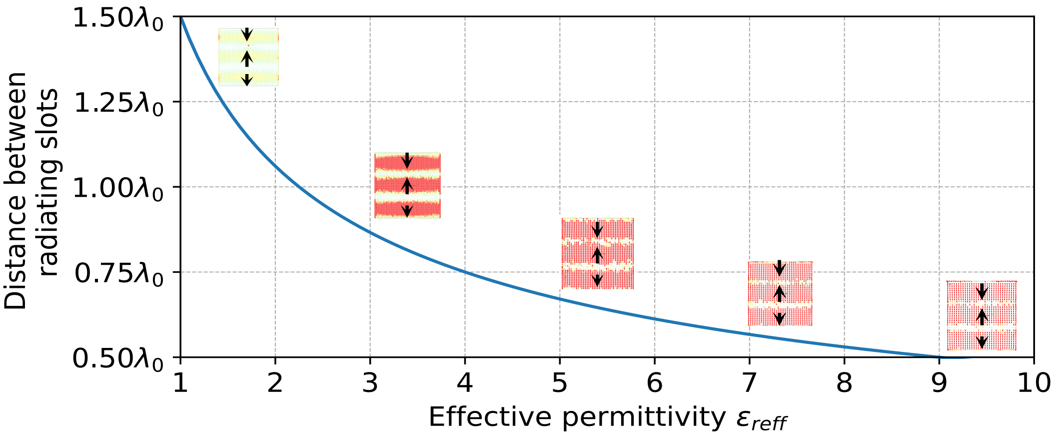

Source: author's own work (2024).

Note that the frequency is fixed (used here for 6GHz in TM_{30} mode, which is 2GHz in TM_{10} mode). If it were not fixed, the field configurations would be altered by the introduction of other neighboring modes, such as TM_{22} and others.

4.4 Impact of Permittivity on the Main Figures of Merit of the MPA

4.4.1 Surface Current Density, J_s

The surface current density atop a patch resonator arises from the interplay between the conductor's current density $\boldsymbol{J}_\mathrm{c}$, governed by *Ohm's Law*, and the current density within the dielectric $\boldsymbol{J}_\mathrm{d}$ conducted by *Ampère-Maxwell's Law*. This intricate phenomenon is precisely captured by Eq. (4.3), which elucidates the intricate interplay between these essential field components in antenna design [70, Ch. 10],[32, Ch. 1, p. 11],[71, Ch. 4, p. 142]:

$$\boldsymbol{J}_\mathrm{s} = \boldsymbol{J}_\mathrm{c} + \boldsymbol{J}_\mathrm{d} = \sigma \boldsymbol{E} + j\omega\varepsilon \boldsymbol{E}, \qquad (4.3)$$

we note that one significant contribution to the current density, particularly within dielectric materials, is the presence of complex permittivity denoted by $\varepsilon = \varepsilon' + j\varepsilon''$. In this context, we can reformulate this expression as $\varepsilon = \varepsilon_0\varepsilon_r(1 + j\tan\delta)$, given that the real part predominates over the imaginary part. The loss tangent $\tan\delta$ is typically quite small, often of the order of 10^{-2} to 10^{-4} for dielectrics used in majority substrates. By considering the Amperian dielectric contribution, which is associated with the electrical surface current density, we can verify that the permittivity effect increases linearly with the amplitude of the electric current on the substrate material. On the other hand, when we evaluate a good substrate with lowloss ($\tan\delta \approx 0$), we can express the complex permittivity predominantly through its real part, $\varepsilon' \gg \varepsilon''$, such that $\varepsilon \approx \varepsilon_0\varepsilon_\mathrm{r}$, only look for material properties. But, the system substrate-air should be considerable, such we can approximately $\varepsilon \approx \varepsilon_\mathrm{ereff}$, leading to the following consequence (on fixed resonance frequency ω_r):

$$\boldsymbol{J}_\mathrm{d} \approx j\omega_r\varepsilon_\mathrm{reff}\boldsymbol{E}. \tag{4.4}$$

Despite all considerations and conditions imposed to Eq. (4.4), we haven't got how to deny a impact significant of effective permittivity under electric current and we become to understand a linearly ascendant behavior governing on MPA.

4.4.2 Theoretical Radiation Pattern

Theoretically, to analyze the effects of permittivity on the radiation pattern on the main planes of radiating power, we modified Equation (2.30) to Equation (4.5), explaining $\beta = \frac{2\pi}{\lambda_0}\sqrt{\varepsilon_\mathrm{reff}}$ keep on λ_0 constant in order to verify the theoretical impact:

$$f(\theta,\phi,\varepsilon_\mathrm{reff}) = \frac{\sin\left(\frac{\frac{2\pi}{\lambda_0}\sqrt{\varepsilon_\mathrm{reff}}\,mW}{2}\sin\theta\sin\phi\right)}{\left(\frac{\frac{2\pi}{\lambda_0}\sqrt{\varepsilon_\mathrm{reff}}\,mW}{2}\sin\theta\sin\phi\right)}\cos\left(\frac{\frac{2\pi}{\lambda_0}\sqrt{\varepsilon_\mathrm{reff}}\,mL}{2}\sin\theta\cos\phi\right). \tag{4.5}$$

Using Eq. (4.5) modified wavelength on fundamental mode TM_{10}, it is $(\lambda_r)_{10}$, and additionally setted up $m = 3$ on third order analysis. We got to simplify the fractional terms and reorganize them, then arriving:

$$f(\theta,\phi,\varepsilon_\mathrm{reff}) = \frac{\sin\left(\frac{3\sqrt{\varepsilon_\mathrm{reff}}\,\pi W}{(\lambda_r)_{10}}\sin\theta\sin\phi\right)}{\left(\frac{3\sqrt{\varepsilon_\mathrm{reff}}\,\pi W}{(\lambda_r)_{10}}\sin\theta\sin\phi\right)}\cos\left(\frac{3\,\sqrt{\varepsilon_\mathrm{reff}}\pi L}{(\lambda_r)_{10}}\sin\theta\cos\phi\right), \tag{4.6}$$

with $L = W \approx 50$ mm, we plot graphic of Fig. 24(a) and Fig. 24(b) to express the magnitudes E_θ and E_ϕ on θ-elevation domain:

Figure 24. Theoretical radiation pattern for effect's permittivities on (a) E-plane and (b) H-plane keep on constant resonance frequency $(f_r)_{30} = 6$GHz (at $(\lambda_r)_{30} = 49.96$ mm).

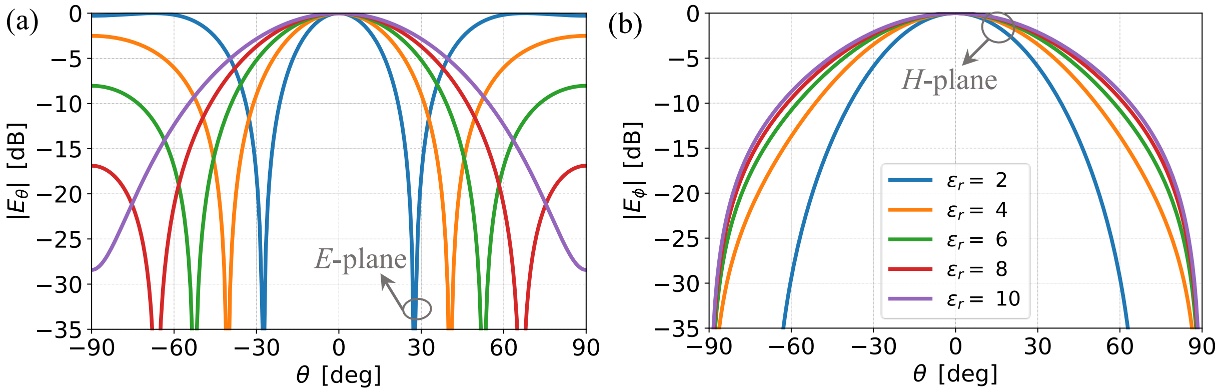

Source: author's own work (2024).

In Fig. 24(a), it is shown irradiation diagram with noteworthy that a reduction in sidelobe levels is clearly evident (theoretically) with variations in relative permittivity in the E-plane. We observe a decrease in SLL from 0 dB (at $\varepsilon_r = 2$, indicated by the blue curve), to lower than -5 dB (at $\varepsilon_r = 6$, indicated by the green curve), -15 dB (at $\varepsilon_r = 8$, indicated by the red curve), and finally to -25 dB (at $\varepsilon_r = 10$, indicated by the violet curve). In Fig. 24(b), we can observe a noticeable enlargement of the main lobe (theoretically) in response to variations in relative permittivity in the H-plane. We observe this enlargement, indicated by the blue curve, showing an increase in half-power beamwidth from 60 degrees (at $\varepsilon_r = 2$) to 90 degrees (at $\varepsilon_r = 8$ and $\varepsilon_r = 10$, shown by the red and violet curves, respectively).

It is happens because changes in relative permittivity have the capability to modify the positions between nulls on the radiation pattern, particularly in the domain of elevation angular plane. By adjusting the relative permittivity, the nulls within the pattern are spaced apart from each other. This variation in permittivity displaces two nulls (given by distancing them) increasing their distance along the wavenumber domain. Consequently, this effect results in the emergence of single maxima, effectively leading to a "reduction" in the sidelobe level on the E-plane.

4.4.3 Energy Leakage Length and Fringing Phenomenal

Finally, we can address the issue of energy leakage in the fringing field due to extension length. With the mathematical models provided by equations (2.22) and (2.27), we can illustrate the normalized ratio of the extension length to height, $\Delta L/h$, and the fringing factor q, respectively, in terms of variations in permittivity, as depicted in Fig. 25(a). The theoretical values are plotted while keeping L_p fixed in the analysis. Additionally, Fig. 25(b) shows the simulated values for extension length and fringing factor (in blue and red colors with dashed lines marked by circles, respectively) while maintaining the resonance frequency constant. In this analysis, we have set the standard values for L_p and W_p as 60 mm, and h as 1.575 mm.

Figure 25. Normalized ratio of effective extended length and normalized fringing factor in (a) physical patch length and (b) resonance frequency angular fixed.

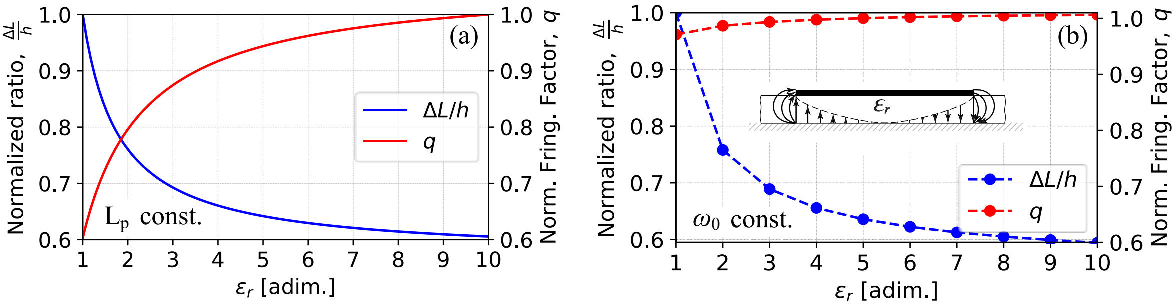

Source: author's own work (2024).

It is anticipated that energy leakage (extended length) will decrease with an increase in permittivity due to the compression of fringing fields, which narrow as a result of the packing of field lines at the radiating edge. This phenomenon holds true for both cases, with L_p and ω_0 fixed, as demonstrated in the introductory section by Fig. 21(a)–(c). Moreover, the fringing factor undergoes significant modification owing to central frequency resonance, as evident from the comparison in Fig. 25(a) and 25(b). It is observed that q exhibits significant variation (with L_p fixed) due to the variation in resonance frequency with respect to other parameters. It is important to recall that the relationships in Equations 2.26 and 2.27 were previously presented in section 2.4. When the central resonance frequency ω_0 is held constant, it is noted that the fringing factor experiences minimal modification, maintaining an approximation close to 1. This is in contrast to the scenario depicted in Fig. 25(a), where, starting from smaller values ($\varepsilon_r = 1$), the approximation begins around 0.6 and gradually increases (due to increasing permittivity) until it ultimately converges to 1.

4.4.4 Propagation Wave on Media

In Chapter 2, we observe that the radiation density spatially distributes electromagnetic energy, along with the propagation of plane front waves into the far-field region. It is evident that these waves may undergo alterations due to the material properties of the antenna being utilized. In the theory of radiation energy propagation, a uniform plane front wave in an unbounded lossy medium exhibits the characteristic of a *traveling wave* (which to present constant phase plane). The electric and magnetic components must satisfy the propagation condition, expressed as $E_z \sim E_0^{\mp} e^{\pm\gamma z}$ for positive and negative propagation solutions along the z-direction. Here, the complex propagation constant $\gamma = \alpha + j\beta$

comprises the attenuation constant α and the phase constant β [71, Ch. 4, p. 138]. In this analysis, we will examine the phase constant and its impact to variations in permittivity. And then we calculate the phase constant (in rad/m) within Eq. (4.7) [71, Ch. 4, p. 139]:

$$\beta = \sqrt{\frac{\omega^2 \mu \varepsilon}{2}(\sqrt{1+\tan^2\delta}+1)}. \tag{4.7}$$

In good dielectrics, on imposition of $(\sigma/\omega\varepsilon)^2 \ll 1$, we can approximate β to [71, Ch. 4, p. 142]:

$$\beta \approx \omega\sqrt{\mu\epsilon}. \tag{4.8}$$

We highlight that approximation has neglected the losses on dielectric substrate (considering $\tan\delta \approx 0$). Only within permittivity predominance and in resonance effect we got it $\omega_0 = c_0 k_0 = \frac{k_0}{\sqrt{\mu_0\varepsilon_0}}$, it's we come across [32, Ch. 3, p. 147]:

$$\beta = k_0\sqrt{\varepsilon_{\text{reff}}}, \tag{4.9}$$

and consequently the phase velocity v_p in meter per second can be defined by [32, Ch. 3, p. 147]:

$$v_p = \frac{c_0}{\sqrt{\varepsilon_{\text{reff}}}}. \tag{4.10}$$

We emphasize that while the microstrip line exhibits a good characteristics under TEM waves, owing to combinations of TM-TE hybrid modes. However, the microstrip antenna patch operates as a cavity resonator primarily propagating TM waves in the near-field region, and so, in the far-field, its behavior conforms to uniform plane wave propagation with constant phase [32, Ch. 4, p. 147]. These distinctions aid in understanding the delineation between propagation regions and cutoff frequency bands on the k-β diagram (or Brillouin diagram) [32, Ch. 8, p. 385]. Furthermore, they facilitate an explanation of how variations in permittivity affect the irradiation phenomenon. In Fig. 26(a), a Brillouin diagram illustrates the relationship between the electric angles kL and βL, which are associated with the wavenumber k and the phase constant β, respectively. This diagram showcases how variations in permittivity influence these parameters. In the Brillouin diagram shown, the y-axis typically represents the wavenumber k, which is a measure of spatial frequency. The x-axis represents the phase constant β, which describes the phase change undergone by a wave as it propagates through a medium [72, Ch. 5, p. 239].

Figure 26. Effect's permittivity on (a) Brillouin diagram and (b) phase constant, phase velocity and $k\beta$-slope variation.

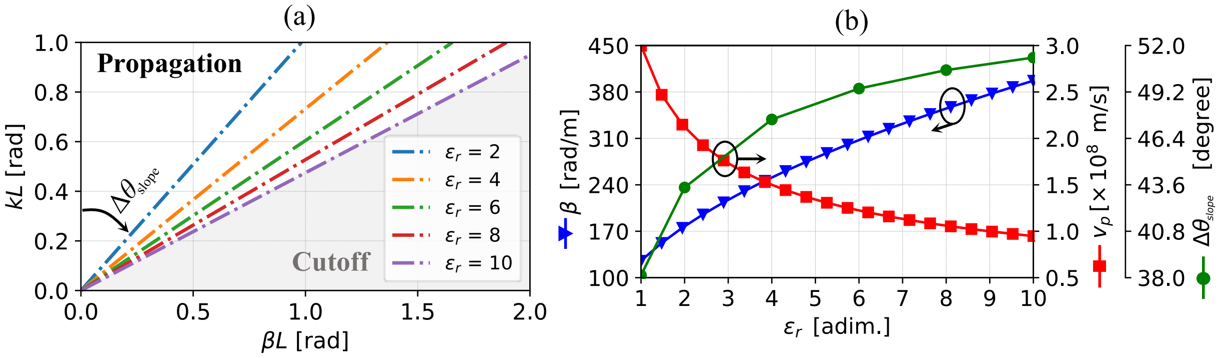

Source: author's own work (2024).

We focus on the existence of two distinct regions on the k-β-diagram: the *propagation region*, where signals can be transmitted in all directions owing to the dispersion of the $\boldsymbol{k}$-vector, and the *cutoff region*, depicted in clear gray, where the medium does not radiate electromagnetic signals within certain frequency spatial bands. The k- and β-curves are dispersion characteristics and they're useful to analyze dispersion relations on guided-waves systems [72, Ch. 5, p. 399] (as it is the case on here). Regarding the linear relationship, as expected from Eq. (4.9), we observe a slight steepening of the line due to an increase in the $k\beta$-slope variation $\Delta\theta_{\text{slope}}$, given by the steepness of the straight line k-β (as indicated in the insert of the graphic in Fig. 26(a)). This can be expressed as:

$$\Delta\theta_{\text{slope}} = \tan^{-1}\left(\frac{k}{\beta}\right) = \tan^{-1}\left(\frac{1}{\sqrt{\varepsilon_{\text{reff}}}}\right), \tag{4.11}$$

with an increasing $k\beta$-slope variation, the propagation region becomes more predominant, and consequently, the cutoff region becomes smaller, allowing certain frequency bands to be radiated by the device. It's worth noting that an increase in the permittivity parameter enables an increase in the spatial frequency k, in other hand, new spatial frequencies components starting to be used by electromagnetic device allowing and facilitating signal transmission and new spectral components spatially on medium.

In Fig. 26(b), the theoretical model for the phase constant, phase velocity, and the variation of the $k\beta$-slope computed by Equations (4.9), (4.10), and (4.11) is presented. Note that the increase in the phase constant β (shown in the blue dashed line with triangular markers) and the angular slope variation $\Delta\theta_{\text{slope}}$ (in green dashed line with circular marker) correspond to the increasing relative permittivity. In contrast to that, phase velocity (in red dashed line with squared marker at Fig. 26(b)) come more smaller affecting plane constant of TEM wave on increasing relative permittivity.

As discussed previously, the angular slope $\Delta\theta_{\text{slope}}$ aperture allows the analysis of new components of spatial frequency propagating in space. In our analysis, we set up the k_r-number wave operating, keeping the wavelength λ_0 constant for the fixed resonance frequency f_r. If we increase the wavenumber k of the dispersion amplitude $\boldsymbol{k}$-vector in a traveling front wave, essentially increasing the spatial frequency of the wave. The k-wavenumber measures how many waves (or cycles) occur per unit distance in the space propagated [73]. Its increase leads to a more densely packed wave in space, allowing the electromagnetic wave to operate in higher frequency ranges such as THz bands, infrared bands, and so on [74]. Naturally, this increase in frequency results in higher energy for the electromagnetic wave, as photons oscillating in a wave-like pattern experience alterations in the wavelength spectrum [74]. This alteration leads to shorter wavelengths, indicating that the wave oscillates more rapidly within a given distance. In practical terms, increasing the wavenumber of the dispersion amplitude vector $\boldsymbol{k}$ means the wavefronts become closer together spatially, resulting in higher spatial frequency and potentially shorter periods between wave peaks.

Concomitantly, increasing the phase constant β of a traveling front wave implies a more rapid phase change as the wave propagates through a medium [71, Ch. 4, p. 133]. This behavior is illustrated more clearly in Fig. 26(b), where the increase in relative permittivity forces the phase constant to increase, potentially altering the phase plane in the propagation region. Specifically, if the phase constant increases, it indicates that the phase of the wave changes more rapidly with distance traveled, resulting in a faster phase shift as the wave moves forward.

Furthermore, in Fig. 26(b), the increase in permittivity of the material forces the phase velocity of a traveling front wave to decrease. This change doesn't necessarily imply a change in the speed of the wave itself, but rather how quickly a specific phase of the wave propagates through the medium [71, Ch. 4.p. 136].

4.4.5 Effect of Increasing Density Permissiveness on Height Variation

As we work with materials of higher permissive density, the effective height h_{eff} becomes roughly proportional to the inverse of the square root of the relative permittivity. Consequently, an increase in the dielectric constant can reduce the effective height of the antenna. For relatively large physical heights, above a few millimeters, along with the predominant permissive effect, this can result in the emergence of surface modes (these modes can account for surface waves) [29, 28, 25].

This occurs because there is a decrease in the cutoff frequency of these modes — cutoff frequencies in the range of a few hundred gigahertz can decrease, influencing the electromagnetic coupling of transverse electric modes TE_{mn}, since the microstrip structure is quasi-TEM. It is important to highlight that, to inhibit these modes, more sophisticated techniques are required for their filtering (such as artificial materials [75] that can excite or inhibit them, feeding method, etc.). This work does not consider this effect; it only evaluates the technique for reducing side lobe levels.

4.5 Numerical Analysis of Radiation Pattern

In simulation process, we denoted that Fig. 27(a), the radiation pattern is displayed for a range of permittivity $\varepsilon_{\mathrm{r}} = 2$ to 10 at resonance frequency $(f_{30})_r = 5.75$ GHz, showcasing the directivity in the E-plane for TM_{30}. It is notable that there is a noticeable reduction in total sidelobe levels, reaching -20.2 dB as the permittivity increases from 2 to 10.

Another parameter of significance is the HPBW, which increases (26° to 57°) due to the enlargement of the main lobe at the θ-elevation angle. Furthermore, in Fig. 27(b), a slight reduction in aperture efficiencies is observed, along with an enlargement of the main lobe in 6.15dB the E-plane for TM_{10} front to $\uparrow 78.3\%\varepsilon_{\mathrm{reff}}$ at $(f_{10})_r = 1.97$ GHz. In the H-plane for the TM_{30}-mode, where this effect is most prominent, there is a slight increase observed, causing the main lobe to become broader compared to other cases. This tendency aligns with the increase in absolute permittivity, as depicted in Fig. 27(c).

Figure 27. Radiation pattern for normalized directivity for (a) E-plane in TM_{30}, (b) E-plane in TM_{10}, (c) H-plane in TM_{10} and TM_{30}, (d) the directivity and radiation efficiency in band frequency in TM_{30}-neighborhood.

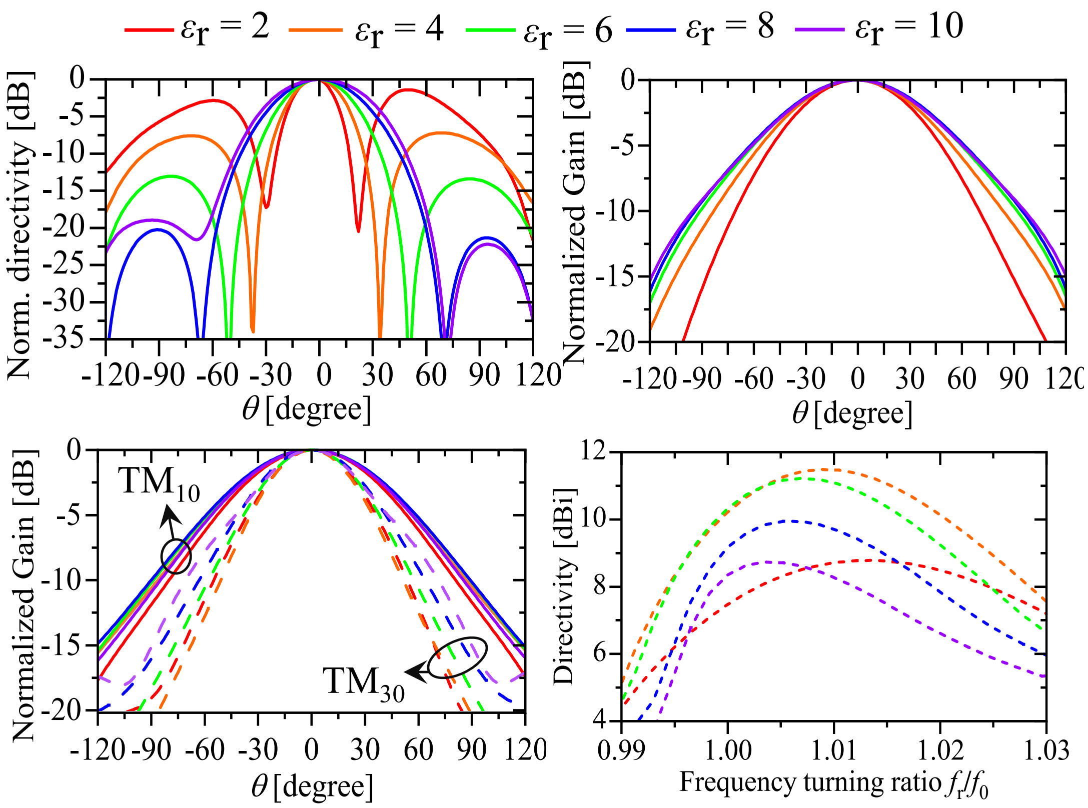

Source: author's own work (2024).

Additionally, note that the theoretically calculated effective length decreases $(\downarrow L_{\mathrm{eff}})$ as observed in the analysis findings. In Fig. 27(d), the directivity is presented across the frequency band, specifically concerning the frequency turning ratio f_r/f_0, normalized with $f_0 = 5.75$ GHz. The bandwidth (indicated by the transparent orange color BW) found ranged from 5.75 to 5.9 GHz. In particular, G_0 remains above 10 dBi for relative permittivity values ranging from 4 to 6 (indicated by orange and green colors).

Already, Fig. 28 illustrates the progression with increasing permittivity range, providing detailed radiation patterns represented in directivity format for both the E-plane (blue color, continuous line) and H-plane (red color, dashed line). The numerical values of permittivity range from $\varepsilon_r = 0.1$ (ideally) to $\varepsilon_r = 10$.

Observations indicate that for smaller ε_r, the sidelobe levels are higher (above $SLL = -6$ dB) as seen in the observation analysis (Fig. 28(a)–(d)). Additionally, it is evident that the directivity is above 12 dBi in these cases. Conversely, in Fig. 28(e)–(h), the sidelobe levels decay to approximately $SLL = -12$ dB, and the directivity drops by an average of 1 dB, stabilizing at 11.5–11.3 dBi. Subsequently, in Fig. 28(i)–(l), the sidelobe levels further reduce below -12 dB, and the directivity decreases by approximately 2 dB, stabilizing at 10.8–9 dBi.

Figure 28. Ideal behavior with radiation pattern (in directivity) for E-plane (at blue continuous color) and H-plane (at red dashed color) in front of varied relative permittivity.

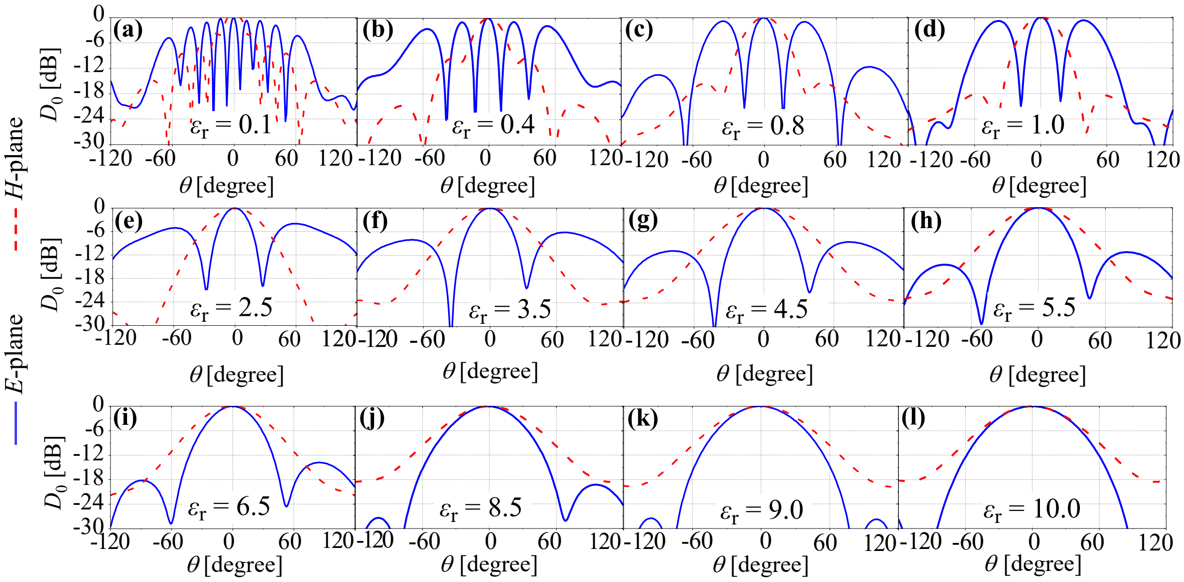

Source: author's own work (2024).

In Jupyter Notebook, within Python environments, the Cubic Spline Interpolator was utilized with $N = 1000$. We compared the variation of SLL in relative permittivity, including both the total simulated directivity (in dB-scale) and radiation efficiencies (the latter in linear scale), along with the physical patch length (which varied) and effective area. These observations are depicted in Fig. 28, illustrating the interpolated curves (continuous line) and simulation points (implemented data).

The field distribution of surface current density $\boldsymbol{J}_s$ reveals two peaks in phase (indicated by red arrows) and one peak in counter-phase (also marked by a red arrow). Additionally, at a permittivity value of 1 and 3, two minima are observed (indicated by green arrows), seemingly lacking a specific direction. These correspond to the transitional region of surface current formation, typical of the field distribution of the TM_{30} mode, as illustrated in Fig. 29. At a permittivity value of 5, we observe a notable intensification of all maxima (highlighted in red), while the transitional region indicated by minima peaks (in green) becomes less pronounced. Furthermore, in the overall organization of the field distribution, the combined contributions of smaller field components result in a stronger far-field radiation pattern, with the main lobe becoming predominant. Finally, at higher permittivity values such as 7 and 9, as observed in Fig. 29, the transitional region indicated by minima peaks (in green) ceases to exist. Furthermore, it's evident that the central maximum is suppressed at $\varepsilon_r = 9$, with two more intense maxima (highlighted in red) emerging. This tendency indicates a recombination of the field's contribution components into a **uniformity of the phase** [76], **amplitude** [76, 77], and **polarization state** [78], conditions favorable for **maximizing directivity**.

In Fig. 29, all plots are scaled uniformly along each axis; additionally, noteworthy is the color scheme employed, with hot colors (such as yellow, orange, and red) denoting maximum values, while cold colors indicate minima, facilitating a comparative understanding of magnitude levels. These plots serve as illustrations, providing insights into the dynamic behavior of the surface, radiation patterns, and electric field interactions within dielectric materials as relative permittivity undergoes significant increases.

Notably, in Fig. 29(a)–(e), for a permittivity value of 1–9, the top view depicts the distribution field of surface current density on the xy-plane. The bottom view showcases the radiation pattern directivity in the E-plane ($\phi = 0°$ or alternatively, the fixed xz-plane), with variations observed along the elevation direction θ. Additionally, the bottom view offers an isometric representation of the surface current density in three-dimensional space.

Furthermore, the density of the distribution field (of surface current and electric) increases proportionally from smaller to larger values of relative permittivity, reflecting the influence of the three oscillating factors of the TM_{30}-mode. This is evident in the identification of three distinct lobes at mean levels, characterized by significant maxima (highlighted in intense orange), particularly noticeable when compared to the main lobe at $\varepsilon_r = 1$. The observation reveals a slight intensity in the magnitude of surface density, depicted in yellow. Furthermore, it is evident that the electric component orthogonal to the surface of the resonator patch (conductor), situated within the xz-plane, exhibits three nulls, indicative of its third-mode operation, as depicted in Fig. 29(a). Notably, the density of vector field (relative to $\boldsymbol{E}$) is more pronounced in cases of smaller permittivities, with maxima observed at the extremities of the resonator and minima illustrated in a clean blue hue, as depicted in Fig. 29(f).

Figure 29. Simulated distribution of surface current density $\boldsymbol{J}_\mathrm{s}$ across the xy-plane, radiation pattern analysis, and characterization of the simulated electric field $\boldsymbol{E}$ (xz-plane).

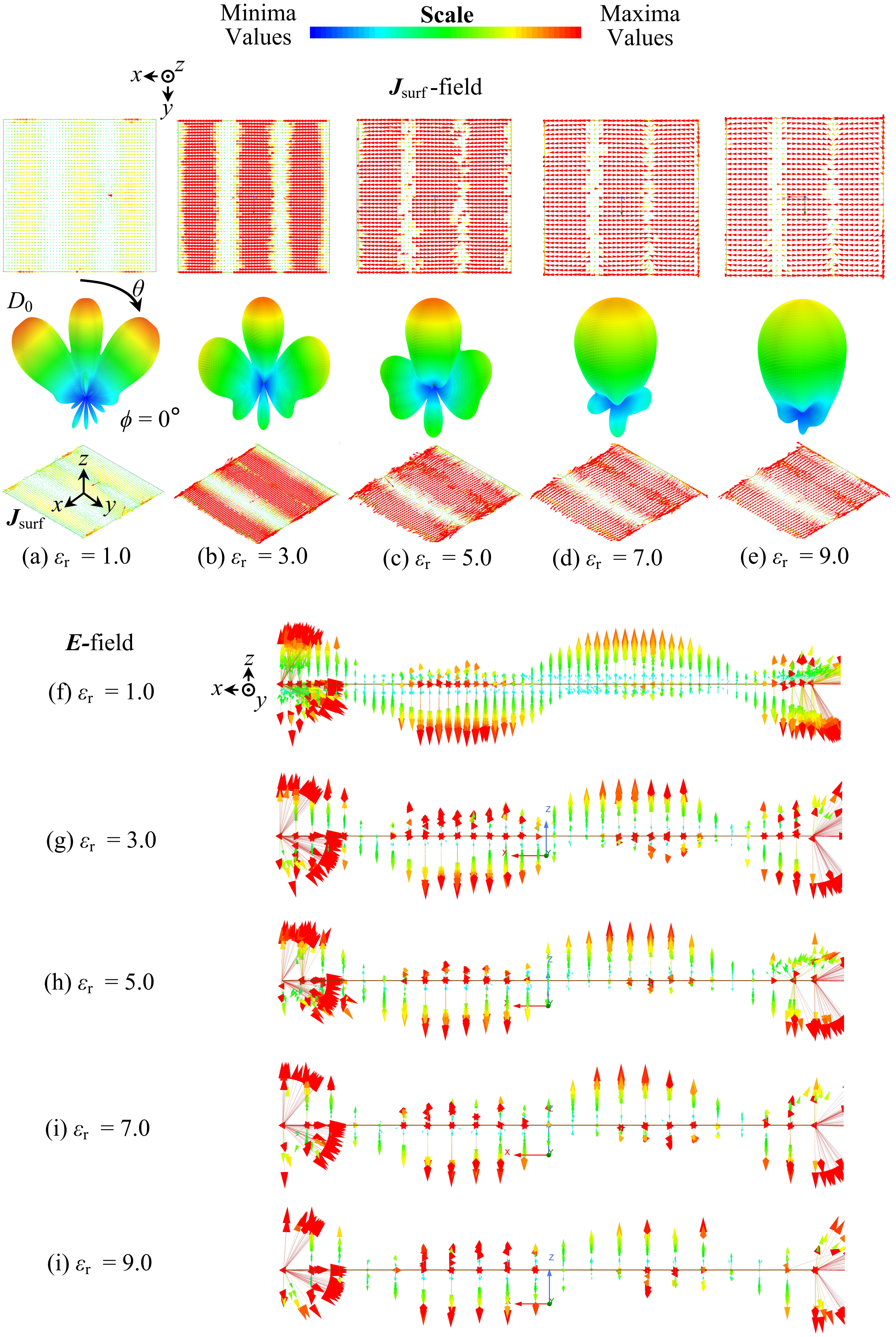

(a) $\varepsilon_\mathrm{r} = 1.0$ (b) $\varepsilon_\mathrm{r} = 3.0$ (c) $\varepsilon_\mathrm{r} = 5.0$ (d) $\varepsilon_\mathrm{r} = 7.0$ (e) $\varepsilon_\mathrm{r} = 9.0$

(f) $\varepsilon_\mathrm{r} = 1.0$

(g) $\varepsilon_\mathrm{r} = 3.0$

(h) $\varepsilon_\mathrm{r} = 5.0$

(i) $\varepsilon_\mathrm{r} = 7.0$

(i) $\varepsilon_\mathrm{r} = 9.0$

Source: author's own work (2024).

Thereby, the intensity of $\boldsymbol{J}_{\mathrm{s}}$ becomes significantly accentuated at $\varepsilon_r = 3$, causing practically the entire resonator patch area to dominate in red color. Another noteworthy observation is the presence of sidelobe levels, as depicted in Fig. 29(b), where the maximum values are highlighted in yellow on the radiation pattern. Although these values are smaller compared to those of the radiation pattern at $\varepsilon_r = 1$, they remain significant.

In Fig. 29(b), the surface current is depicted in an isometric view, emphasizing the presence of counter-phase components that add up, resulting in the cancellation of certain field components in the far region. At $\varepsilon_r = 3$, the electric field $\boldsymbol{E}$ demonstrates more spaced components (Fig. 29(g)), indicating that the substrate impedes the penetration of the electric field. This phenomenon is well-documented in the literature [79, Ch. 4]. Another factor that helps explain this phenomenon is the penetration of the electric field, which is captured by the electric displacement vector (assuming a linear dielectric medium and isotropic material) [79, Ch. 4],[32, Ch. 1, p. 12]:

$$\boldsymbol{D} = \varepsilon \boldsymbol{E}. \tag{4.12}$$

The electric displacement vector, as computed by Equation (4.12), exhibits a notable increase concomitant with the rise in permittivity. Specifically, the displacement vector demonstrates a proportional dependence on both the electric field and the effective permittivity, thereby amplifying its magnitude with higher permittivity values $\uparrow \varepsilon$. Such observations underscore the intricate interplay between material properties and electromagnetic phenomena, shedding light on the nuanced dynamics governing electric fields in varying dielectric mediums.

In Fig. 29(c) and its combined analysis with Fig. 29(g), a notable intensification in surface current density is observed compared to previous cases. It is noteworthy that the nulls within the $\boldsymbol{J}_{\mathrm{s}}$ field plot appear narrower, indicative of a more concentrated current distribution. Moreover, the radiation pattern corresponding to a permittivity value of $\varepsilon = 5$ exhibits a decrease in magnitude, yet the pattern's significance is heightened, as depicted by the discernible green color-map. Additionally, the vectorial field of surface current presents counter-phased components that are closer in proximity to one another – probably cancelling them in far-field region. Concurrently, a pronounced spacing persists between the electric vectorial components, surpassing that observed in cases with a relative permittivity of three. Notably, the nulls traverse towards the extremities of the patch resonator, as illustrated in Fig. 29(g).

Already in Fig. 29(d) and its combined analysis with Fig. 29(i), a notable escalation in surface current density is evident compared to previous cases with relative permittivities of 3 and 5. This increase in intensity is corroborated by the virtual absence of nulls within the plot, indicating a concentrated distribution of current. Furthermore, the radiation pattern corresponding to a permittivity value of $\varepsilon = 7$ exhibits a pronounced decrease in magnitude, particularly highlighted by the cyan-blue color-map. Upon examining the surface current vector field in an isometric view, it becomes apparent that counter-phased components are closer in proximity, resulting in a cancellation of themselves in the far-field. Concurrently, a significant spacing between electric vectorial components is observed, accentuating the expansion of the electric displacement field in comparison to cases with lower relative permittivities. Notably, as previously observed, the nulls in the electric field (as depicted in Fig. 29(i)) migrate towards the extremities, while a complete resonating cycle manifests upon the metallic conductor (patch).

Finally, in the case where the relative permittivity is $\varepsilon_r = 9$, as depicted in Fig. 29(e) and Fig. 29(j), a remarkable convergence of surface current densities towards uniformity is observed, facilitating the cancellation of most field components in the far region. This phenomenon leads to a nearly complete reduction in sidelobe levels within the radiation pattern, as evidenced by the conspicuous decrease in SLL. Additionally, a slight decrease in the maxima, depicted in yellow on the color-map, was anticipated during the simulation process and subsequently validated by the results presented in Fig. 28(b). Our hypothesis is further corroborated by the findings in Fig. 29(e), where the near-complete cancellation of field components in the far-field is vividly illustrated in the xy-plane, where counter-phased arrows converge due to the proximity-induced increase in permittivity magnitude.

Moreover, the vectorial components associated with oscillating cycles exhibit a diminished intensity compared to previous scenarios analyzed, suggesting that a single maximum becomes dominant in the far-field, akin to a fundamental mode behavior. Furthermore, it is notable, as depicted in Fig. 29(j), that nulls near the extremities are less intense, potentially propagating away from the resonator patch and likely into the substrate and beyond the outer surface of the metallic conductor.

We delve into how variations in permittivity influence far-field radiation pattern G_0 across the $\phi \times \theta$ domain using contour maps, where warm hues signify maxima and cool hues indicate minima of total directivity. These maps, depicting directivity as a function of dielectric constant ε_r, offer crucial insights into electromagnetic behavior, showcasing how material properties shape radiation patterns. Figure 30 displays contour maps for five dielectric constants: (a) $\varepsilon_r = 1$, (b) $\varepsilon_r = 3$, (c) $\varepsilon_r = 5$, (d) $\varepsilon_r = 7$, and (e) $\varepsilon_r = 9$, providing a comprehensive understanding of directivity distribution's evolution with varying dielectric constants, crucial for optimizing antenna performance. In particular note in Fig. 30(a) is the pronounced presence of sidelobes (within $30° \leq \theta \leq 60°$ and $-60° \leq \theta \leq -30°$), exhibiting heightened intensity (depicted in red) alongside the mainlobe, particularly noticeable in the E-plane at broadside ($\theta = 0°$).

Figure 30. Contour maps show directivity variation across dielectric constants, it depict directivity for: (a) $\varepsilon_r = 1$, (b) $\varepsilon_r = 3$, (c) $\varepsilon_r = 5$, (d) $\varepsilon_r = 7$, and (e) $\varepsilon_r = 9$.

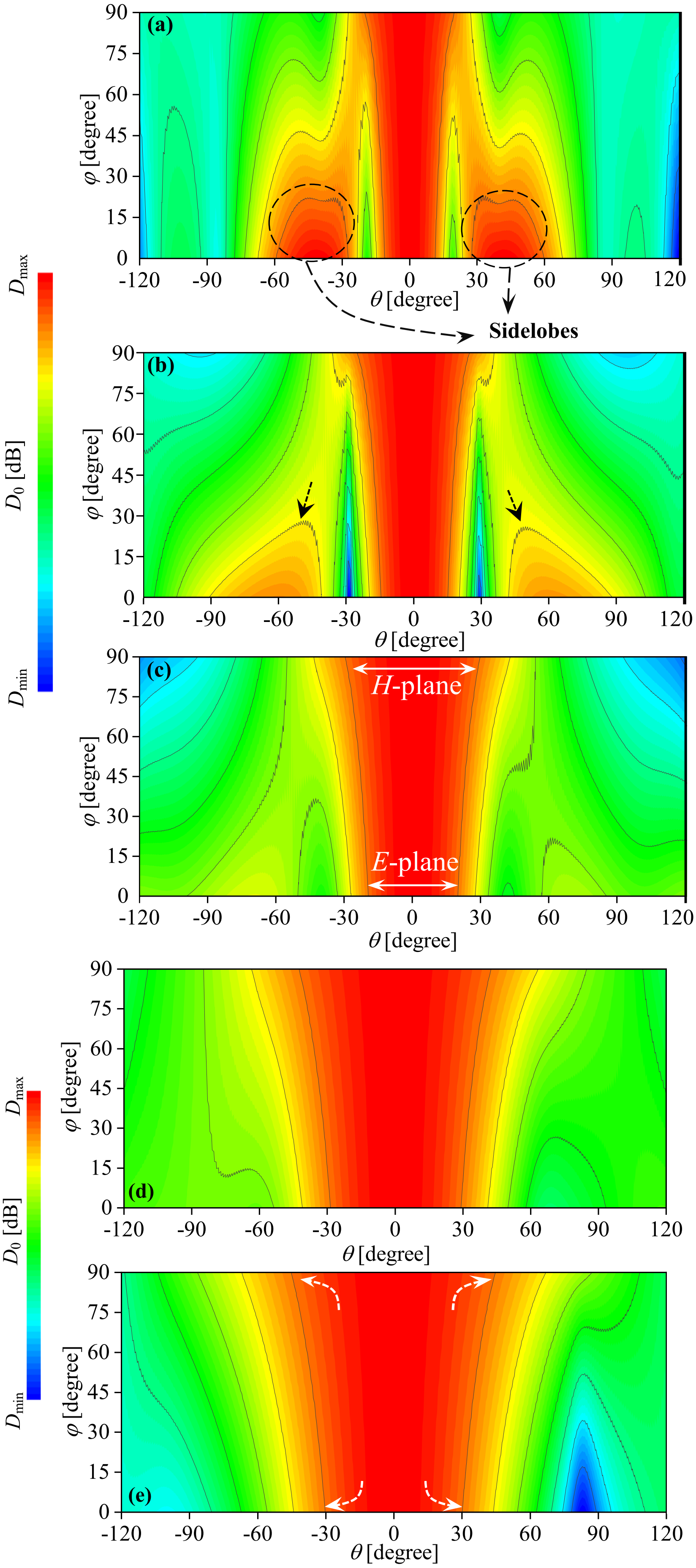

Source: author's own work (2024).

Discussion also highlights the decrease in sidelobe magnitude during the transition within $30° \leq \phi \leq 45°$ at ϕ-direction, affecting sidelobe intensity in the H-plane. This phenomenon characterizes a third mode operation, already evident at $\phi = 90°$ (Fig. 30(a)). In our analysis, a subtle transition in sidelobe levels, indicated by a shift from orange to yellow hues on the contour map, draws attention. We emphasize the partial radiation of electromagnetic energy into space, depicted in clear green, signifying signal dispersion due to neighboring sidelobes (albeit with lower intensity), potentially affecting target precision.

Furthermore, in Fig. 30(b), the effective suppression of more pronounced secondary lobes with increasing dielectric constant from 1 to 3 is evident. Notably, arrows highlight the significant reduction, even in the orange color range, around $\theta = \pm 60°$. Strong nulls emerge at $\theta = \pm 30°$ in the E-plane ($\phi = 0°$), while in the H-plane, there's a slight enlargement of the mainlobe, particularly perceptible at $\phi = 90°$ (Fig. 30(b)).

Henceforth, Fig. 30(c) depicts an intermediate scenario with a permittivity value of $\varepsilon_r = 5$, reinforcing our earlier discussions. We emphasize the dispersion of electromagnetic energy into undesired directions, as evidenced by clear green hues. Conversely, we draw attention to the widening of the mainlobe, accompanied by the presence of sidelobe levels, illustrating how the increase in dielectric constant correlates with the expansion of the half-power beam-width in both the E- and H-planes (as indicated by double arrows), as previously discussed.

The observations (behavior) made in Fig. 30(c) persist in both Fig. 30(d) and Fig. 30(e), on latter cases on dielectric constant at $\varepsilon_r = 7$ and 9, characterized by a significant increase in the global beamwidth associated with the mainlobe in both the E- and H-planes. We note that a portion of the electromagnetic energy, carried by wave-front propagation, diverges from the broadside direction, yet the majority remains focused at $\theta = 0°$. Furthermore, we highlight a slight decrease in the total directivity, from approximately 12dBi to 9.7dBi, as illustrated in Fig. 28(b).

These observations align with the coherent and concise analysis presented in previous sections, particularly in Fig. 27(a) and 28(c) combined within Fig. 29(a)–(e), it was which demonstrated the effect on radiation performance, underscoring the enlargement of the mainlobe (indicated by white arrows on Fig. 30(e)) upper than $\theta = \pm 30°$ on latter scenarios. Additionally, the significantly suppression of secondary lobes practically nonexistent on two last cases analyzed.

The representation in contour mapping, as depicted in Figure 30, serves as a conduit for gaining insight into the topics previously introduced and elaborated upon in this section. Through this analysis, we endeavor to elucidate the dynamics of field distribution and the nuanced interplay between amplitude and phase uniformity across varying permittivity levels in dielectric materials. Figs. 30(a)–(e) provide a visual narrative, offering answers and an overarching perspective on these intricate dynamics.

4.6 Physical and Electric Compact Sizing

4.6.1 Normalization of Effective Size Parameters

Afterward of an extensive discussion on the influence of permittivity on the radiation pattern, it is imperative to delve into the impact of permittivity on the electrical dimensions, particularly within the context of a fixed resonance frequency. Moreover, it is crucial to comprehend the underlying reasons for the observed decrease in physical length. To compute the effective length L_{eff}, we express Equation (4.13) in terms of normalized guided wavelength λ, delineating its contribution as a balance between the physical length L_p and the additional length induced by leakage energy, denoted as ΔL:

$$L_{\text{eff}}\,[\lambda] = \left[\frac{1}{\lambda_0}\Big(L_p + 2\Delta L\Big)\right]\lambda, \tag{4.13}$$

Note the presence of a factor of 2 multiplying the extension length, attributed to the radiating slots located on both sides of the resonator patch's extremities.

It is crucial to acknowledge that all parameters are varying in this analysis, except for the resonance frequency in free-space, which remains fixed at $(f_r)_{30} = 5.8$ GHz, consequently determining the wavelength in free-space. It is noteworthy that maintaining control over physical parameters proves challenging, as fixing them at constant values results in the resonance effect of TM_{30} shifting across the frequency domain, while the effective height varies electrically due to wave propagation through the substrate. Thus, the modification of permittivity values becomes necessary to assess radiation performance accurately. Therefore, our study's validity hinges upon the consideration of normalized values for both electrical and physical dimensions. For instance, an MPA operating in the fundamental mode possesses an electrical length equivalent to $\lambda/2$. However, during third mode operation, its effective length increases to $3\lambda/2$, as elucidated by Equation (4.14) considering the TM_{30}-mode:

$$L_{\text{eff}} \approx \frac{3}{2}\lambda. \tag{4.14}$$

Electrically speaking, the MPA exhibits a notable increase in its electrical dimensions, expanding from $\lambda/2$ to $3\lambda/2$. This augmentation is accompanied by a significant enhancement in directivity, particularly at resonance frequency (which is fixed using project technique).

4.6.2 Compact Sizing and Relationship Between Physical and Electrical Dimensions

The concept of ‘Compact Sizing’ intricately intertwines the relationship between electrical and physical dimensions. In the broader context of commercial and industrial demands, achieving an effective increase in volume while simultaneously reducing the physical packing volume embodies the essence of compactness sizing. This approach enables us to condense physical dimensions, thereby optimizing space utilization, while concurrently maintaining or even enhancing electrical dimensions. As emphasized at the outset of this chapter, the paramount objective is to develop devices that are adaptable to surfaces, occupy smaller areas, and facilitate reduced packing within integrated circuits.

Moreover, the effective volumetric packing size pertaining to the overall antenna configuration is computed through Eq. (4.15) normalized in terms of cubic wavelength λ^3:

$$\text{Overall}\,[\lambda^3] = L_{\text{eff}} \times W_{\text{eff}} \times h_{\text{eff}} = \left[L_{\text{eff}}^2 \left(\frac{h}{\lambda_0} \right) \right] \lambda^3, \tag{4.15}$$

The effective aperture of an antenna is defined as the ratio of the power delivered by the antenna to a conjugate matched load, to the incident co-polarized power density [80]. In essence, it quantifies the antenna's ability to capture and radiate electromagnetic energy. Notably, the effective aperture exceeds that of an isotropic antenna, representing its enhanced performance. Mathematically, the aperture efficiency can be computed as follows [8, Ch. 2]:

$$\varepsilon_{ap} = \frac{G_0 \lambda^2}{4\pi A_{phy}}, \tag{4.16}$$

where $A_{phy} = L_p^2$ is physical area for square of patch resonator, and λ guided wavelength is calculated by:

$$\lambda = \frac{c_0}{\sqrt{\varepsilon_{\text{reff}}}(f_r)_{mn}}. \tag{4.17}$$

The behavior discussed herein was analyzed, as depicted in Fig. 31, concerning compactness sizing across electrical, physical length, overall dimensions, and aperture efficiency (labelled by Aper. Eff.). In our analysis, we observe a notable trend in the effective length normalized by wavelength, denoted by L_{eff}, represented by the green dashed line with circular markers. This parameter exhibits a gradual increase from 1.45λ (at $\varepsilon_r = 1$), reaching 1.50λ (at

Figure 31. Analysis of compact sizing encompasses both electric dimensions (such as effective length and overall) and physical dimensions (resonator patch length).

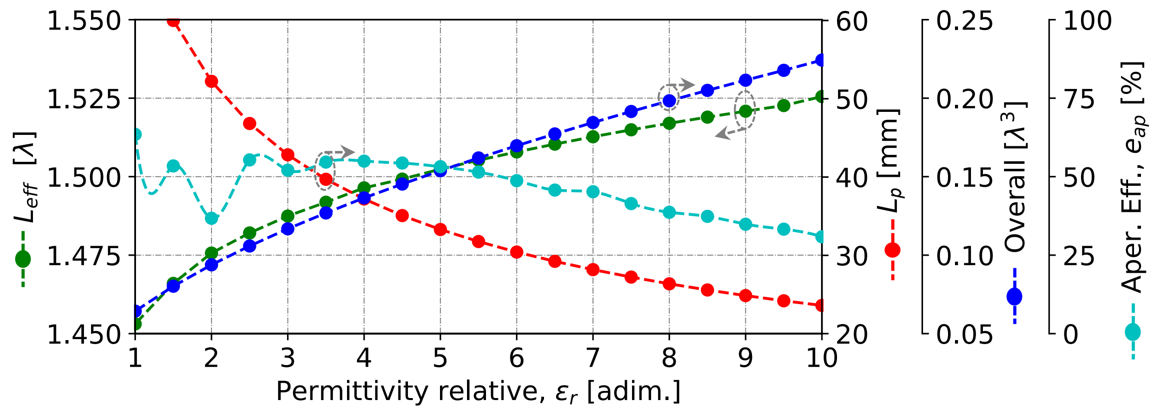

Source: author's own work (2024).

$\varepsilon_r = 5$), and culminating at 1.525λ (for $\varepsilon_r = 10$). Conversely, the physical length – red dashed line with circular markers, as previously discussed – demonstrates a contrasting pattern. Initially set at 60 mm (for $\varepsilon_r = 1.5$), it rapidly decreases to half its value, measuring 30 mm (at $\varepsilon_r = 6$), and then reduces to approximately 26 mm (for $\varepsilon_r = 10$).

Thus, the overall parameters governing the electrical "volume" of the antenna follow a behavior akin to the effective length, in blue dashed line with circular markers. Beginning with smaller values, approximately $0.05\lambda^3$ (for $\varepsilon_r = 1$), they gradually increase to $0.15\lambda^3$ (for $\varepsilon_r = 5$), eventually exceeding $0.2\lambda^3$ (for $\varepsilon_r = 10$). In the latter case, attention is drawn to the aperture efficiency curve, depicted by the cyan-blue dashed line with circular markers, representing perceptual values. The aperture efficiency demonstrates a remarkable stability from $\varepsilon_r = 1$ to 6, hovering around an upper threshold of 50%. Subsequently, there is a slight decline, reaching a maximum value of $\sim 25\%$ for dielectric constants surpassing 10, delineating the slight fall down of the electrical aperture and amplitude of total directivity.

4.7 Design and Project of a MPA with Reduced Sidelobes Levels

The proposed antenna structure is a conventional rectangular microstrip patch antenna consisting of a grounded substrate with a metallic material thickness of $t = 18\mu m$ and a square resonator patch positioned on the upper part of the MPA in the xy-plane. The physical dimensions of the patch, namely length ($L_p = W_p$) and width, remain constant. The length and width's substrate were considered $W_d = L_d \approx 3.11 L_p$ and the substrate's height ($h = 0.0322\lambda_0$, 1.270 mm) in the z-direction, with resonance frequency $(f_r)_{30} = 7.60$GHz utilizing dielectric material Rogers RT/Duroid 6006 (with permittivity relative $\epsilon_r = 6.15 \pm 0.15$ and loss tangent $\tan\delta = 0.0027$). The feeding configuration utilizes a coaxial probe with an input impedance of 50Ω. The software employed for analysis was Ansys Electronics Desktop with electromagnetic module HFSS 2023, utilizing the Finite Element Method [21] to calculate the electromagnetic fields.

We calculated the length of the patch $L_p = 23.7$ mm (using the Eq. (2.24)) for a resonator with a fundamental mode resonance frequency of $(f_r)_{10} = 2.533$ GHz, which results in a TM_{30}-mode at 7.6 GHz. Using the FEM method, we initially did not achieve a matching impedance, we conducted a parameterization of the feeding point $d_{\text{feed}} = 0.31 L_p$. The radiation pattern shown in Fig. 32 for frequency in 7.3GHz.

In Fig. 32(a), the radiation pattern is shown with the normalized realized gain for both planes. In the E-plane, the sidelobe levels reach approximately 15 dB. Another important characteristic is the widening of the main lobe in the E-plane. In the H-plane, depicted in red, we observe a main lobe in the broadside direction, which is the expected outcome.

Figure 32. Simulated (a) radiation pattern for TM_{30} in 7.3GHz and (b) realized gain in band.

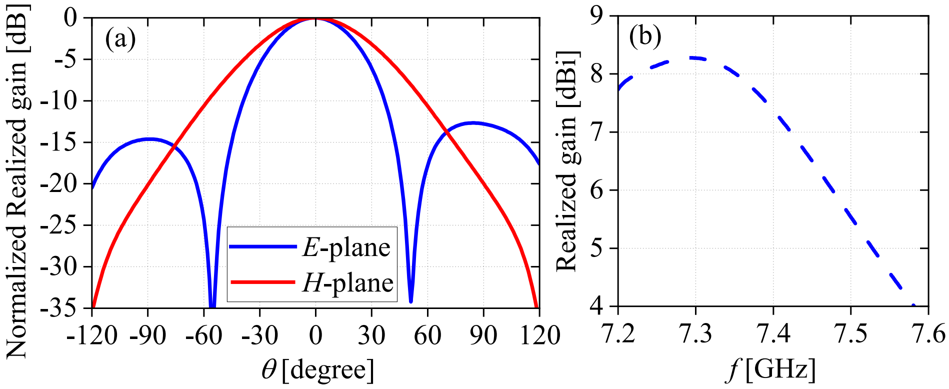

Source: author's own work (2024).

In Fig. 32(b), the realized gain is shown across the frequency band. Notably, the maximum peak at 7.3 GHz reaches a value of 8.3 dBi. This result highlights the need to combine this technique with others, as the conventional MPA model does not inherently offer higher gain and directivity, as demonstrated in our findings.

4.8 Directivity and Sidelobe Levels in Permittivity Variation

Finally, we observed that the behavior of SLL decreased from 13 dB to -33 dB on average at Fig. 33(a) linearly in decline (with trend fall off). The directivity showed variations from 12.2 to 9 dB and continued to stabilize within the analyzed permittivity range, as depicted in Fig. 33(a) and Fig. 33(b) enlarged. The patch length physical L_p (normalized in wavelength) decreased from 4λ to 0.5λ as ε_r fell, subsequently impacting the effective area from $2\lambda^2$ to $0.6\lambda^2$, following the interpolated directivity curve. We emphasize that in Fig. 33(b), the maximum peak directivity remains consistent at 11 dBi across permittivity values ranging from 2.5 to 6.0. However, beyond this range, the peak directivity begins to decline, reaching 10.5 dBi at $\varepsilon_r = 7.5$, and dropping further to below 10.0 dBi at $\varepsilon_r = 9$ and $\varepsilon_r = 10$. In terms of percentage, there is a global decrease of 49.88% in the absolute peak directivity. Another notable aspect (as depicted in Fig. 33(a) is that the sidelobe levels remain consistently below 5 dB across permittivity values ranging from 1 to 3. At $\varepsilon_r = 5$, the level approaches 0 dB. However, beyond this range, there is a slight linear decline, with the sidelobe level reaching -10 dB at $\varepsilon_r = 8$ and dropping more pronouncedly below -15 dB at $\varepsilon_r = 9$ and $\varepsilon_r = 10$.

Figure 33. Simulated behavior about antennas performance when the variation of relative permittivity ε_r for some figure-of-merit parameters. In (a) Sidelobe levels SLL and directivity D_0 decibel scale (the point represent each simulation realized and the continuous line is cubic interpolation have done) and (b) directivity in enlarged scale.

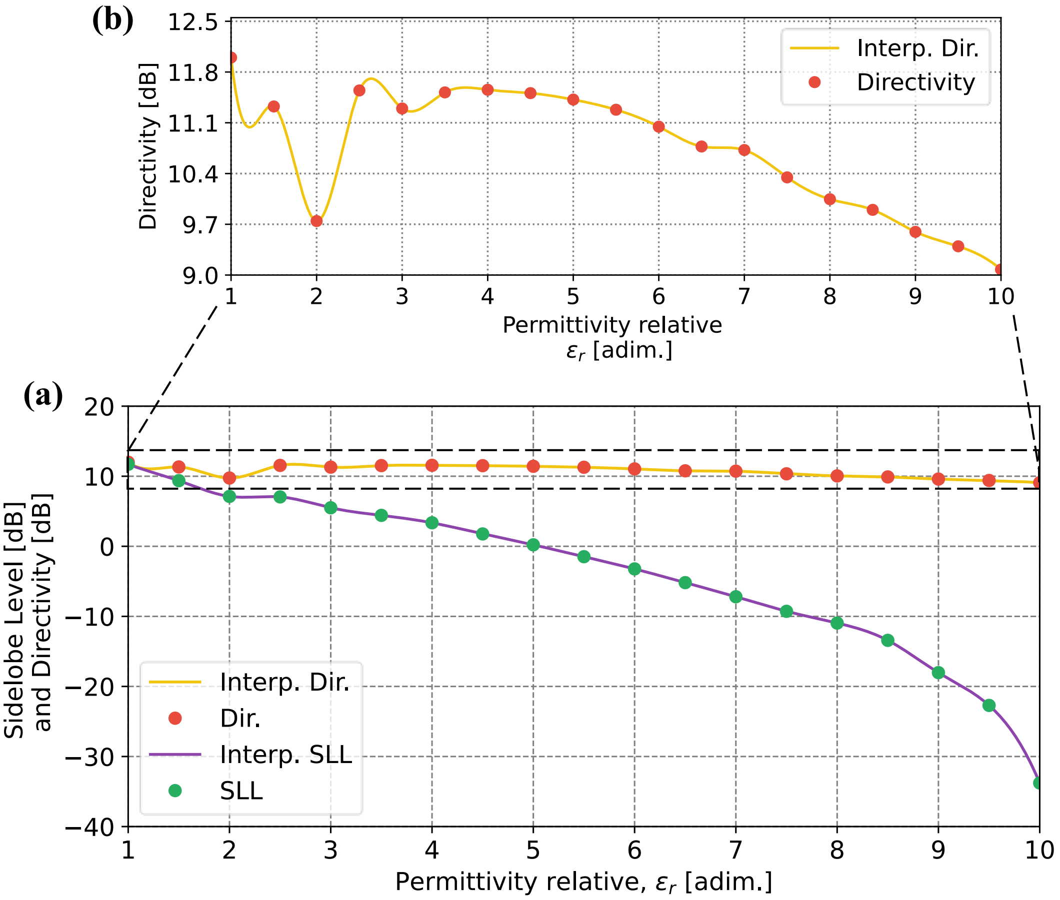

Source: author's own work (2024).

5 Comparison Between Methods and Models

5.1 Figure of Merit Gain-Area

To illustrate the primary comparative effects between the two methods, we present the radiation patterns at nearby frequencies, focusing on the models with reduced sidelobe levels, as shown in Fig. 34(a). The sidelobe levels for the permittivity analysis and slots and stubs techniques were approximately reduced, both strategies reach 12.7dB and 13.3dB of SLLs, respectively.

Figure 34. Comparison between (a) radiation patterns for both methods and (b) gain by effective area across the normalized frequency band.

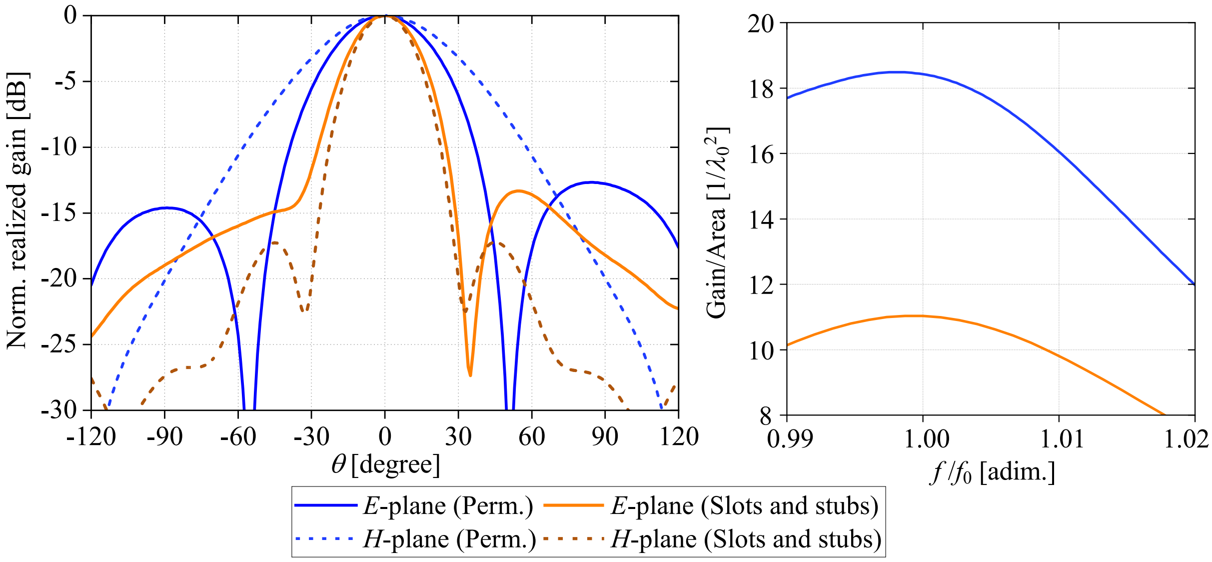

Source: author's own work (2024).

However, the main lobe from the slots and stubs technique was more directive due to a narrower beamwidth, being less aperture beam, which is a significant advantage for precise radar applications. In contrast, the main lobe from the permittivity analysis method was broader in the E-plane. Additionally, in the H-plane, the slots and stubs method produced a more directive beam compared to the more enlarged main lobe from the permittivity analysis.

In Fig. 34(b), we present the relationship between realized gain and effective area, measured in $\frac{1}{\lambda_0^2}$, as proposed. This metric demonstrates the effectiveness of the two models. Our discussion indicates that the permittivity analysis method achieves higher gain per area, which can be attributed to the drastic reduction in physical area to approximately $L_p \times W_p \approx 0.598\lambda_0 \times 0.598\lambda_0$, while maintaining a consistent gain of approximately 8.3 dBi.

In contrast, the effective area ($2.830\lambda_0 \times 2.830\lambda_0$) and gain of 15dBi both increase together in the slots and stubs method, resulting in a higher discrepancy of approximately 7 units of $\frac{1}{\lambda_0^2}$ in absolute comparison, at the normalized resonance frequency of the operating modes. Table 4 summarizes all the values of the main figures of merit from our analysis.

Table 4. Comparison between main figure of merit related two techniques.

Technique	TM_{m0}	G_0/A_{eff} $[1/\lambda_0^2]$	SLL^* [dB]	$(f_r)_{m0}$[GHz]
Permittivity	TM_{30}	18.40	12.7	7.30
Slots and stubs	TM_{50}-like	11.04	13.3	7.55

**Obtained from the realized gain for both models in the E-plane.*
Source: author's own work (2024).

5.2 Availability Between Resonance Frequencies

In Table 5, we provide an evaluation comparing the theoretical cavity model, the cavity model corrected by [36], the finite element method evaluated by a computational tool, and the relative error between the cavity model and the FEM method. The numerical values presented in Table 5 show discrepancies among themselves. The results indicate a correction with approximately 6.27% difference between the theoretical evaluation and computational simulation. These associated results, obtained through permittivity analysis which they are related to project and design of the MPA constructed considering the electromagnetic characteristics present in Sec. 4.7 and the substrate material more dense.

Table 5. Comparison between resonance frequencies $(f_r)_{m0}$ from theoretical model and computational FEM method in TM_{30} (using $\epsilon_r = 6.15$).

Cavity (Eq. (2.16))	Corrected by [36] (Eq. (2.23))	FEM	Relative error* $\Delta(f_r)_{m0}/(f_r)_{m0}$
7.65GHz	7.31GHz	7.22GHz	6.27%

**Operation realized between cavity model and computational method (FEM)*
Source: author's own work (2024).

In Table 6, we present the effect of resonance frequency for the TM_{50} mode using a lower permittivity. We observe a smaller discrepancy in the relative error compared to the previous analysis, with an approximate correction of 3.69%. It is important to highlight that these values simulate the actual MPA project, and permittivity is the only factor influencing these relative errors. Other factors, such as the loss tangent associated with lossy substrate material, the geometry of resonator patches, the substrate height, the mesh grid used for calculations, and numerous other factors, also play a role. Additionally, the order of resonance frequencies in different modes may contribute to the variations in errors observed in the conventional models presented in all tables.

Table 6. Comparison between resonance frequencies $(f_r)_{m0}$ from theoretical model and computational FEM method in TM_{50} (using $\epsilon_r = 2.20$).

Cavity (Eq. (2.16))	Corrected by [36] (Eq. (2.23))	FEM	Relative error* $\Delta(f_r)_{m0}/(f_r)_{m0}$
8.42GHz	8.20GHz	8.11GHz	3.69%

**Operation realized between cavity model and computational method (FEM)*

Source: author's own work (2024).

6 Conclusion

6.1 Advantages and Disadvantages

After presenting the two techniques for reducing and mitigating SLL, we can discuss their advantages and disadvantages, and bridge their effectiveness:

- In both methods discussed, a primary issue and challenge is the excitation of neighboring undesirable TM$_{mn}$-modes by numerous factors like the feed point, which disrupts the radiation pattern. This issue is inherent to the electromagnetic nature and is unavoidable even with modifications to the feed point distance.
- Permittivity analysis presented the Gain/Area more expressive, when we compare with slot and stubs method. The effective area in permittivity analysis becomes more smaller than slots and stubs that we work to increase the effective area and reduce the order mode without comprising the gain metric.
- A disadvantage of the permittivity analysis in relation to slots and stubs method is the fact of cutoff frequencies of surface mode become more lower with increasing dielectric constant. It excites TE$_{mn}$-modes undesirable perturbing resonance frequencies of TM$_{mn}$ desirable (in operation).
- A disadvantage of the permittivity analysis in relation to slots and stubs method is the fact of matching input impedance. The material larger dense permissively results in decrease of bandwidth, what it is problematic issue.
- An advantage common to both methods is their ease of implementation and employment in physical prototypes. They do not involve problematic fabrication processes such as short-pins, complex multi-layer structures, or other factors.
- One advantage of the slot-method compared to permittivity analysis is the potential for higher gain/directivity by implementing a slot-set in the resonator patch structure. Conversely, permittivity analysis tends to decrease gain/directivity to conventional values (from 13 dB to 9 dB) due to the increased dielectric constant.
- Another advantage of the slot-method over permittivity analysis is that most models achieve a quick impedance match, facilitated by slight adjustments to the feed point. In contrast, permittivity analysis complicates impedance matching because increasing permittivity exacerbates input impedance modifications and substrate reflections.

- An advantage of permittivity analysis is the reduction in physical area achieved by increasing the dielectric constant, which reduces SLL and makes the antenna more miniaturizable for small system-on-chip (SoC) applications. This reduction occurs while maintaining resonance frequency, with the effective length remaining practically constant at approximately 1.5λ, and an overall increase in size.
- Comparing the two techniques, aperture efficiency remains nearly constant at approximately 25% across all permittivity ranges in permittivity analysis. In the slot-method, however, aperture efficiency increases due to gain enhancement during the modification processes.

6.2 Future Perspectives

In future perspectives, we propose to continue this work with several key investigations:

- Exploring sophisticated feeding methods to selectively excite desired modes could be a valuable investigation, as it may filter out neighboring unwanted modes.
- Combining the slot-method with permittivity analysis could potentially achieve higher SLL reduction and optimize gain.
- Expanding the slot-method from TM_{50}-mode to even higher orders such as TM_{70} and TM_{90} modes presents an opportunity for further exploration.
- Study of array configuration with optimized slot antenna (TM_{50}-mode).

Bibliography

[1] A. N. Barreto, B. Faria, E. Almeida, I. Rodriguez, M. Lauridsen, R. Amorim, and R. Vieira, "5G – Wireless Communications for 2020," *Journal of Communication and Information Systems*, vol. 31, no. 1, Jun. 2016. [Online]. Available: https://jcis.sbrt.org.br/jcis/article/view/384

[2] 5G spectrum bands explained – low, mid and high band. Nokia Blog. [Online]. Available: https://www.nokia.com/thought-leadership/articles/spectrum-bands-5g-world/

[3] R. Sil and R. Chatterjee, *Evolution of Next-Generation Communication Technology.* Singapore: Springer Nature Singapore, 2023, pp. 1–17. [Online]. Available: https://doi.org/10.1007/978-981-99-3668-7_1

[4] H. Remmert, "When is 6G coming, and what does it mean for 5G and 4G LTE?" Aug. 2023, Digi International Blog. [Online]. Available: https://www.digi.com/blog/post/when-is-6g-coming-what-does-it-mean-for-5g-4g

[5] A. Morris, "O2 germany CEO gears up for 600MHz battle," Jan. 2023, lightReading Blog. [Online]. Available: https://www.lightreading.com/5g/o2-germany-ceo-gears-up-for-600mhz-battle#close-modal

[6] A. Ayeni, S. O. Onidare, O. A. Sowande, and Q. I. Adebowale, "Spectral limitations and the emerging trends in wireless communication," 2020.

[7] N. J. Gomes, P. P. Monteiro, and A. Gameiro, *Trends in Wireless Communications*, 2012, pp. 17–46.

[8] C. Balanis, *Antenna Theory: Analysis and Design.* Wiley, 2016. [Online]. Available: https://books.google.com.br/books?id=iFEBCgAAQBAJ

[9] B. G. P. Shariff, T. Ali, P. R. Mane, and P. Kumar, "Array antennas for mmwave applications: A comprehensive review," *IEEE Access*, vol. 10, pp. 126 728–126 766, 2022.

[10] A. Chen, "What is a horn antenna?" mar. 2024. [Online]. Available: https://www.sannytelecom.com/what-is-a-horn-antenna/

[11] E. Nugoolcharoenlap and G. Mansour, "Microstrip array antennas for Point-to-Point WLAN links," vol. 6, p. 2020, 07 2020.

[12] A. Arora, A. Rana, A. Yadav, and R. Yadava, "Design of microstrip patch antenna at 2.4 GHz for Wi-Fi and bluetooth applications," *Journal of Physics:*

Conference Series, vol. 1921, no. 1, p. 012023, may 2021. [Online]. Available: https://dx.doi.org/10.1088/1742-6596/1921/1/012023

[13] N. K. Nikolova, M. Ravan, and R. K. Amineh, “Chapter six - substrate-integrated antennas on silicon,” in *Silicon-Based Millimeter-wave Technology*, ser. Advances in Imaging and Electron Physics, M. J. Deen, Ed. Elsevier, 2012, vol. 174, pp. 391–458. [Online]. Available: https://www.sciencedirect.com/science/article/pii/B9780123942982000065

[14] S.-P. Gao, B. Wang, H. Zhao, W.-J. Zhao, and C. E. Png, “Installed radiation pattern of patch antennas: Prediction based on a novel equivalent model,” *IEEE Antennas and Propagation Magazine*, vol. 57, no. 3, pp. 81–94, 2015. [Online]. Available: https://doi.org/10.1109/MAP.2015.2437275

[15] N. Kaur and S. Malhotra, “A review on significance of design parameters of microstrip patch antennas,” in *2016 5th International Conference on Wireless Networks and Embedded Systems (WECON)*, 2016, pp. 1–6.

[16] A. G. Koutinos, G. A. Ioannopoulos, M. T. Chryssomallis, and G. A. Kyriacou, “Bandwidth enhancement of rectangular patch antennas using multiple feeding points: A review,” in *2018 7th International Conference on Modern Circuits and Systems Technologies (MOCAST)*, 2018, pp. 1–4.

[17] C. R. Peñafiel-Ojeda, C. E. Andrade, R. Baez-Egas, and V. Garcia-Santos, “An ultrawideband printed monopole antenna analyzed with the theory of characteristic modes,” *IEEE Latin America Transactions*, vol. 20, no. 6, pp. 948–954, 2022.

[18] U. Rafique, S. Pisa, R. Cicchetti, O. Testa, and M. Cavagnaro, “Ultra-wideband antennas for biomedical imaging applications: A survey,” *Sensors*, vol. 22, no. 9, 2022. [Online]. Available: https://www.mdpi.com/1424-8220/22/9/3230

[19] M. Garg and N. Singh, “Rectangular microstrip patch antenna,” *International Journal of Computer Science And Technology*, vol. 6, no. 4, dec. 2015. [Online]. Available: https://www.ijcst.com/vol64/2/59-nisha-singh.pdf

[20] T. Hemalatha, B. Roy, B. Chakrabarti, A. Bhattacharya, and T. Hirano, “Analyzing the effect of substrates on a compact pentagonal patch antenna-a short review,” in *2023 3rd International Conference on Range Technology (ICORT)*, 2023, pp. 1–6.

[21] Ansys Inc., Ansys Electronics Desktop HFSS 2023, Canonsburg, PA 15317 USA, 2023.

[22] C. U. Ndujiuba and A. O. Oloyede, “Selecting best feeding technique of a rectangular patch antenna for an application,” *International Journal of Electromagnetics and Applications*, vol. 5, no. 3, pp. 99–107, 2015.

[23] I. B. Ramesh Garg, Prakash Bhartia and A. Ittipiboon, *Microstrip Antenna Design Handbook.* London: Artech House, 2001. [Online]. Available: https://books.google.com.br/books/about/Microstrip_Antenna_Design_Handbook.html?id=_er1LO5pEnUC&redir_esc=y

[24] A. Bansal and R. Gupta, "A review on microstrip patch antenna and feeding techniques," *Int. J. Inf. Tecnol.*, vol. 12, pp. 149–154, 2018. [Online]. Available: https://doi.org/10.1007/s41870-018-0121-4

[25] D. R. Jackson, *Microstrip Antennas*, 5th ed. McGraw Hill, 2007, ch. 7, john L. Volakis, Editor. In: Antenna Engineering Handbook.

[26] G. Unal and M. Aksun, "Bridging the gap between RF and optical patch antenna analysis via the cavity model," *Sci. Rep.*, vol. 5, no. 15941, 2015. [Online]. Available: https://doi.org/10.1038/srep15941

[27] K. F. Lee and K. M. Luk, *Microstrip Patch Antennas.* Imperial College Press, 2010. [Online]. Available: https://www.worldscientific.com/doi/abs/10.1142/p669

[28] D. R. Jackson, "Overview of microstrip antennas," dept. of ECE, University of Houston. [Online]. Available: https://www.mikrocontroller.net/attachment/208694/microstrip_antennas_overview.pdf

[29] ——, "Introduction to microstrip antennas," dept. of ECE, University of Houston. [Online]. Available: https://courses.egr.uh.edu/ECE/ECE6345/Short%20Course/Introduction%20to%20Microstrip%20Antennas.pdf

[30] C. A. Balanis, *Modern antenna handbook.* John Wiley & Sons, 2011.

[31] S. Chuang, L. Tsang, J. Kong, and W. Chew, "The equivalence of the electric and magnetic surface current approaches in microstrip antenna studies," *IEEE Transactions on Antennas and Propagation*, vol. 28, no. 4, pp. 569–571, 1980.

[32] D. M. Pozar, *Microwave Engineering*, 4th ed. Hoboken, NJ: John Wiley & Sons, Inc., 2012.

[33] S. J. Orfanidis, *Electromagnetic Waves and Antennas*, 2016. [Online]. Available: https://www.ece.rutgers.edu/~orfanidi/ewa/

[34] G. Kumar and K. P. Ray, *Broadband microstrip antennas.* Artech House, 2003.

[35] P. Hammer, D. Van Bouchaute, D. Verschraeven, and A. Van de Capelle, "A model for calculating the radiation field of microstrip antennas," *IEEE Transactions on Antennas and Propagation*, vol. 27, no. 2, pp. 267–270, 1979.

[36] R. Dearnley and A. Barel, “A comparison of models to determine the resonant frequencies of a rectangular microstrip antenna,” *IEEE Transactions on Antennas and Propagation*, vol. 37, no. 1, pp. 114–118, 1989.

[37] Z. Ahmed, “TM_{m0} mode rectangular patch antennas with improved radiation characteristics,” Ph.D. dissertation, Department of Electrical Engineering, Capital University of Science and Technology, Islamabad, 2021.

[38] W. Richards, Y. Lo, and D. Harrison, “An improved theory for microstrip antennas and applications,” *IEEE Transactions on Antennas and Propagation*, vol. 29, no. 1, pp. 38–46, 1981.

[39] I. B. Ramesh Garg, Prakash Bhartia and A. Ittipiboon, *Microstrip Antenna Design Handbook*. London: Artech House, 2001, ch. 4. Rectangular Microstrip Antennas, pp. 253–316. [Online]. Available: https://books.google.com.br/books/about/Microstrip_Antenna_Design_Handbook.html?id=_er1LO5pEnUC&redir_esc=y

[40] N. M. Martin, “The computer-aided design of rectangular microstrip antennas,” dec. 1984. [Online]. Available: https://digital.library.adelaide.edu.au/dspace/bitstream/2440/19674/2/02whole.pdf

[41] S. Liu and K. Yu, “Successive multivariate variational mode decomposition,” *Multidimensional Systems and Signal Processing*, vol. 33, 09 2022.

[42] M. S. Rabbani and H. Ghafouri-Shiraz, “Improvement of microstrip patch antenna gain and bandwidth at 60 GHz and X bands for wireless applications,” *IET Microwaves, Antennas & Propagation*, vol. 10, no. 11, pp. 1167–1173, 2016. [Online]. Available: https://ietresearch.onlinelibrary.wiley.com/doi/abs/10.1049/iet-map.2015.0672

[43] W.-J. Lu, J. Yu, and L. Zhu, “On the multi-resonant antennas: Theory, history, and new development,” *International Journal of RF and Microwave Computer-Aided Engineering*, vol. 29, no. 9, p. e21808, 2019. [Online]. Available: https://onlinelibrary.wiley.com/doi/abs/10.1002/mmce.21808

[44] Q. U. Khan and M. B. Ihsan, “Higher order mode excitation for high gain microstrip patch antenna,” *AEU – International Journal of Electronics and Communications*, vol. 68, no. 11, pp. 1073–1077, 2014. [Online]. Available: https://www.sciencedirect.com/science/article/pii/S1434841114001575

[45] A. Singh, S. Vijay, and R. N. Baral, “Low cross-polarization improved-gain rectangular patch antenna,” *Electronics*, vol. 8, no. 10, 2019. [Online]. Available: https://www.mdpi.com/2079-9292/8/10/1189

[46] X. Zhang, L. Zhu, and Q.-S. Wu, "Sidelobe-Reduced and Gain-Enhanced Square Patch Antennas With Adjustable Beamwidth Under TM_{03} Mode Operation," *IEEE Transactions on Antennas and Propagation*, vol. 66, no. 4, pp. 1704–1713, apr 2018. [Online]. Available: https://ieeexplore.ieee.org/document/8291150/

[47] R. Santos, H. S. Bernardo, M. R. Almeida, and R. A. Penchel, "Design antena de microfita com alto ganho deslocando a frequência de ressonância com pinos em curto-circuito para aplicações no 5G," in *Anais do XLI Simpósio Brasileiro de Telecomunicações e Processamento de Sinais (SBrT2023).* São José dos Campos, São Paulo: Biblioteca do SBrT, out 2023, pp. 1–5. [Online]. Available: https://doi.org/10.14209/sbrt.2023.1570916723

[48] X. Zhang, K.-D. Hong, L. Zhu, X.-K. Bi, and T. Yuan, "Wideband differentially fed patch antennas under dual high-order modes for stable high gain," *IEEE Transactions on Antennas and Propagation*, vol. 69, no. 1, pp. 508–513, 2021.

[49] "IEEE standard letter designations for radar-frequency bands," *IEEE Std 521-2019 (Revision of IEEE Std 521-2002)*, pp. 1–15, 2020. [Online]. Available: https://doi.org/10.1109/IEEESTD.2020.8999849

[50] S. Spolitis, I. Kurbatska, and V. Bobrovs, "Comparison of C-band and L-band WDM-PON systems performance with PAM-4 modulation format," in *2017 International Workshop on Fiber Optics in Access Network (FOAN)*, 2017, pp. 1–6.

[51] "Satellite frequency bands," 2024, European Space Agency. [Online]. Available: https://www.esa.int/Applications/Connectivity_and_Secure_Communications/Satellite_frequency_bands

[52] "Satellite frequency allocation and the band spectrum," 2023, Cadence PCB Solutions. [Online]. Available: https://resources.pcb.cadence.com/blog/2023-satellite-frequency-allocation-and-the-band-spectrum

[53] J. Hao, N. Yan, Y. Luo, H. Fu, and K. Ma, "A Low-Cost Dual-Band Multimode High-Gain Stacked-Patch Antenna Based on SISL for 5G Applications," *IEEE Antennas and Wireless Propagation Letters*, vol. 21, no. 1, pp. 4–8, Jan. 2022. [Online]. Available: https://ieeexplore.ieee.org/document/9537592/

[54] Z. Ahmed, A. Muhammad, and M. B. Ihsan, "Improving the Sidelobe Level, Return Loss and Bandwidth of Notch-Loaded TM_{30} Mode Patch via Fractal-Slot," *IEEE Access*, vol. 10, pp. 19 917–19 924, 2022. [Online]. Available: https://ieeexplore.ieee.org/document/9716124/

[55] A. Bhattacharyya, J. Pal, K. Patra, and B. Gupta, "Bandwidth-Enhanced Miniaturized Patch Antenna Operating at Higher Order Dual-Mode Resonance Using

Modal Analysis," *IEEE Antennas and Wireless Propagation Letters*, vol. 20, no. 2, pp. 274–278, Feb. 2021. [Online]. Available: https://ieeexplore.ieee.org/document/9311696/

[56] Y. Luo, Z. N. Chen, and K. Ma, "A Single-Layer Dual-Polarized Differentially Fed Patch Antenna With Enhanced Gain and Bandwidth Operating at Dual Compressed High-Order Modes Using Characteristic Mode Analysis," *IEEE Transactions on Antennas and Propagation*, vol. 68, no. 5, pp. 4082–4087, may 2020. [Online]. Available: https://ieeexplore.ieee.org/document/8895839/

[57] R. A. Santos, H. S. Bernardo, D. H. Spadoti, G. S. da Rosa, and R. A. Penchel, "Gain enhancement and sidelobe level reduction of microstrip patch antenna under operation of TM_{50}-like mode," *IEEE Open Journal of Antennas and Propagation*, pp. 1–1, 2024.

[58] Y. He, Y. Li, W. Sun, and Z. Zhang, "Dual-Polarized, High-Gain, and Low-Profile Magnetic Current Array Antenna," *IEEE Transactions on Antennas and Propagation*, vol. 67, no. 2, pp. 1312–1317, Feb. 2019. [Online]. Available: https://ieeexplore.ieee.org/document/8548581/

[59] J. Anguera, A. Andújar, and J. Jayasinghe, "High-directivity microstrip patch antennas based on $TM_{\text{odd-0}}$ modes," *IEEE Antennas and Wireless Propagation Letters*, vol. 19, no. 1, pp. 39–43, Jan. 2020.

[60] Y. He, Y. Li, W. Sun, Z. Zhang, and P.-Y. Chen, "Dual Linearly Polarized Microstrip Antenna Using a Slot-Loaded TM_{50} Mode," *IEEE Antennas and Wireless Propagation Letters*, vol. 17, no. 12, pp. 2344–2348, dec 2018. [Online]. Available: https://ieeexplore.ieee.org/document/8485346/

[61] J. Wen, D. Xie, and L. Zhu, "Bandwidth-Enhanced High-Gain Microstrip Patch Antenna Under TM_{30} and TM_{50} Dual-Mode Resonances," *IEEE Antennas and Wireless Propagation Letters*, vol. 18, no. 10, pp. 1976–1980, Oct. 2019. [Online]. Available: https://ieeexplore.ieee.org/document/8801890/

[62] A. M. Zaidi, M. T. Beg, B. K. Kanaujia, and K. Rambabu, "Hexa-band branch line coupler and wilkinson power divider for LTE 0.7 GHz, LTE 1.7 GHz, LTE 2.6 GHz, 3.9 GHz, public safety band 4.9 GHz, and WLAN 5.8 GHz frequencies," *IEEE Transactions on Circuits and Systems II: Express Briefs*, vol. 67, no. 2, pp. 275–279, 2020.

[63] P. Gupta, M. Bharti, and A. Kumar, "Circularly polarized two port flexible antenna for WLAN and Wi-Fi-6 applications," in *2022 4th International Conference on Advances in Computing, Communication Control and Networking (ICAC3N)*, 2022, pp. 1661–1665.

[64] X. Zhang, Y. Zhang, D. Liao, X. Zhou, C. Tang, and S. Ci, "Bidirectional cache for P2P traffic in WLAN," in *2012 13th International Conference on Parallel and Distributed Computing, Applications and Technologies*, 2012, pp. 638–641.

[65] Z. A. Hassoun, M. H. Wali, H. A. Hussein, N. H. Haroon, and A. Alkhayyat, "Study the effect of dielectric permittivity and changing substrates material on microstrip patch antenna," in *2022 International Congress on Human-Computer Interaction, Optimization and Robotic Applications (HORA)*, 2022, pp. 1–5.

[66] P. K. Desai and S. Bindu, "Impact of dielectric substrate on the performance of microstrip patch antenna at millimeter wave frequency," in *2023 International Conference on Intelligent and Innovative Technologies in Computing, Electrical and Electronics (IITCEE)*, 2023, pp. 629–632.

[67] E. Vythee and R. A. Jugurnauth, "Microstrip patch antenna design and analysis with varying substrates for 5G," in *2020 3rd International Conference on Emerging Trends in Electrical, Electronic and Communications Engineering (ELECOM)*, 2020, pp. 141–146.

[68] L. Zhang, Q. Zhang, and C. Hu, "The influence of dielectric constant on bandwidth of u-notch microstrip patch antenna," in *2010 IEEE International Conference on Ultra-Wideband*, vol. 1, 2010, pp. 1–4.

[69] I. Marcansola, "Design de antenas patch retangular operando em modos de alta ordem," 2022. [Online]. Available: http://hdl.handle.net/11449/238020

[70] W. H. Hayt, Jr. and J. A. Buck, *Engineering Electromagnetics*, 6th ed. McGraw-Hill Series in Electrical and Computer Engineering, 2001.

[71] C. A. Balanis, *Advanced Engineering Electromagnetics*, 2nd ed., ser. CourseSmart Series. John Wiley & Sons, 2012. [Online]. Available: https://books.google.com.br/books?id=_q35KChOfVwC

[72] K. Zhang and D. Li, *Electromagnetic Theory for Microwaves and Optoelectronics*, 2nd ed. Springer, 2007.

[73] R. K. Kupka, "k-space TE/TM beam propagation method: derivation, assessment, and accurate correction for reflected fields and multiple reflections," *J. Opt. Soc. Am. A*, vol. 12, no. 2, pp. 404–419, Feb 1995. [Online]. Available: https://opg.optica.org/josaa/abstract.cfm?URI=josaa-12-2-404

[74] "The electromagnetic spectrum," fev. 2013, National Aeronautics and Space Administration (NASA), Goddard Space Flight Center. [Online]. Available: https://imagine.gsfc.nasa.gov/science/toolbox/emspectrum2.html#:~:text=Radio%20waves%20have%20photons%20with,X%2Drays%20and%20gamma%20rays.

[75] “A te-mode rectangular microstrip patch antenna excited by coplanar l-strip feed,” *Progress In Electromagnetics Research C*, vol. 134, pp. 171–180, 2023.

[76] D. Cheng, “Optimization techniques for antenna arrays,” *Proceedings of the IEEE*, vol. 59, no. 12, pp. 1664–1674, 1971.

[77] S. M. Radha, G. Shin, W. Kim, S. I. H. Shah, and I.-J. Yoon, “Design and verification of an electrically small, extremely thin dual-band quasi-isotropic antenna,” *IEEE Antennas and Wireless Propagation Letters*, vol. 19, no. 12, pp. 2482–2486, 2020.

[78] X. Weng, Y. Miao, G. Wang, Y. Wang, Q. Zhan, X. Dong, J. Qu, X. Gao, and S. Zhuang, “Property unification of inherent amplitude, phase and polarization within a light beam,” 2022.

[79] D. J. Griffiths, *Introduction to Electrodynamics*, 3rd ed. Prentice Hall, 1999.

[80] S. W. Ellingson, “Effective aperture,” libreTexts Physics, Sec. 10 Antennas. [Online]. Available: https://phys.libretexts.org/Bookshelves/Electricity_and_Magnetism/Electromagnetics_II_(Ellingson)/10%3A_Antennas/10.13%3A_Effective_Aperture

List of all Publications and Works

Journal Article

Renan A. dos Santos, **H. S. Bernardo**, Danilo H. Spadoti, Guilherme S. da Rosa and Rafael A. Penchel, “Gain Enhancement and Sidelobe Level Reduction of Microstrip Patch Antenna Under Operation of TM$_{50}$-like Mode,” *IEEE Open Journal of Antennas and Propagation*, 31th may 2024 (early access), doi: 10.1109/OJAP.2024.3406950.

National Conference

H. S. Bernardo, R. A. dos Santos, E. Simionato, I. Aldaya, G. S. da Rosa and R. A. Penchel, “High-Gain and Wideband Microstrip Patch Antenna for 5G Sub-6 GHz Applications,” *21 Simpósio Brasileiro de Micro-Ondas e Optoeletrônica (SBMO2024)*, 2024, 15th–18th sep. 2024, Anais do Simpósio Brasileiro de Micro-Ondas e Optoeletrônica [Accepted].

Book Chapter

H. S. Bernardo, E. M. F. de Oliveira and R. A. Penchel, “Análise de geometrias distribuídas de dispositivos de microondas por equivalentes em circuitos elétricos,” in “Tendências e avanços científicos nas engenharias: aeronáutica, aeroespacial, eletrônica e de telecomunicações,” ed. 2nd, vol. 3, Campinas Grande: Editora Amplla, 2023, pp. 50 – 68, doi: 10.51859/amplla.tac393.1323-5.

National Conference

R. A. dos Santos, **H. S. Bernardo**, M. R. Almeida and R. A. Penchel, “Design Antena de Microfita com Alto Ganho Deslocando a Frequência de Ressonância com Pinos em Curto-Circuito para Aplicações no 5G,” *XLI Simpósio Brasileiro de Telecomunicações e Processamento de Sinais (SBrT2023)*, 2023, São José dos Campos, pp. 1–5, 8th out. 2023, Anais do Simpósio Brasileiro de Telecomunicações e Processamento de Sinais, doi: 10.14209/sbrt.2023.1570916723.

Workshop Seminar

H. S. Bernardo, G. S. da Rosa, R. A. Penchel, “High-Gain and Reduced Side-Lobe Levels for a Patch Antenna Operating in the TM$_{05}$-Mode for Millimeter-Wave Applications at 60GHz in Indoor Environments,” Workshop Program Post-Graduate in Electrical Engineering, [Presentation], 1st dec. 2023.